

**NUMERICAL SIMULATION AND MODELING OF COMPRESSOR STAGE  
INSTABILITY OF A ROTATING STALL NATURE**

**By**

**Marco Vagani**

A DISSERTATION

Submitted to  
Michigan State University  
in partial fulfillment of the requirements  
for the degree of

DOCTOR OF PHILOSOPHY

Mechanical Engineering

2012

## **ABSTRACT**

### **NUMERICAL SIMULATION AND MODELING OF COMPRESSOR STAGE INSTABILITY OF A ROTATING STALL NATURE**

By

Marco Vagani

Rotating stall is an unsteady flow phenomenon that appears in both axial and centrifugal compressors. It is detrimental to the performance of the compressor, significantly narrowing its operating range. Numerical simulation of this phenomenon has been a major area of investigation for axial compressors with some success. While stall occurs less often in centrifugal compressors than axial ones, it can be much harder to predict. Some preventive measures are known, but are mostly rules of thumb developed through experimental experience. Accurate modeling of rotating stall will allow for better understating of the onset conditions and possible preventive measures that may be adopted during the design stage, before testing.

This work focuses on the prediction of impeller rotating stall using Computational Fluid Dynamics. A compressor was chosen that has demonstrated rotating stall instabilities with different diffuser lengths and return vanes. Unsteady numerical simulations were performed to establish the reliability with which rotating stall can be captured, as compared to the experimental results. Fast Fourier Transform analysis was used to determine the mass-flow fluctuations in the domain that can be associated to the phenomenon. These observations were then used to determine the onset flow rate for impeller rotating stall. Finally, a redesign of the compressor is proposed and analyzed using the developed methodology.

## ACKNOWLEDGEMENTS

I would like to start by expressing my gratitude toward Dr. Abraham Engeda, who has supported me in my research and personal life in so many ways. I thank him for his encouragement, confidence in my abilities, and the many life lessons he provided. I wish him all the best in his professional and personal life.

I would also like to thank Dr. Norbert Müller, Dr. Criag Somerton, and Dr. Elias Strangas for agreeing to participate in my guidance committee and for their comments that helped me improve this work. I am especially grateful to Dr. Müller for his support over the years and for sparking my interest in the area of Turbomachinery.

This work would not be possible without the support and experience provided by Solar Turbines Incorporated. I would especially like to thank Avneet Singh for the experimental data provided for this work, and Mike Cave for the guidance and advice during my internships and research work.

On a personal note, I would like to thank my family and friends. My family provided the stepping stones for a great career, and my friends helped me persevere through the long hours even when there was no end in sight. Finally, the biggest thank you of all goes to my wife Elizabeth, who has sacrificed so much for my career. I thank her for her unrelenting support, for understanding and putting up with the distant internships, for being a great mother, and for motivating me every day.

# TABLE OF CONTENTS

<b>LIST OF TABLES .....</b>	<b>vi</b>
<b>LIST OF FIGURES .....</b>	<b>vii</b>
<b>NOMENCLATURE.....</b>	<b>xi</b>
<b>CHAPTER 1: INTRODUCTION.....</b>	<b>1</b>
1.1 MOTIVATION.....	1
1.2 ROTATING STALL CLASSIFICATION AND CHARACTERIZATION.....	5
1.3 ROTATING STALL PROPAGATION .....	8
1.4 CORRECTIVE SOLUTIONS .....	15
1.5 NUMERICAL STUDIES OF ROTATING STALL .....	18
1.6 OBJECTIVES .....	25
<b>CHAPTER 2: EXPERIMENTAL COMPRESSOR TESTING.....</b>	<b>27</b>
2.1 COMPRESSOR SELECTION.....	27
2.2 TEST SETUP.....	28
2.3 RESULTS .....	33
<b>CHAPTER 3: METHODOLOGY .....</b>	<b>38</b>
3.1 THE INVESTIGATION PLATFORM .....	38
3.2 STEADY-STATE VALIDATION.....	40
3.3 360° GRID GENERATION .....	42
3.4 TURBULENCE MODELS.....	46
3.5 PARALLEL PROCESSING .....	48
3.6 FIXED-FLOW TRANSIENT SIMULATIONS .....	51
3.7 SPEED-LINE TRANSIENT SIMULATIONS.....	55
<b>CHAPTER 4: FIXED-FLOW TRANSIENT SIMULATIONS.....</b>	<b>59</b>
4.1 ROTATING STALL AT $N = 20640$ RPM.....	59
4.2 ANALYSIS OF MASS FLOW FLUCTUATIONS.....	64
4.3 COMPRESSOR SURGE AT $N = 21860$ RPM.....	68
4.4 CONCLUSIONS.....	70
<b>CHAPTER 5: SPEED-LINE TRANSIENT SIMULATIONS.....</b>	<b>72</b>
5.1 20640 RPM SPEED LINE.....	72
5.2 19240 RPM SPEED LINE.....	82
5.3 COMPARISON TO EXPERIMENTS .....	86
5.4 CONCLUSIONS .....	87
<b>CHAPTER 6: COMPRESSOR RE-DESIGN .....</b>	<b>89</b>
6.1 OBJECTIVES .....	89
6.2 BLADE DESIGN .....	90
6.3 STEADY-STATE PERFORMANCE .....	95



6.4	BLADE LOADING.....	98
6.5	SPEED-LINE TRANSIENT RESULTS .....	102
6.6	CONCLUSIONS.....	111
<b>CHAPTER 7: CONCLUSIONS .....</b>		<b>113</b>
7.1	SUMMARY.....	113
7.2	CONTRIBUTIONS .....	114
7.3	RECOMMENDATIONS.....	115
<b>REFERENCES.....</b>		<b>119</b>

## LIST OF TABLES

Table 1.1.	Some documented cases of rotating instabilities in numerical simulations for various turbomachines .....	20
Table 1.2.	Documented cases of rotating stall in numerical simulations for centrifugal compressors .....	20
Table 2.1.	Test rig geometry for selected centrifugal compressor.....	27
Table 2.2.	Experimental rotating stall onset points with the original return channel .....	35
Table 2.3.	Experimental rotating stall onset points with the reduced return channel .....	35
Table 3.1.	Grid accuracy for single-passage meshes .....	44
Table 3.2.	Solution time reduction for parallel processing, run for 400 iterations with 4,065,828 nodes .....	50

## LIST OF FIGURES

Figure 1.1.	Performance map showing the actual surge line and rotating stall onset line .....	2
Figure 1.2.	Blade vibration measurements plotted on a compressor performance map, as recorded experimentally by Haupt, Jin and Rautenberg [14] .....	4
Figure 1.3.	Rotating stall pattern corresponding to $m = -3$ [9].....	5
Figure 1.4.	Schematic of stall propagation in the direction opposite to impeller rotation [9] .....	9
Figure 1.5.	Sequence of passage stall in a shrouded compressor impeller, as recorded experimentally by Lennemann and Howard [27] .....	10
Figure 1.6.	Sequence of passage stall in an unshrouded compressor impeller, as recorded experimentally by Lennemann and Howard [27] .....	11
Figure 1.7.	Sequence of pressure contours during rotating stall in a centrifugal compressor impeller with splitter vanes, recorded experimentally by J. Chen et al. [29] .....	13
Figure 1.8.	Rossby wave, high (H) and low (L) pressure vortices producing the forward and reverse flows in rotating stall (adapted from Y. N. Chen [33]) .....	14
Figure 1.9.	Axial compressor rotating stall and the effect of inlet air jets for control (adapted from J.P. Chen et al. [48]).....	21
Figure 1.10.	Numerical simulations of stability limit for a vaneless diffuser [56] .....	22
Figure 1.11.	Diffuser rotating stall control with air jets at the diffuser inlet (adapted from J.P. Chen et al. [48]) .....	23
Figure 1.12.	Velocity vectors displaying backflow near the leading edge of a low-speed centrifugal compressor [10].....	24
Figure 2.1.	Solar Turbines test facility schematic [60] .....	28
Figure 2.2.	Dynamic pressure measurement sites in the diffuser.....	30
Figure 2.3.	Graphical method for determining number of stall cells .....	32
Figure 2.4.	Comparison of flow path between original return channel and reduced flow return channel .....	34
Figure 2.5.	Test results for C2-HP compressor with C2 (original) and A2 (reduced) return channels .....	37

Figure 3.1.	Schematic of impeller model used for CFD validation, with boundaries and interfaces .....	41
Figure 3.2.	Isentropic head coefficient and efficiency comparison between experimental and steady-state numerical results at $N = 19240$ rpm .....	42
Figure 3.3.	Detail of full $360^\circ$ mesh used for simulations, near blade trailing edge.....	45
Figure 3.4.	Detail of full $360^\circ$ mesh used for simulations, near blade leading edge .....	45
Figure 3.5.	Mesh overlap nodes for partitioning, adapted from ANSYS CFX [66] .....	49
Figure 3.6.	Solution times and overlap percentage variation with number of parallel processors.....	51
Figure 3.7.	Full $360^\circ$ computational model used for transient CFD simulations, with axial inlet, impeller, diffuser and interfaces .....	54
Figure 4.1.	Velocity vectors showing development of rotating stall cell, $N = 20640$ rpm and $\varphi_1 = 0.04308$ .....	60
Figure 4.2.	Meridional velocity near blade leading edge during rotating stall, $N = 20640$ rpm and $\varphi_1 = 0.04308$ , at simulation time $t = 434.1 \times 10^{-6}$ sec .....	62
Figure 4.3.	Pressure contours showing development of rotating stall low-pressure zone, $N = 20640$ rpm and $\varphi_1 = 0.04308$ .....	63
Figure 4.4.	Time-record of mass flow rates for transient simulation at $N = 20640$ rpm and $\varphi_1 = 0.04308$ .....	65
Figure 4.5.	Frequency spectrum of mass-flow signals at rotor interfaces, $N = 20640$ rpm and $\varphi_1 = 0.04308$ .....	66
Figure 4.6.	Frequency spectrum of the normalized mass-flow imbalance, comparing rotating stall at $N = 20640$ rpm and $\varphi_1 = 0.04308$ with normal operation at $N = 19240$ rpm and $\varphi_1 = 0.054$ .....	68
Figure 4.7.	Time-record of mass flow rates for transient simulation at $N = 21840$ rpm and $\varphi_1 = 0.04985$ .....	69
Figure 5.1.	Time-record of mass flow rates for full $360^\circ$ speed-line simulation at $N = 20640$ rpm.....	73
Figure 5.2.	Close-up view of the mass flow rates for $N = 20640$ rpm line, showing the onset of rotating stall in CFD and experiments .....	74

Figure 5.3.	Time-record of mass flow rates for single-passage speed-line simulation at $N = 20640$ rpm .....	75
Figure 5.4.	Frequency spectrum of normalized mass imbalance, split between regions of stable and rotating stall operation for $N = 20640$ rpm line, for an onset point determined at 2.077 kg/s .....	76
Figure 5.5.	Velocity contours showing rotating stall at various flow rates on the $N = 20640$ rpm speed-line simulation. For each contour, the type of rotating stall found in CFD and experimentally is labeled for comparison. ....	78
Figure 5.6.	Mass flow rates for the $N = 19240$ rpm line, showing the onset of rotating stall determined in CFD and experiments .....	82
Figure 5.7.	Frequency spectrum of normalized mass imbalance, split between regions of stable and rotating stall operation for $N = 19240$ rpm line, for an onset point determined at 1.751 kg/s .....	83
Figure 5.8.	Velocity contours showing rotating stall at various flow rates on the $N = 19240$ rpm speed-line simulation. For each contour, the type of rotating stall found in CFD and experimentally is labeled for comparison. ....	85
Figure 6.1.	Incidence angle comparison for the original design .....	91
Figure 6.2.	Blade angle distribution for the original design and for two proposed re-designs ..	93
Figure 6.3.	Incidence angle comparison for the original design and Combo re-design .....	95
Figure 6.4.	Isentropic head coefficient and efficiency comparison between original design and various re-design options for $N = 19240$ rpm .....	96
Figure 6.5.	Comparison of flowpath area for the various designs .....	97
Figure 6.6.	Blade loading comparison between the Original and Combo designs, at near-design point $\phi_1 = 0.0531$ and $N = 19240$ rpm .....	100
Figure 6.7.	Blade loading comparison between the Original and Combo designs, at near-surge point $\phi_1 = 0.0426$ and $N = 19240$ rpm .....	101
Figure 6.8.	Time-record of mass flow rates for the $N = 19240$ rpm line, showing the onset of rotating stall for both the Original and Combo designs .....	104
Figure 6.9.	Frequency spectrum of mass imbalance for both Original and Combo designs for $N = 19240$ rpm line, split between regions of stable and rotating stall operation .....	105
Figure 6.10.	Velocity contours showing stable, transition and rotating stall operation on the $N = 19240$ rpm speed-line simulation for the Combo design .....	106

Figure 6.11. Time-record of mass flow rates for the  $N = 20640$  rpm line, showing the onset of rotating stall for both the Original and Combo designs ..... 108

Figure 6.12. Frequency spectrum of mass imbalance for both Original and Combo designs for  $N = 20640$  rpm line, split between regions of stable and rotating stall operation ..... 109

Figure 6.13. Velocity contours showing stable, transition and rotating stall operation on the  $N = 20640$  rpm speed-line simulation for the Combo design ..... 110

## NOMENCLATURE

$b$	Blade height	[mm]
$C$	Absolute fluid velocity	[m/s]
CFL	Courant number	dimensionless
$d$	Diameter	[mm]
$f$	Frequency	[Hz]
$H$	Head	[kJ/kg]
$K$	Blade angle design parameter	[degrees, °]
$M$	Normalized meridional distance along blade	dimensionless
$m$	Lobe number, number of rotating stall cells and direction	dimensionless
$\dot{m}$	Mass flow rate	[kg/s]
$\dot{m}'$	Normalized mass flow rate	dimensionless
$N$	Impeller rotational speed	[rpm]
$Q$	Volume flow rate	[m <sup>3</sup> /s]
$r$	Radius	[mm]
RSM	Rotating Stall Margin	dimensionless
$T$	Cycle period	[seconds]
$t$	Time	[seconds]
$U$	Blade speed	[m/s]
$v$	Fluid velocity	[m/s]
$W$	Relative fluid velocity	[m/s]
$\bar{W}$	Mean blade velocity	[m/s]

$Z$	Number of blades	dimensionless
$\alpha$	Absolute velocity angle, measured from radial direction	[degrees, °]
$\beta$	Relative velocity angle, measured from tangential direction	[degrees, °]
$\delta$	Incidence angle	[degrees, °]
$\Delta t$	Numerical time step size	[s]
$\Delta W$	Blade loading	[m/s]
$\Delta x$	Distance between two adjacent mesh points	[m]
$\eta$	Isentropic efficiency	dimensionless
$\lambda$	Blade loading coefficient	dimensionless
$\phi$	Phase angle	[degrees, °]
$\varphi$	Flow coefficient	dimensionless
$\psi$	Isentropic head coefficient	dimensionless
$\Psi_M$	Grid sensitivity metric	dimensionless
$\Omega$	Impeller rotational speed	[rad/s]
$\omega$	Rotational speed	[rad/s]

### Subscripts

1	Impeller inlet
2	Impeller exit
5	Diffuser exit
b	Blade value
BEP	Best efficiency point
bsl	Baseline for grid sensitivity metric



bc	Boundary condition
f	Fluid value
g	Geometric separation
h	Hub
imb	Imbalance
imp	Impeller
int	Rotor/stator interface
isen	Isentropic
LE	Blade leading edge
m	Meanline
p	Pressure fluctuations
ps	Pressure side
r	Rotor
RS	Rotating stall
s	Shroud
ss	Suction side
sta	Stage
t	Blade tip
TE	Blade trailing edge

# CHAPTER 1: INTRODUCTION

## 1.1 MOTIVATION

Centrifugal compressors have become very widely used in a variety of industries, which can be subdivided into two categories based on their design requirements: the process and power industry, which requires customized and reliable machinery; and the aircraft and turbocharger industry, which requires highly optimized, mass produced solutions [1]. The refrigeration and air conditioning industry falls mainly in the first category, but also has many applications in the second category. In the aircraft industry, design of centrifugal compressors is typically focused on producing a single, highly efficient design which is then scaled for different applications. These compressors are optimized to run at maximum efficiency at a fixed speed and flow rate. In the process industry, the focus is more on reliability than performance. In this case, each design is customized to its application in order to have a wide operating range and extended compressor longevity [2].

The operating range of a compressor is defined as the range of flow rates at which the compressor exhibits stable operation. The concept of stability in an inherently unsteady flow machine [3,4] comes in several varieties. Most commonly, unstable operation is qualified as any flow or operation that deviates from the compressor's normal operation. Technically, it should be qualified by the compressor's ability to achieve steady-state operation after experiencing a disturbance. If the compressor cannot achieve a steady-state condition, its operation is generally referred to as unstable [5]. In general, the operating range of a compressor is limited at both high and low flow rates by choke and surge, respectively. In the choked condition, the mass flow is large enough to achieve sonic condition, and cannot be increased further. Surge condition occurs

at very low flow rates, and is characterized by a full reversal of the flow through the compressor, also causing large radial and axial vibrations. The low flow limit of operation for an impeller is typically referred to as the surge line, as can be seen in Figure 1.1. However, this is a common misnomer, as in many cases the lower limit of operation is actually defined by the onset of instabilities such as stationary or rotating stall [6].

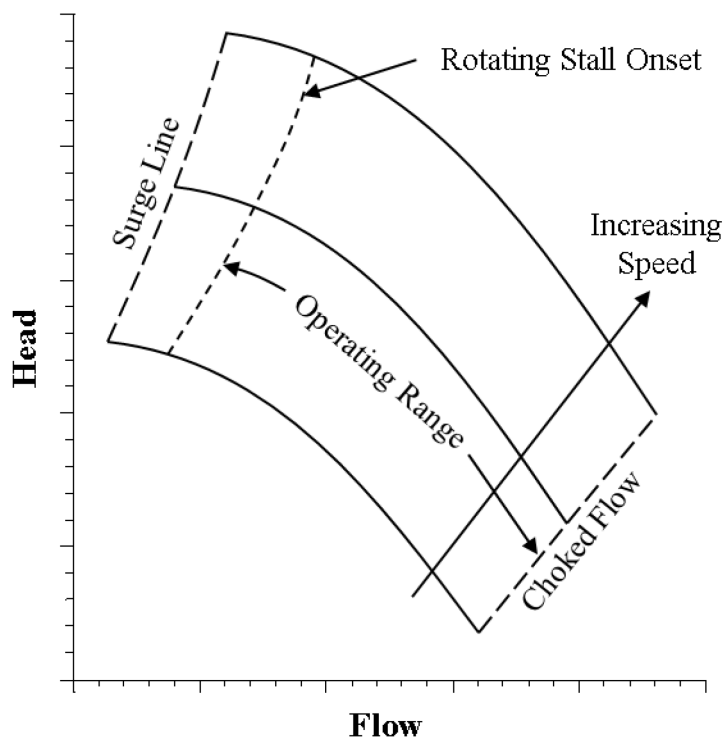


**Figure 1.1. Performance map showing the actual surge line and rotating stall onset line**

Stationary and rotating stall are typically precursors to surge, but are not always limited to low flow rates. Four types of instabilities can occur when approaching the surge line of a compressor: stationary stall, rotating stall, mild surge and deep surge. All of them involve flow recirculation zones, but to different extents. Stationary or non-rotating stall has been reported as small areas of reversed flow or low pressure oscillations that occur in stationary

components of the compressor stage, such as vaned diffusers, return channels or inlet guide vanes. The cause of stationary stall is typically attributed to large incidence at diffuser or return channel vanes or small radii of curvature in guide vanes, return bends or return channel vanes [7]. Rotating stall is also characterized by small areas of reversed flow, but these stall cells rotate relative to the stationary observer. Rotating stall may occur in the compressor's impeller, diffuser and return channel, but rotating stall in the return channel has been rarely reported [2,7,8]. Both rotating stall and stationary stall cause compressor performance to drop, but the recirculation zones in both cases are too small to affect the overall mass flow rate of the compressor [2,9]. Surge is differentiated from stall by the fact that it produces significant fluctuations in the flow rate of the machine. In mild surge, the flow rate through the system cycles periodically, but does not become fully reversed [2,10]. In deep surge, the flow reverses throughout the entire annulus of the compressor. Deep surge is the easiest of these phenomena to detect, as it is accompanied by loud flow oscillations and vibrations that easily harm the compressor. Rotating stall and mild surge can be hard to distinguish, especially in cases where rotating stall presents first and triggers the occurrence of mild surge [10]. It should also be noted that in a majority of axial compressors, surge is always preceded by rotating stall. However, in centrifugal compressors, surge may occur without the appearance of rotating stall [9].

In addition to reducing the performance of a compressor, rotating stall is also associated with subsynchronous blade vibrations [11,12,13,14,15]. The unstable flow patterns associated with rotating stall create pressure fluctuations on the blades, which in turn causes them to vibrate. The vibrations are of much higher frequency and lower amplitude than those seen during surge, but are still very harmful to compressors. This vibration transmits to the rotor shaft and can cause damage to the compressor seals and bearings, significantly reducing the life of the

machine. Figure 1.2 shows experimental results for a centrifugal compressor with a vaned diffuser from Haupt, Jin and Rautenberg [14]. Rotating stall presents at the low flow rates of the 13100 rpm and 13300 rpm lines, causing a significant increase in blade vibration.

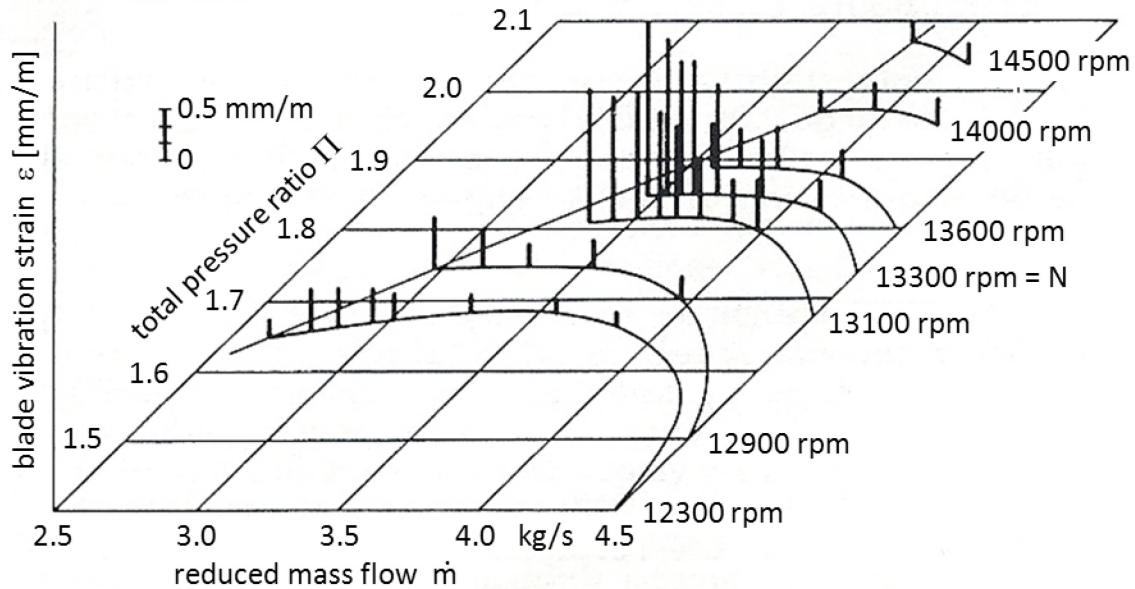


**Figure 1.2. Blade vibration measurements plotted on a compressor performance map, as recorded experimentally by Haupt, Jin and Rautenberg [14]**

Due to the issues with stability and blade vibration caused by rotating stall, compressor maps usually limit their operations to areas where rotating stall has not been observed during experimental testing. In cases where reliability and longevity are of importance, rotating stall can significantly reduce the operating range of the compressor, or forces a complete redesign in order to remove the instabilities. Ideally, designers would want to know if rotating stall will occur early in the design process. However, experimental testing is currently the only reliable method of detecting it. The objective of this work is to produce a reliable method of predicting rotating stall using commercial Computational Fluid Dynamics (CFD) software, well before the testing phase. With this method in place, it will be possible to redesign and test using computer

simulations, which saves time and money. Additionally, the simulations will lead to a better understanding of this phenomenon, allowing for corrective solutions and guidelines for better designs that avoid the formation of rotating stall.

## 1.2 ROTATING STALL CLASSIFICATION AND CHARACTERIZATION

As mentioned in the previous section, rotating stall is an unsteady flow phenomenon that involves rotating regions of reversed flow. Figure 1.3 shows a schematic example of impeller rotating stall, seen from the eye of the impeller. The flow distortions that make up rotating stall can present with multiple lobes, or cells, distributed equidistantly around the impeller passage. The number of cells commonly varies between 1 and 5, with 2-cell and 3-cell stall being the most widely reported [2,9,16]. The highest number of rotating stall cells detected experimentally is  $m = +6$  and  $m = +7$ , recorded for two different impellers tested by Haupt et al. [17] and Seidel et al. [18].

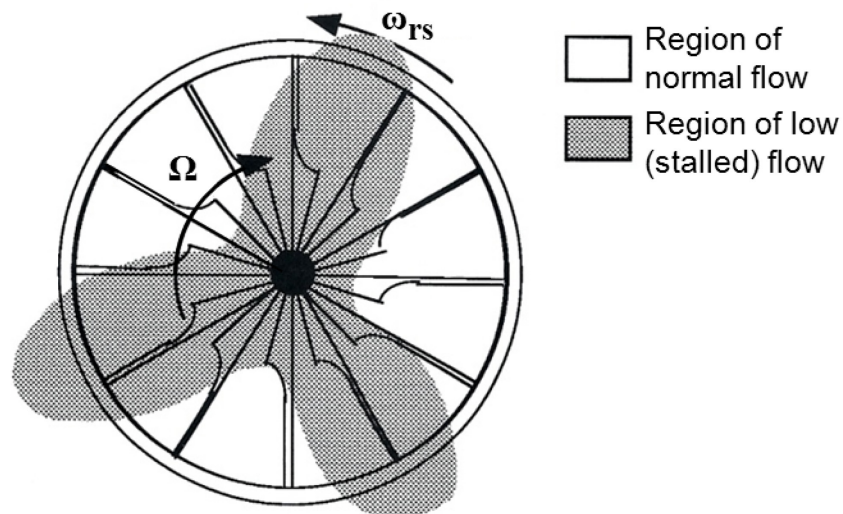


Figure 1.3. Rotating stall pattern corresponding to  $m = -3$  [9]

During operation in rotating stall, the stall cells develop due to the separation of boundary layers within the blade passages. However, the separated flow does not remain in the same passage as the impeller rotates, but rather propagates to an adjacent passage in the impeller. The various passages in the impeller each take turns stalling and then recovering, which causes the stall cells to rotate around the impeller. The rate at which they rotate is always less than the actual rotor speed. Unlike surge, the flow rate through the impeller is not decreased by rotating stall. The flow velocity in the stalled regions is reduced, but this causes the velocity through the surrounding passages to increase. As a result, the net mass flow rate through the impeller is maintained [8,9].

Rotating stall can be classified according to various definitions, such as its location, size, strength and cause. The first distinction is to classify it according to the component in which it occurs. While rotating stall may occur anywhere in the compressor stage, impeller rotating stall (IRS) and diffuser rotating stall (DRS) account for 90% of reported cases [7,9]. The location at which the separation occurs is also used to classify it as blade or wall stall. In blade stall, the flow separates from the blades of the impeller, while wall stall typically occurs as a separation zone caused by excessive shroud curvature or roughness [3]. The initial factor contributing to stall is used to distinguish it as incidence-induced or loading-induced stall. In incidence-induced stall, the decreased flow rate causes the incidence angle between the blades and flow to increase, which in turn causes a low speed zone to separate from the tip of the blades [2,8]. In loading-induced stall, flow separates further downstream, due to large pressure differentials across the blade passage [9]. The appearance of the stall on the performance curves is also used to differentiate stall types. Abrupt stall has a sudden onset and causes a sudden drop in the pressure characteristic. Progressive stall varies gradually with flow rate, growing smoothly as flow rate is

decreased [8,19]. Finally, rotating stall can be characterized as part-span or full-span stall by the size of the disturbance. If the stall cell is large enough to restrict the entire blade passage, from hub to shroud, it is referred to as full-span or deep stall. Instead, if the flow is restricted only for a portion of the blade passage, it is called part-span or mild stall. This is a common occurrence in axial compressors, but only one case has been reported for centrifugal compressors [2,8].

Characterization of different rotating stall occurrences is based on recording the number of stall cells, their rotational speed and the direction of propagation of the cells. The number of rotating stall cells and direction of propagation are both recorded in the variable  $m$  (in some sources  $\lambda$  is used instead), which is positive if the cells rotate in the same direction as the impeller, or negative if they rotate in the opposite direction. The example in Figure 1.3, page 5, shows an example of impeller rotating stall for  $m = -3$ . The speed of the cell's rotation,  $\omega_{rs}$ , is measured in Hz relative to the rotating impeller frame. However, it is most commonly reported in non-dimensional form relative to the impeller speed,  $\Omega$ , as the percentage ratio of  $\omega_{rs}/\Omega$ .

Much experimental work has gone into the classification of rotating stall throughout a compressor stage [8,20,21]. The results from Frigne and Van den Braembussche [8] provide a good metric for determining the type of rotating stall present from the rotational speed of the stall cells. They tested three compressor configurations, and found that three different types of rotating stall presented at unique speeds. Diffuser rotating stall occurred primarily at low rotational speeds of  $\omega_{rs}/\Omega \leq 20\%$ . Higher speeds were only detected for impeller rotating stall, and a further distinction could be made between abrupt and progressive onset stall. Abrupt stall rotated at 20% to 40% of the impeller speed, while progressive stall occurred at approximately 50% to 80% of impeller speed. Their results also showed that the development of progressive impeller rotating stall will completely suppress any diffuser rotating stall, but not vice-versa.



However, Abdelhamid [22] recorded that it is possible for abrupt impeller rotating stall and vaneless diffuser rotating stall to alternate at the same flow rate. Other researchers have confirmed but also widened the ranges given above. Jansen [16] claimed vaneless diffuser rotating stall to occur between 5% and 22% of impeller speed. Abdelhamid [20] claimed abrupt impeller rotating stall may occur between 20% and 50% of impeller speed. Mizuki et al. [23] reported progressive impeller rotating stall as high as 100% of impeller speed, while Kämmer and Rautenberg [24] reported it as low as 44%.

### **1.3 ROTATING STALL PROPAGATION**

The precise conditions that lead to the development of rotating stall are still not well understood. This section begins with an explanation of the development and propagation of impeller rotating stall for an axial compressor, as presented by Stenning [25] and Emmons et al. [26]. Axial compressor flow patterns are much simpler than centrifugal compressor flow patterns and the shorter length and easier accessibility to the flow passages has allowed for more in-depth investigation of the rotating stall phenomenon. Further in the section, some experimental results for centrifugal compressor stall are presented. The reversed flow patterns involved in centrifugal compressor stall are more complex, but some analogies to axial machines can be seen.

In axial machines, the leading cause for rotating stall is incidence, where the flow separates from the leading edge of the blade. The initial development of the stall zone can be triggered by manufacturing defects in the flow path or uneven pressure perturbations caused by upstream components in the flow. When the compressor blade row reaches the stall flow point, instead of all the blades stalling simultaneously, stall occurs only in small cells [3,26]. This can be explained by the fact that the mass flow through the impeller remains unchanged. As flow rate

is reduced, the incidence on the compressor blades is increased throughout the entire annulus. Once the incidence reaches the stall point, patches of retarded flow develop off the leading edge of some blades and the flow through the stall cell is reduced. The flow rate in the rest of the annulus is increased, which actually causes the incidence angles to drop below the stall point. This mechanism allows for the stall to exist as patches, instead of filling the entire annulus of the impeller.

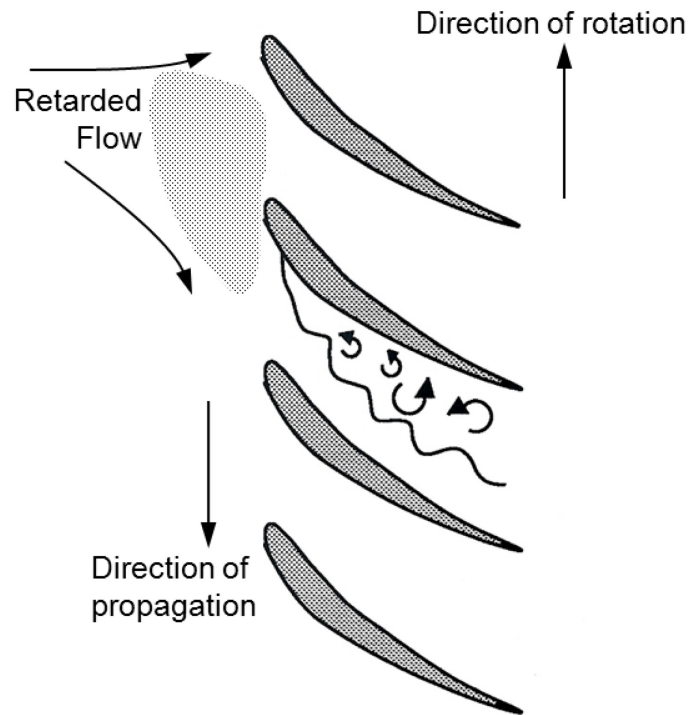


**Figure 1.4. Schematic of stall propagation in the direction opposite to impeller rotation [9]**

The propagation of the stall cells along the blade row is similarly explained. Once stall has developed in a blade passage, it creates an area of low flow before the leading edge of the blades, as shown in Figure 1.4. This retarded flow region forces the incoming flow to be diverted towards the blades on either side of the stalled passage. In the case depicted above, the diverted flow causes the incidence on the bottom blade to increase, and the incidence on the top blade to

decrease. Due to the increased incidence, the bottom passage will develop a separation zone and stall. At the same time, the decreased incidence on the top blade will allow the stalled passage flow to recover. The net effect is that the stall cell propagates downwards, rotating around the machine annulus in a self-sustained motion.

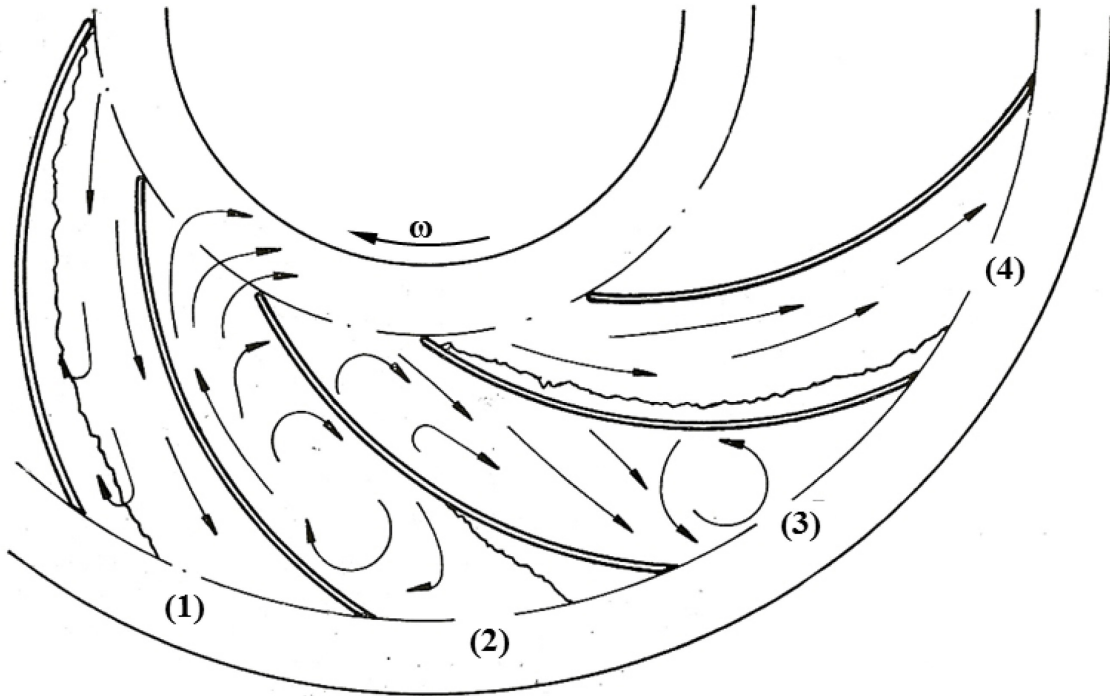


**Figure 1.5. Sequence of passage stall in a shrouded compressor impeller, as recorded experimentally by Lennemann and Howard [27]**

The flow pattern associated with impeller rotating stall was also investigated experimentally by Lennemann and Howard [27] using Hydrogen Bubble flow visualization in a centrifugal pump and by Krause et al. [28] using Particle Imaging Velocimetry in a radial pump. Their results give a better understanding of the flow fields and reversed flow regions in stall operation. Figure 1.5 shows their schematic for the rotating stall sequence in a shrouded compressor impeller. In passage (1), flow separates off the suction side of the blade and backflow occurs in the separated layer. This backflow grows and causes a blockage of the

impeller passage, which forces the entire flow to reverse in passage (2). The reversed flow moves out of the passage, into the inducer section and is forced into the next passage. The leakage around the leading edge allows the flow in passage (3) to recover and accelerate, forcing the reversed flow eddies back into the original flow direction. As the passage recovers fully (4), the separation along the suction side of the blade re-forms and eventually restarts the stall pattern.

Lennemann and Howard also performed the same experiment for an un-shrouded impeller, the results for which are shown in Figure 1.6. The stall sequence differs from that recorded for the shrouded impeller in that the initial separation that leads to stall occurs off the pressure side of the blade and different timing of the flow reversal. However, they are both characterized by an initial separation, followed by flow blockage through the passage, and reversed flow into the inlet around the leading edge of the blade.

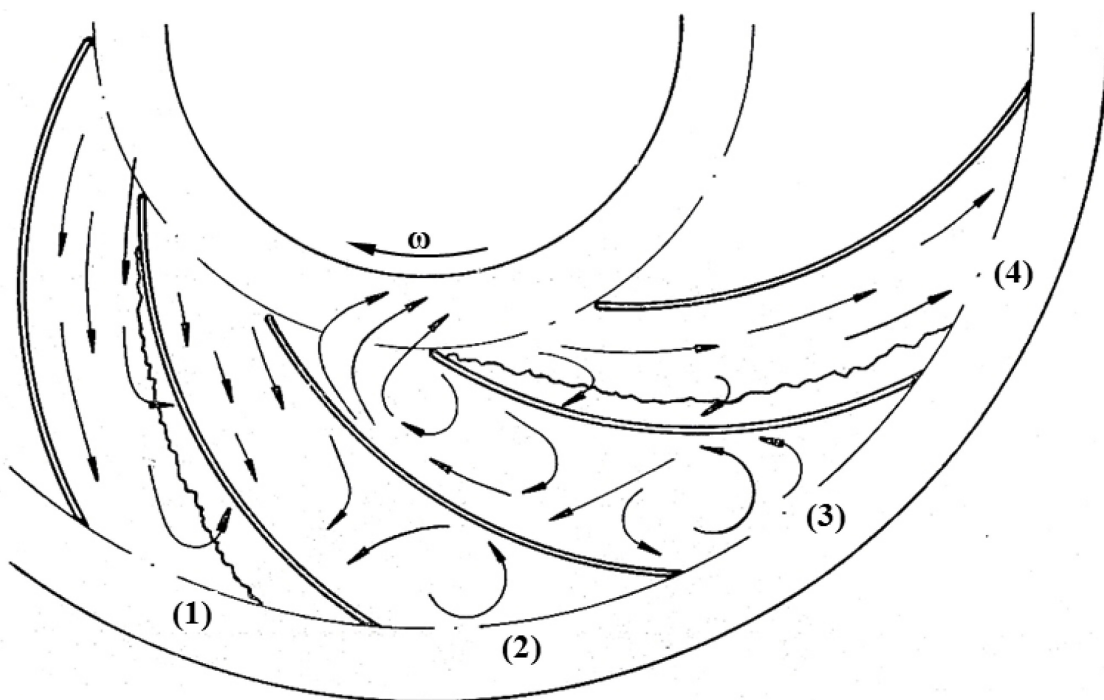


**Figure 1.6. Sequence of passage stall in an unshrouded compressor impeller, as recorded experimentally by Lennemann and Howard [27]**

The major breakthrough resulting from these flow visualization results was the confirmation of reversed flow areas in the impeller passages. It was seen that the boundary layer separation developed into reverse flow eddies, and the backflow around the leading edge of the blade allows the stalled region to propagate from passage to passage. If the separation layer did not develop into backflow, but rather remained the same size, there would be no cause for the stall cell to rotate around the impeller.

Another experimental study of interest was completed by J. Chen et al. [29] by recording the unsteady pressure fields in an unshrouded impeller with splitter blades. The pressure along the shroud casing was recorded at multiple instances in time during an operating point just after the development of rotating stall. The sequence of measured pressure contours recorded for an entire stall cycle is shown in Figure 1.7 on page 13. The plots are to be read in increasing numerical order. The contours labeled 6 and 8 show normal operation of the impeller while no recirculation is present. However, low-pressure zones develop off the suction side leading edge of the main blade and also directly before the splitter blade. The contours labeled 11, 16 and 20 show the impeller passage in a mixed operation, which corresponds to the un-stalled areas of an impeller undergoing rotating stall. A high-pressure zone crosses the passage from pressure to suction sides. The pattern suggests that two flows are developing in the impeller, a reverse flow at the trailing edge and a separation zone at the leading edge. The stalled flow pattern can then be seen in contours 24 and 26. Low-pressure regions form inside the splitter passage, indicating reversed or swirling flow in those areas. The low-pressure zone also moves across the passage from pressure to suction side. By the last image, labeled 4, the flow has recovered and returned to the normal operation pattern seen in the first images. The sequence can now repeat as the stall cell moves around the impeller again.

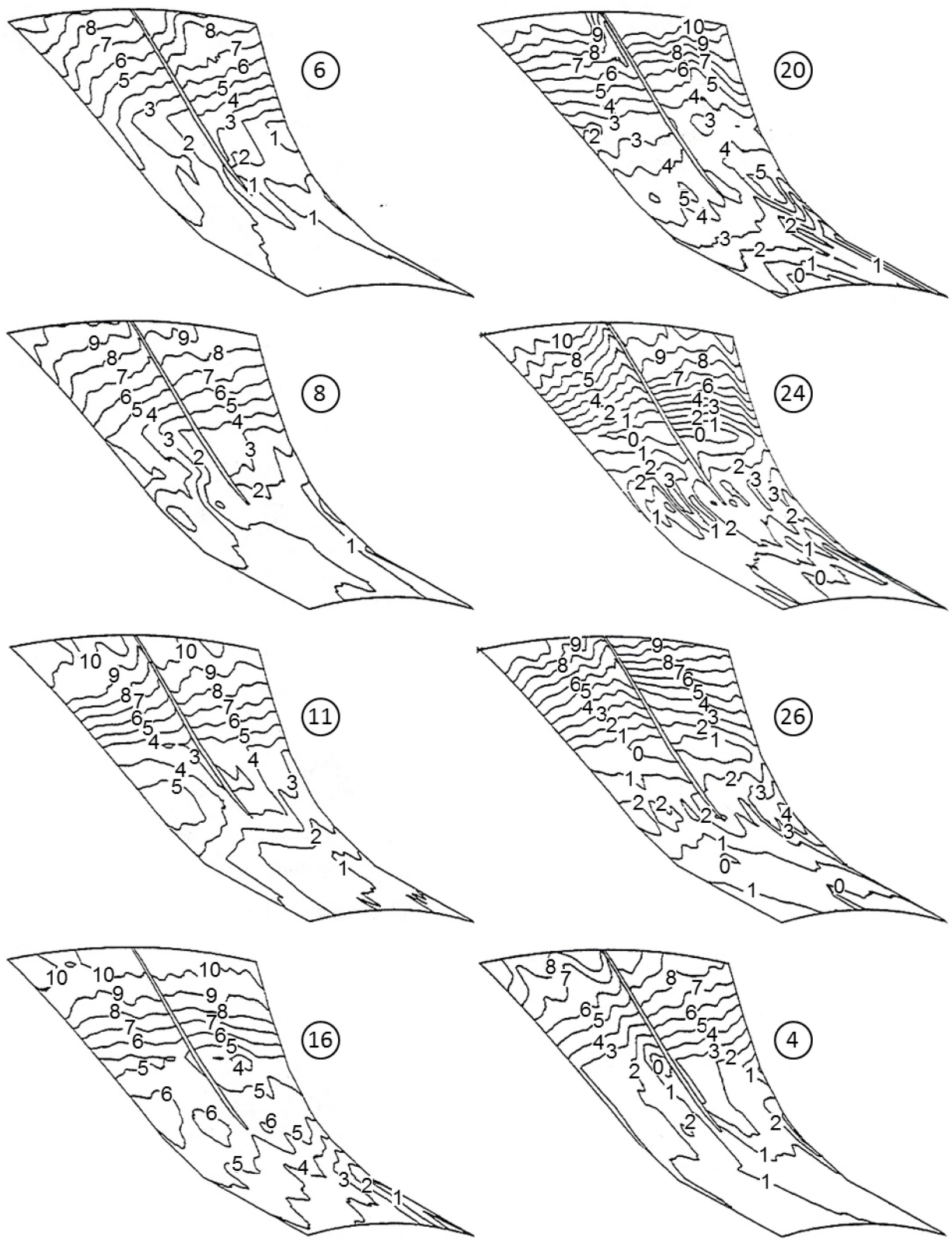


**Figure 1.7. Sequence of pressure contours during rotating stall in a centrifugal compressor impeller with splitter vanes, recorded experimentally by J. Chen et al. [29]**

The pressure contour results show a high-pressure and a low-pressure zone associated with rotating stall, which move across the impeller passage. The motion of these waves was studied by Y. N. Chen et al. [30,31,32,33], who suggested that the high-pressure and low-pressure zones move as waves across the entire compressor annulus. The motion of the secondary reverse flow matches the behavior of Rossby waves, a meteorological phenomenon. The Rossby wave links the reversed flow sections of the high-pressure zones (H) and low-pressure zones (L) and forces them to circulate around the impeller in a circular manner. This is shown schematically in Figure 1.8. The areas within the loop followed by the Rossby wave correspond to areas of stalled, reversed flow. The flow outside is in normal operation, with positive throughflow.

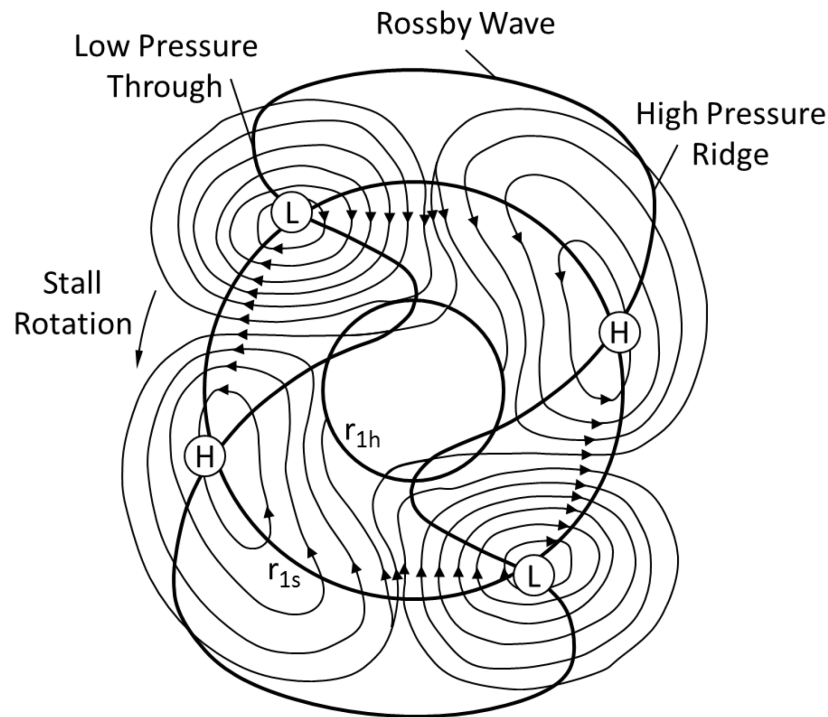


**Figure 1.8. Rossby wave, high (H) and low (L) pressure vortices producing the forward and reverse flows in rotating stall (adapted from Y. N. Chen [33])**

## 1.4 CORRECTIVE SOLUTIONS

Many of the corrective solutions that have been developed for rotating stall are specific to a certain type of impeller, diffuser, or a specific combination of the two. Therefore, some caution must be taken when applying them. Some of the solutions are preemptive: they provide criteria that help avoid situations where it is possible for stall to form. These can be applied in the design stage. Others are reactive: they provide guidelines on how to re-design compressor components if stall is detected during experimental testing.

For impeller rotating stall, three parameters have been found to be of importance in the design process. The first is the relative velocity ratio,  $W_2/W_{1t}$ , which must remain above 0.55. Impellers with lower values will have a tendency to experience stall. For designers using 2-D codes, the blade loading can be a useful parameter to predict stall occurrence. Locations where the variation in velocity between the suction and pressure sides of the blade,  $(W_{ss}-W_{ps})/\bar{W}$ , is in excess of 0.8 are likely to produce separated flow that initiates stall. Additionally, many designers often limit leading edge incidence angles to less than  $12^\circ$  to prevent leading-edge separation. However, this is not a very successful method, as the critical incidence is influenced by blade inlet angles, curvature and upstream flow conditions [7]. Adhering to these criteria generally helps reduce the occurrence of rotating stall, but not in every case [6]. Such design criteria may help designers, but are empirically based and may not work in design cases differing from those for which the criteria were developed.

For diffuser rotating stall, the main parameter designers look at is the absolute flow angle at the exit of the impeller,  $\alpha_2$ . A substantial number of researchers have published criteria for vaneless diffusers [8,16,22] and vaned diffusers [19,34,35]. Although the recommendations presented by these authors vary, the most stringent claim is to keep the exit flow angle above the



range  $\alpha_2 \geq 72^\circ$ . However, exceeding this value will not always lead to rotating stall, as the actual onset may vary depending on the type of stall and diffuser geometry. Senoo et al. [34] and Kobayashi et al. [36,37] developed empirical correlations for a critical diffuser inlet flow angle,  $\alpha_{2c}$ , with various corrections for diffuser geometry and thickness ratio,  $b_2/d_2$ . If the flow angle at the diffuser inlet exceeds this critical value, rotating stall is likely to occur.

Reactive solutions are applied after experimental testing of a compressor. They are typically rules of thumb that have been developed through experience in testing. For most cases, the exact mechanism that allows these corrections to work is not fully understood. They work by pushing the onset of stall further into the low flow portion of the compressor map, rather than actually eliminating the stall. This is done in an effort to widen the stable operating range of the compressor, but also can successfully eliminate the problem of stall if its onset is pushed past the compressor's surge line.

Compressor design experience has shown that some simple changes in the diffuser geometry can generally reduce the onset flow point of stall. Using a longer vaneless diffuser or reducing the thickness of the diffuser or return channel passage can all extend the operating range of a compressor [7]. Additionally, Sorokes [38] showed that the shape of the pinch area at the diffuser inlet can have a major effect on the inception of stall. Yoshida [39] showed that reducing the amount of vaneless space in a vaned diffuser can also push the onset of stall to a lower flow rate. In certain cases, rotating stall may be initiated by machining flaws in the flow passage. In such cases, a simple solution was to re-stagger the vanes in the diffuser [7] or return channel [40].

An important area of research in compressor applications is the development of control systems which automatically avoid rotating stall and surge. These systems fall into two

categories, passive control and active control. Passive control systems avoid stall and surge by forcing the compressor into a more stable operating point or expanding. Active control systems are designed to eliminate the stall and allow the compressor to operate in a range that was previously unstable.

The simplest control system to implement is a passive system that detects rotating stall and automatically increases the flow rate back to an acceptable flow. Basically, this allows the safety margin to be significantly smaller, so the compressor can run at operating points near the surge line which have a higher head or efficiency [41,42]. Other passive control systems involve bleed valves in the diffuser or moveable walls in the plenum/volute, but most of these systems also cause a reduction in the compressor efficiency [10].

The most effective method of controlling impeller rotating stall has been the use of air injection nozzles at the impeller inlet or in the diffuser. Since it has been proved that rotating stall is inevitably linked to reversed flow, removing the flow reversal is the most effective solution for stall suppression. Goto [43] demonstrated that by including injection nozzles evenly distributed around the shroud of the impeller inlet, it is possible to create a velocity discontinuity in a small layer of fluid around the blade tip. This discontinuity prevents the formation of reversed flow at the impeller inlet, so rotating stall has no means of developing. This was a passive control system, the jets would operate continuously. Day [44] developed an active control system where the jets would open only when rotating stall was detected. Stein, Niazi and Sankar [5,10] have also introduced the use of pulsating jets to actively control rotating stall when pressure fluctuations are detected in the inducer. The jets use bleed air from the diffuser and re-inject it to suppress the stall as it is forming.

One passive method to control vaneless diffuser stall would be to use retractable diffuser exit rings, as shown by Abdelhamid [35]. This uses two flow control rings at the diffuser exit, which are used to throttle the flow axisymmetrically. This increases the throughflow component of the flow, and decreases the flow angle to below the critical values. Another method of control would be to use variable geometry vanes in the diffuser, so the incidence angle between the vanes and fluid could be adjusted. This would require a fairly complex active control system, as the vanes would have to be adjusted for every flow point, otherwise the vanes may cause compressor performance to drop.

Control systems are an effective approach to dealing with the problem of rotating stall, but they provide a lot of challenges. Instrumentation and installation of actuators may be expensive, and the control systems need to be customized for each compressor. However, the systems are of interest because much of the efforts to model rotating stall numerically have been for the purpose of control.

## **1.5 NUMERICAL STUDIES OF ROTATING STALL**

Prediction of rotating stall has been an important area of interest in compressor development. However, the current state of technology does not provide a reliable method to predict stall formation before experimental testing. One-dimensional codes are often not adequate when assessing the potential for stall. Many compressors designed within the criteria described in Section 1.4 still result in rotating stall. Jansen [16], Abdelhamid [20], and Moore [45] all developed theoretical models for rotating stall prediction in vaneless diffusers. Jansen's results only correlate well with experiments where 2 stall cells are present, while Abdelhamid's results limited the number of cells between 1 and 3 and Moore's results are limited to weak

disturbances. This limits the number of cases for which their analyses apply. Mainly, most prediction schemes rely on one-dimensional or two-dimensional approximations of highly complex, four-dimensional (time dependent) flow profiles.

Due to the complex flow structure of rotating stall and the geometry of centrifugal compressors, detailed measurement of the flow field is difficult, if not impossible. It is still very uncertain what the flow pattern within a compressor during different types of rotating stall is like. The use of numerical simulations may provide a more cost-effective approach to this type of investigation. However, most three-dimensional codes developed are limited to analyzing steady-state flow in a single compressor passage. The primary challenge to numerical modeling of rotating stall is the asymmetric nature of the phenomenon. The stall cells are capable of disturbing the flow through multiple adjacent blade passages, while leaving the remaining passages in the rotor unaffected. This requires numerical simulations to model the entire compressor geometry rather than just a single passage around one blade. The increase in solution time is substantial and requires the use of large computing clusters.

There has been a relative amount of success in numerical studies of rotating stall in axial compressors and centrifugal pumps, listed in Table 1.1. In centrifugal compressors, capturing rotating stall has been challenging, summarized in Table 1.2. Few cases are reported, and they are mostly limited to diffuser rotating stall or impeller stall caused by tip clearance at the leading edge. Numerical simulations of full-span impeller rotating stall in centrifugal compressors were not found in literature.

**Table 1.1. Some documented cases of rotating instabilities in numerical simulations for various turbomachines**

	<b>Machine Type</b>	<b>R.S. Location</b>	<b>Solver Type</b>
Hoying et al. (1999) [46]	Axial Compressor	Rotor Blade Tip	In-house code (MIT)
März et al. (2002) [47]	Axial Compressor	Rotor Blade Tip	In-house code (NASA)
J.P. Chen et al. (2009) [48]	Axial Compressor	Rotor Blade Tip	In-house code (OSU)
Legras et al. (2010) [49]	Axial Compressor	Rotor Blade Tip	elsA ONERA
Wu et al. (2010) [50]	Axial Compressor	Rotor Blade Tip	EURANS
Choi et al. (2011) [51]	Axial Fan	Rotor	In-house code (Rolls-Royce)
Sano et al. (2002) [52]	Centrifugal Pump	Vaned Diffuser	SCRYU/Tetra
Lucius & Brenner (2011) [53]	Centrifugal Pump	Rotor	ANSYS CFX
Widmer et al. (2011) [54]	Pump-Turbine	Turbine & Guide Vanes	ANSYS CFX
Tani et al. (2012) [55]	Centrifugal Pump	Inducer	CRUNCH CFD

**Table 1.2. Documented cases of rotating stall in numerical simulations for centrifugal compressors**

	<b>Machine Type</b>	<b>R.S. Location</b>	<b>Solver</b>
Ljevar et al. (2006) [56]	Centrifugal Compressor	Vaneless Diffuser	2-D FLUENT
J.P. Chen et al. (2009) [48]	Centrifugal Compressor	Vaned Diffuser	In-house code (OSU)
Everitt & Spakovszky (2011) [57]	Centrifugal Compressor	Vaned Diffuser	Numeca FINE/Turbo
Stein (2000) [10]	Centrifugal Compressor	Rotor LE Blade Tip	In-house code (Ga.Tech)
Iwakiri et al. (2009) [58]	Centrifugal Compressor	Rotor LE Blade Tip	In-house code (Kyushu)

The majority of rotating stall research using numerical methods has been targeted towards axial compressors. In these machines, rotating stall typically occurs near the tip of the

impeller blades due to the tip clearance and wall effects. However, the main focus of this research has been towards determining the precursory signs of rotating stall in order to develop control or corrective solutions. For example, the results by J.P. Chen et al. [48], shown in Figure 1.9, demonstrate the effectiveness of using of air-jets to control and prevent stall. However, the research groups involved in axial rotating stall simulation developed their own codes, each tailored to a specific application or stall type. In fact, the only commercial solver that has claimed to successfully predict “periodically repeating unsteady effects” is the Harmonic Balance Method included in CD-adapco’s STAR-CCM [59], but the method has only been applied to axial machines.

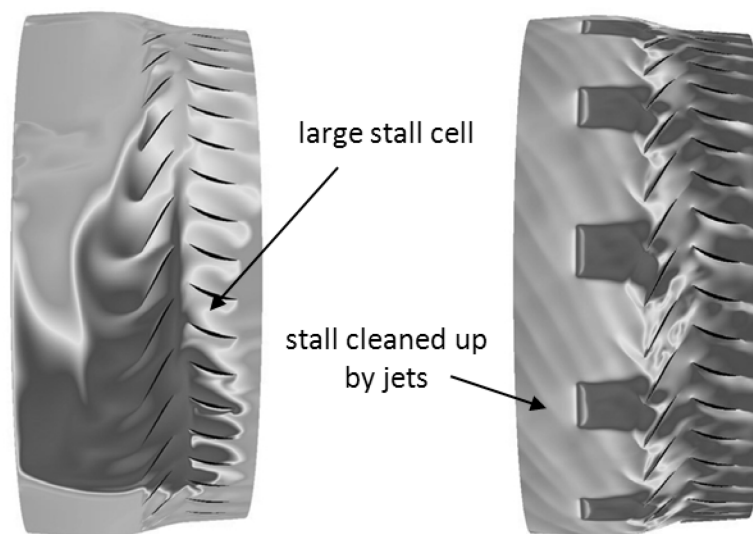


**Figure 1.9. Axial compressor rotating stall and the effect of inlet air jets for control (adapted from J.P. Chen et al. [48])**

Few cases are reported where numerical studies of centrifugal compressor rotating stall have been successful. For the most part, the stall in these cases has been located in the diffuser. Ljevar et al. [56] used a 2-D commercial code to capture a rotating instability in a vaneless diffuser. Using the code, they determined the stability limit in terms of  $\alpha_{2c}$  for this particular diffuser to be  $83.2^\circ$ , as shown in Figure 1.10.

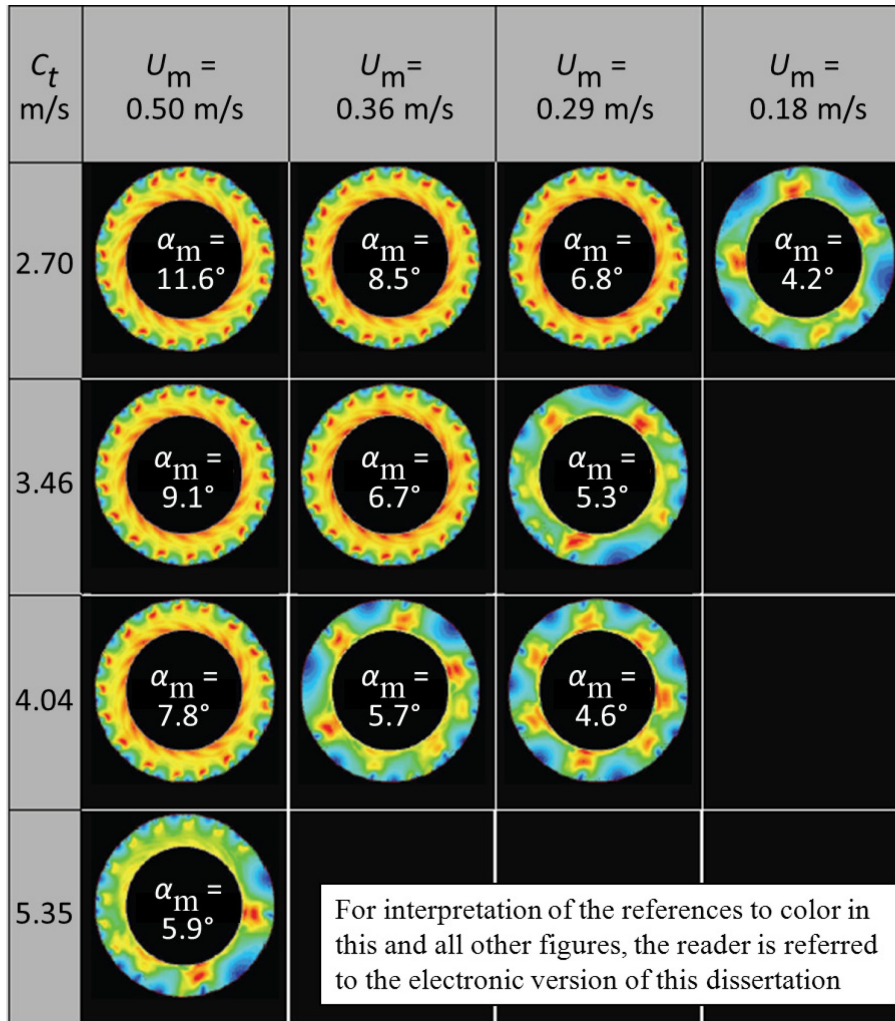


**Figure 1.10. Numerical simulations of stability limit for a vaneless diffuser [56]**

J.P. Chen et al. [48] also produced a code to determine if air jets would help relieve rotating stall in a vaned diffuser of a centrifugal compressor. The results, shown in Figure 1.11, show a small stall cell that develops along the leading edge of the diffuser blades. They also confirm that the air jets, located in the small dark regions of the velocity vector plots, help reduce the effect of rotating stall in the diffuser. In this case, the jets do not remove the swirl from the flow, but they do cause the throughflow velocity of the fluid to increase. Therefore, the incidence at the diffuser passage is reduced and the stall cell does not form.

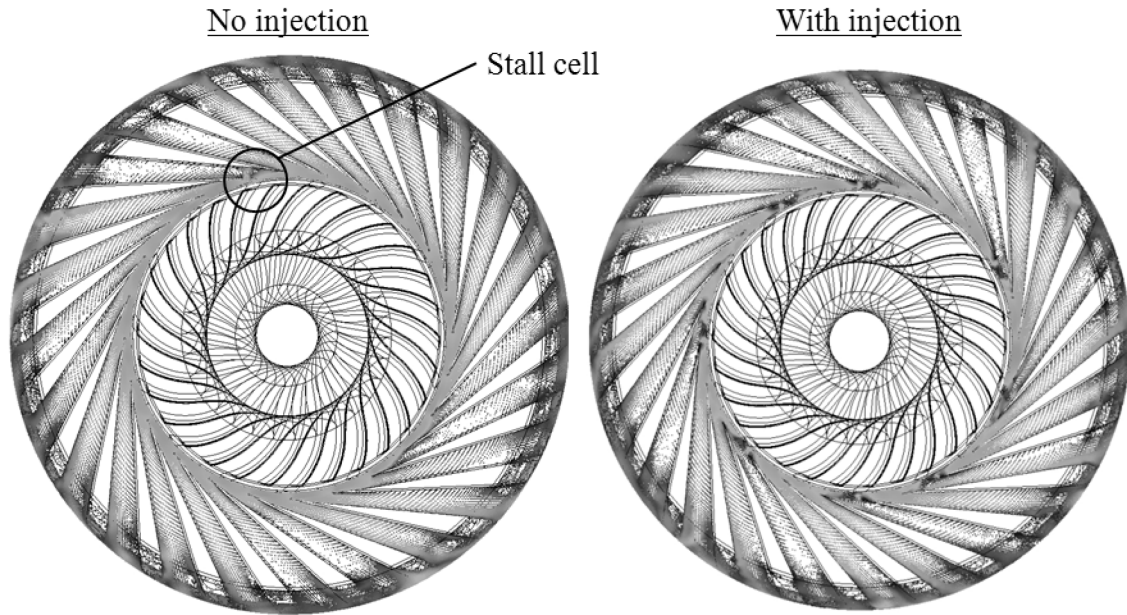


**Figure 1.11. Diffuser rotating stall control with air jets at the diffuser inlet (adapted from J.P. Chen et al. [48])**

The results by Stein [10] and Iwakiri et al. [58] are both for unshrouded impellers that show a similar type of tip stall to that present in axial compressors. Both developed in-house 3-D codes to detect impeller rotating stall, with Stein's again being for the purpose of air-jet control. The code was targeted to a NASA low-speed centrifugal compressor. The stall presented as a mild (part-span) case at the leading edge of the blades, shown in Figure 1.12. The images show instantaneous snapshots during the stall cycle,  $T_{RS}$ , in which backflow develops and recovers. While these two cases are the closest in literature to centrifugal compressor impeller stall, they are limited to part-span rotating stall caused by tip vortices off the impeller leading edge. No simulations of full-span impeller rotating stall are currently available in literature.



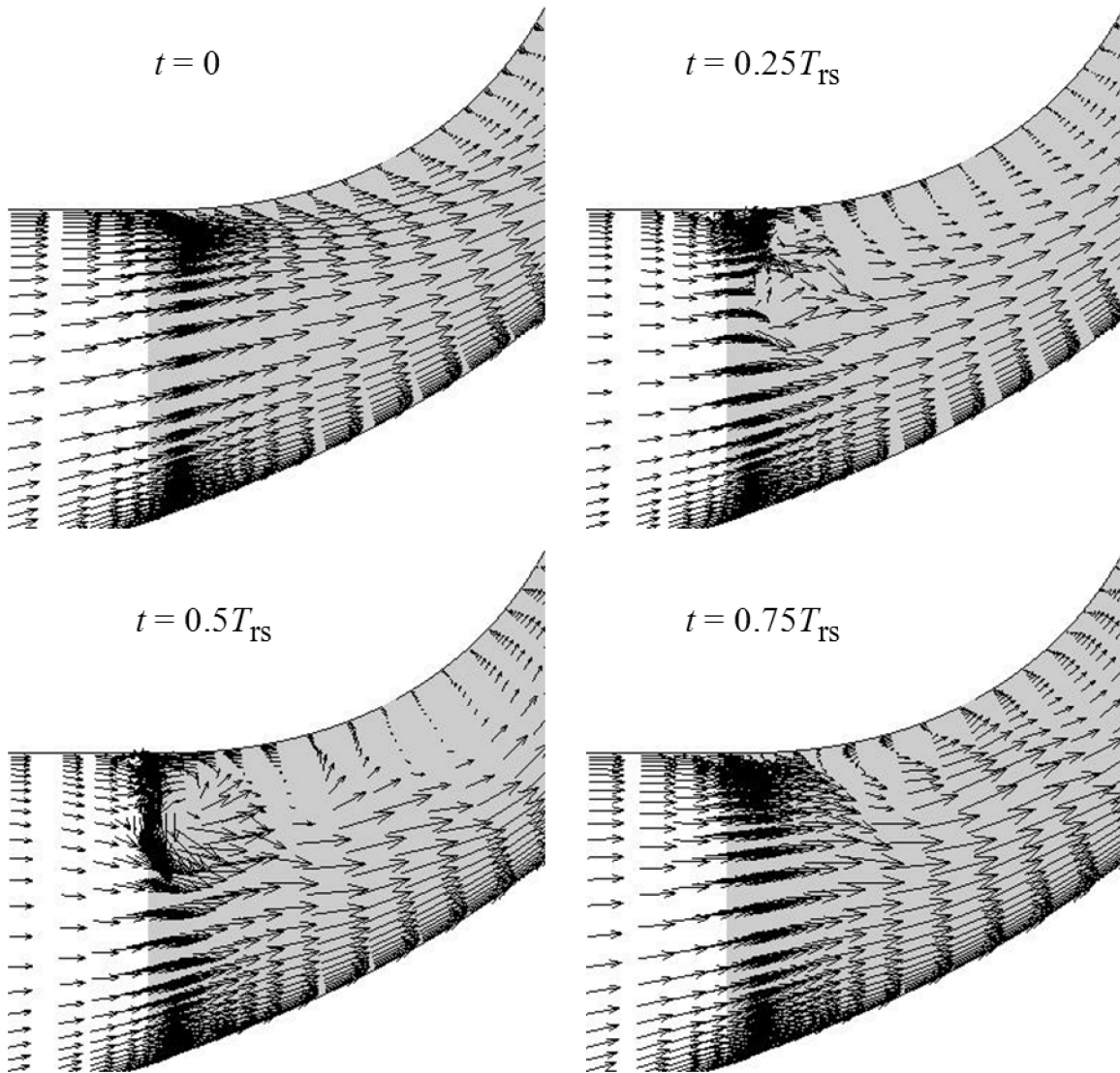


**Figure 1.12. Velocity vectors displaying backflow near the leading edge of a low-speed centrifugal compressor [10]**

In recent years, commercial CFD solvers have become more targeted towards the turbomachinery industry. Commercial software is able to model the unsteady flow in a centrifugal compressor much more accurately than in the past. Coupled with the ready access of high-performance computing, it should be possible to capture the rotating stall phenomenon using numerical simulations. Accurate modeling of stall in computational solvers will then allow for a better understanding of rotating stall flow fields and its causes.

## 1.6 OBJECTIVES

The significance of studying rotating stall instabilities in compressors is derived directly from the detrimental effects of rotating stall on performance. Eliminating stall will reduce vibrations, enhance the stable operating range, and increase the longevity of the compressor. The ability to predict its occurrence and to correctly model its development and propagation will enhance the knowledge base of this phenomenon. The use of computational simulations will allow for the prediction and elimination of stall well before the manufacturing and testing phase of the design process. The objectives for this work focus on two main categories of rotating stall research: developing a procedure to predict and characterize rotating stall, and determining a design methodology or criterion to avoid its formation.

Prediction of rotating stall will be completed using a commercial CFD solver that is already used heavily by compressor designers in industry. Successful modeling of instabilities in CFD is already a challenge, and the first step will be to determine a CFD setup that will generate a rotating stall cell that matches the flow patterns expected from literature. That includes the selection of a proper mesh, simulation time step, turbulence model, and solver schemes. The numerical results will also be compared to experimental results for the same compressor. In all the cases mentioned in Section 1.5, the unsteady simulations were performed at operating points where rotating stall was known to occur. These types of simulations help validate CFD analysis of rotating stall, but do not help with determining the actual onset flow rate of the phenomenon. The numerical simulation methods developed will be used to determine a simple method of successfully predicting the onset of rotating stall.

The numerical simulations that are used to predict the occurrence of rotating stall should also provide some insight into the development of rotating stall in the tested compressors. This

will help isolate the root cause of stall in the compressor. The compressor geometry will then be re-designed in order to avoid the flow condition that leads to the creation of the stall cell. The modifications should maintain the performance parameters of the compressor, while eliminating the development of stall cells or pushing the stall onset near the surge line for the compressor. The simulation methods developed to test for rotating stall will then be used to determine if the re-design is successful. Determining which geometric corrections help avoid rotating stall will help develop a design criterion to be applied in the initial design stages for centrifugal compressors.

# CHAPTER 2: EXPERIMENTAL COMPRESSOR TESTING

## 2.1 COMPRESSOR SELECTION

The compressor chosen for modeling was a single stage from a Solar Turbines Inc. high-pressure industrial compressor, dubbed the C2-HP Pipeliner. The stage consists of a shrouded impeller with a vaneless diffuser designed for a multi-stage pipeline booster. The impeller was tested at Solar Turbines facilities as an intermediate stage for a multi-stage compressor, including an inlet guide vane, a vaneless diffuser and a return channel. This compressor was selected for further investigation because it consistently had rotating stall develop along multiple speed lines during experimental testing. As part of the testing program, the compressor was then re-tested with a different return channel, but the rotating stall remained.

**Table 2.1. Test rig geometry for selected centrifugal compressor**

$d_{1h}/d_{1s}$	0.731
$d_{1s}/d_2$	0.639
$b_2/d_2$	0.054
$d_5/d_2$	1.898
$b_5/b_2$	0.850
$Z$	15

The impeller and diffuser geometry is given in Table 2.1. The design point for this impeller was at  $\phi_1 = 0.054$  and  $N = 19240$  rpm. Testing was performed along five different speed lines: 13100, 16020, 19240, 20640, and 21870 rpm. For each speed line, the compressor was tested at eight flow points, spaced evenly between choked flow and surge. Rotating stall was actively monitored, and if a signal appeared the onset flow rate and type of stall were recorded.

## 2.2 TEST SETUP

The C2-HP compressor was tested at the Solar Turbines Aero Test Facility. A description of the test setup follows, focusing mainly on the details regarding the detection and characterization of rotating stall. For more details on the general operation and capabilities of the test stand, see the publications by Cave et al. [60,61].

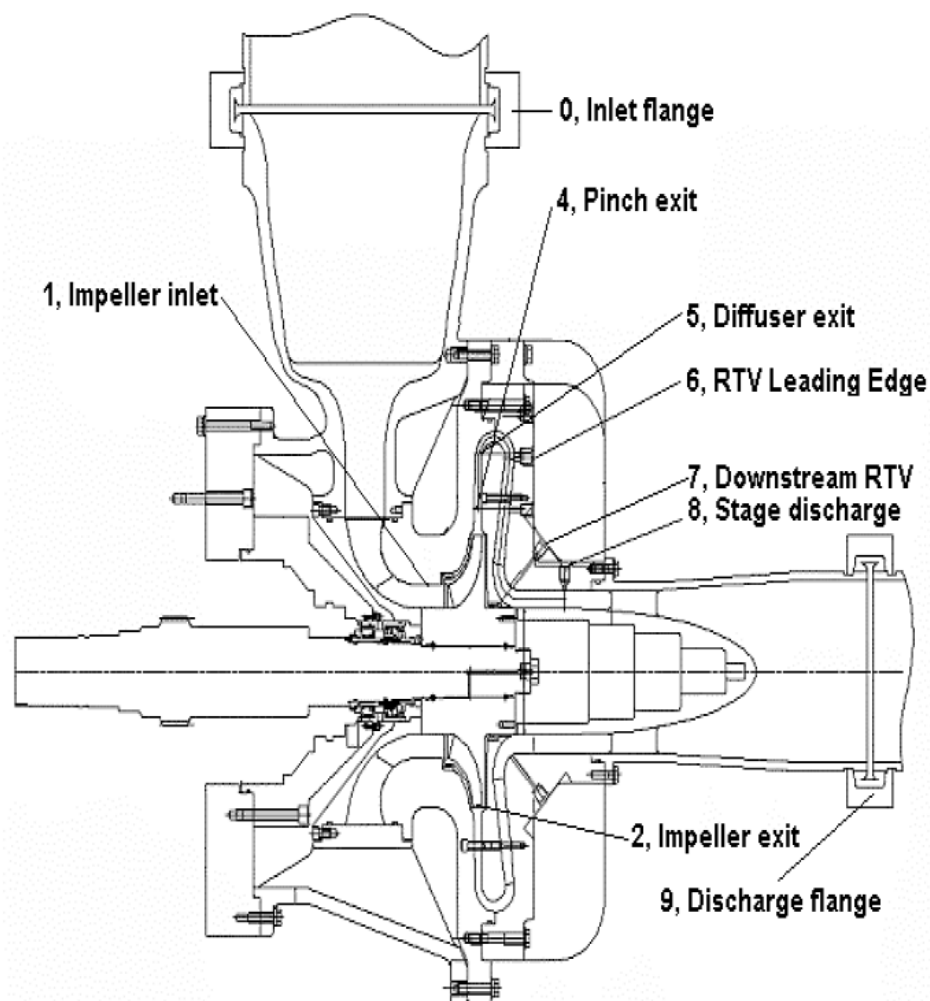


**Figure 2.1. Solar Turbines test facility schematic [60]**

The test stand is set up to test a single compressor stage as an intermediate stage in a multi-stage compressor. All the stage components are easily exchanged or replaced within the

rig. For the test configuration for the C2-HP compressor, this included an inlet with guide vanes to straighten the flow, a shrouded impeller, a vaneless diffuser, and a vaned return channel. The test stand is set up for closed-loop operation. After the return channel, the air passes through three control valves that are used to set the flow rate of air in the loop, which is measured using a venturi upstream of the compressor inlet. A heat exchanger is used to cool the air coming out of the compressor back to the required inlet temperature. The impeller is driven by a variable frequency electric motor coupled to a gearbox.

The experiments are setup to complete performance and flow measurements. Static pressure and temperature measurements are recorded at various locations along the compressor. The flow rate is controlled and measured. Pressure rise and efficiency are calculated based on the measured data. Additionally, flow measurements are taken at various accessible locations using three-hole probes. The velocity and flow angle are measured across the span at each of these locations. Compressor vibrations are also monitored using proximity probes, but are not used to monitor for the subsynchronous vibrations that may be caused by rotating stall.

Rotating stall is measured using dynamic pressure taps located in the diffuser section of the test rig. Three dynamic pressure transducers were placed at a radius of 12 inches and positioned at separation angles of  $50^\circ$  and  $210^\circ$ , as is shown in Figure 2.2. Rotating stall was characterized using the data from these measurements, following the methods of Whitbeck [9] and Abdelhamid et al. [62]. The time-series data recorded through the dynamic pressure taps was processed using FFT analysis. For operating points without rotating stall, a single peak was visible at the rotating frequency of the machine. For operating points with rotating stall, one or more additional peaks were recorded at a lower frequency. The frequency of the peak and its

corresponding phase angle were recorded and used to determine the number of cells and rotational frequency of the stall.

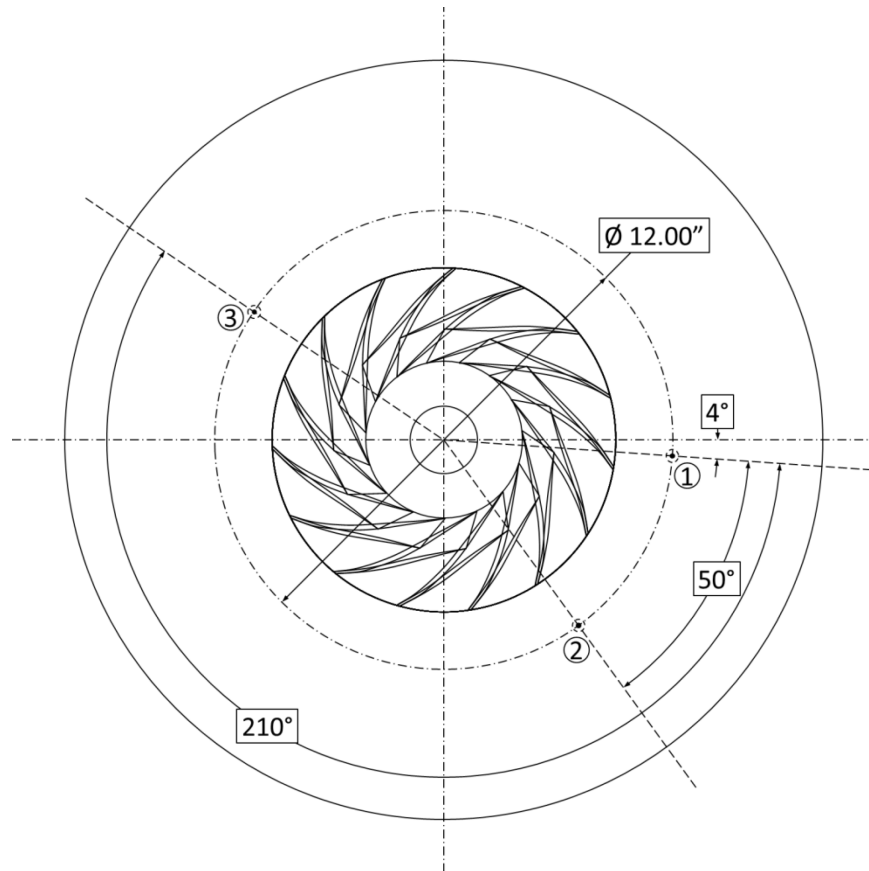


**Figure 2.2. Dynamic pressure measurement sites in the diffuser**

If the compressor was operating with rotating stall, the pressure signals from the transducers would show periodic fluctuations. By comparing any two signals, FFT correlation analysis would provide the amplitude and frequency content of the signals, and the phase angle between them. The signal would therefore contain one peak at the frequency of these pressure fluctuations,  $f_p$ . More harmonics may show up at higher frequencies, and should be ignored. For each peak, a phase angle,  $\Delta\phi_{TS}$ , was recorded and used to determine whether the additional peaks are harmonics. If the ratio of phase angle of the high-frequency peak to the phase angle of the

low-frequency peak matched with the ratio of their frequencies, the high-frequency signal is just a harmonic of the low-frequency signal.

The phase angle between the two signals was also used to determine the number of the rotating stall cells. Since the actual geometric angle between the transducers is known,  $\Delta\phi_g$ , it is possible to correlate the phase between the signals and the angle between the transducers to the number of rotating stall cells:

$$m = \frac{\Delta\phi_{rs} \pm k \cdot 360^\circ}{\Delta\phi_g} \quad (2.1)$$

where  $k$  is any integer necessary to keep the ratio as an integer. The sign of  $m$ , which corresponds to the direction of the stall rotation, is set by determining which signal precedes the other.

Take, for example, a compressor with dynamic pressure taps separated by  $\Delta\phi_g = 50^\circ$ . If a single stall cell is rotating in the direction of the impeller, the phase angle recorded between pressure peaks would be  $\Delta\phi_{rs} = 50^\circ$ . With  $k = 0$ , the lobe number is  $m = +1$ . If the stall cell rotates opposite the impeller, the phase angle recorded would be  $\Delta\phi_{rs} = 310^\circ$ . Therefore, using  $k = -1$ , the lobe number is  $m = -1$ . However, if two cells are rotating in the direction of the impeller, the pressure peaks in the signal would appear twice in a single rotation, doubling the recorded frequency. The phase angle would also double because the time difference between the readings of the two transducers is constant, resulting in  $\Delta\phi_{rs} = 100^\circ$ . As before, with  $k = 0$  the lobe number is  $m = +2$ .

To avoid ambiguous readings, all three transducers must be used. The lobe number was first determined using the above method using transducers 1 and 2, placed  $50^\circ$  apart. Then it was repeated using transducers 1 and 3, placed  $210^\circ$  apart. The results for both cases must match. This method was most easily implemented using a graphical approach. To determine the lobe



number, lines for  $m = \pm 1, \pm 2, \pm 3, \pm 4$  and  $\pm 5$ , are plotted on a diagram for different values of phase angles and separation angles, as shown in Figure 2.3. Two vertical lines are plotted at the separation angles for the two cases ( $\Delta\phi_{g1-2} = 50^\circ$  and  $\Delta\phi_{g1-3} = 210^\circ$ ). The phase angles were measured experimentally, and if they both match the intersection for the same number of cells, the lobe number was confirmed. For example, for a lobe number  $m = -3$ , the two phase angles must be  $\Delta\phi_{rs1-2} = -150^\circ$  and  $\Delta\phi_{rs1-3} = 90^\circ$ .

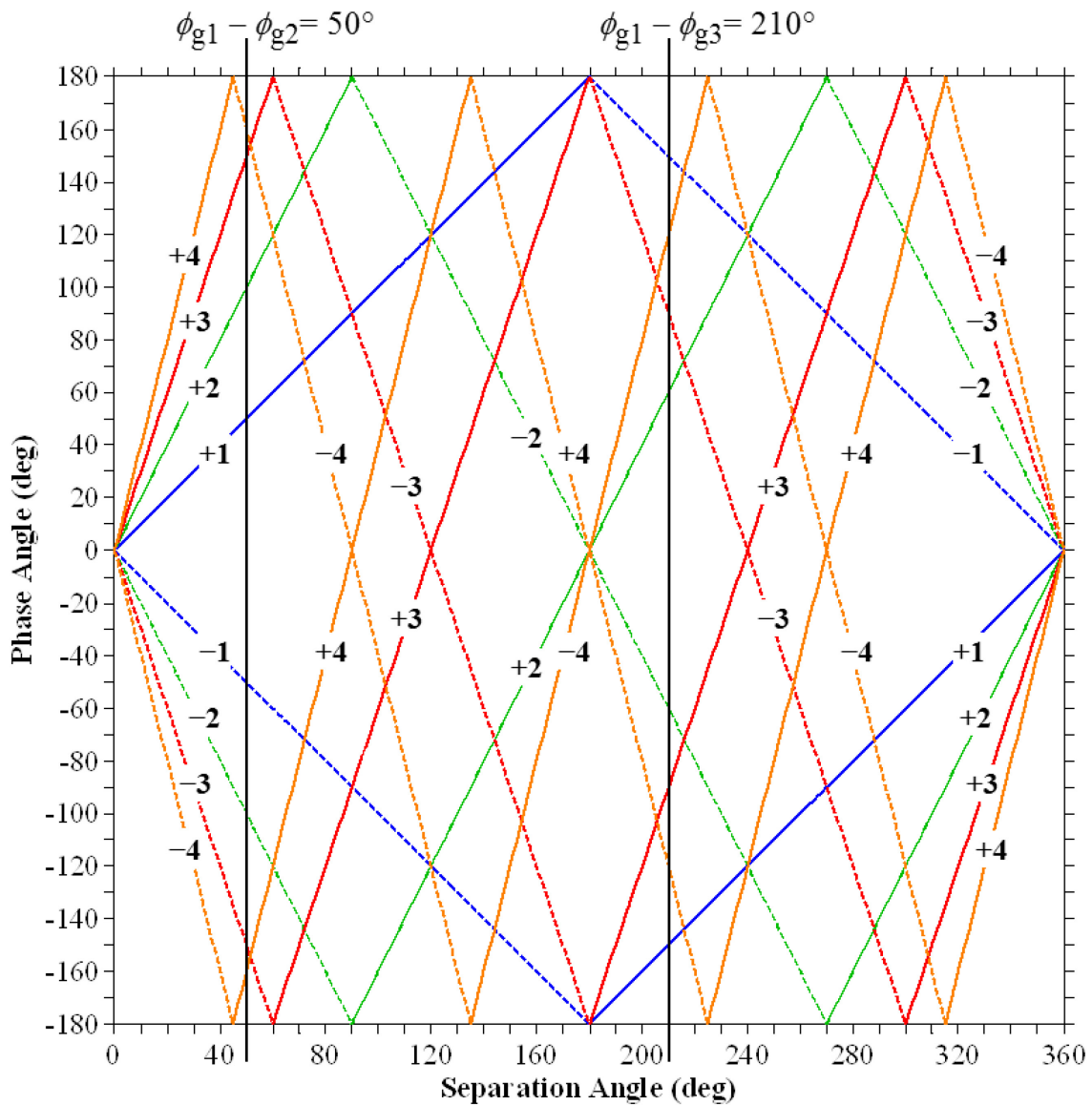


**Figure 2.3. Graphical method for determining number of stall cells**

The relative propagation speed of the stall cells was evaluated from the frequency of the pressure fluctuations,  $f_p$ , and the known rotor speed,  $f_r$ :

$$\frac{\omega_{rs}}{\Omega} = \frac{f_p}{m \cdot f_r} \quad (2.2)$$

In order to do this, the number of cells must be known. For a single cell, the fluctuations in the pressure traces must match the frequency of the stall. For two cells, the pressure fluctuations will pass the same transducer twice in one rotation, so their frequency is doubled. Therefore, for multiple cells the frequency of the pressure fluctuations must be divided by the number of stall cells in the pattern.

### 2.3 RESULTS

Performance tests were completed for this compressor with two different sets of return channels (RTVs): the original return channel designed for the C2-series of compressors, and a reduced return channel designed for the A2-series of compressors which have a lower flow rate than the C2-series (approximately a 58% reduction in area). The purpose of the modified tests was to determine if changing the return channel would have an effect on rotating stall. The flow path geometries for both cases are shown in.

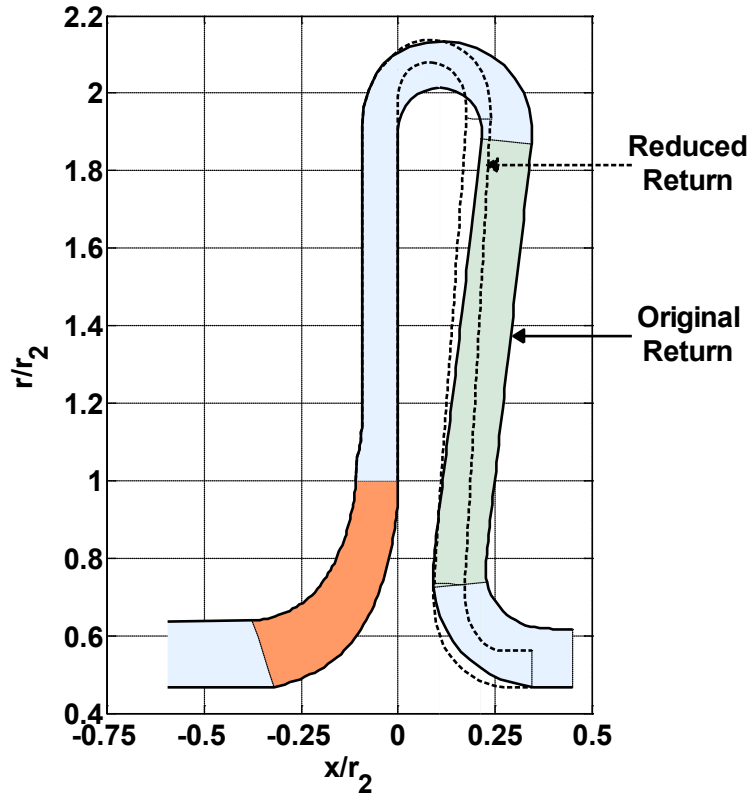


**Figure 2.4. Comparison of flow path between original return channel and reduced flow return channel**

The original tests were completed at all five speed lines: 13100, 16020, 19240, 20640, and 21870 rpm, and the second tests were completed only for the 13100, 19240 and 21870 rpm speed lines. The performance maps for both cases are plotted on Figure 2.5, on page 37. For each data point tested, rotating stall was monitored. Following the methods given in Section 2.2, if stall was present, the lobe number and rotational frequency were recorded. The results are summarized in Table 2.2, for the tests using the original return vanes, and in Table 2.3, for the tests using the reduced return vanes.

**Table 2.2. Experimental rotating stall onset points with the original return channel**

<b>Speed, <math>N</math> (rpm)</b>	16020	19240	20640		21870
<b>R.S. Onset flow rate, <math>\varphi_1</math></b>	0.0434	0.0524	0.0551	0.0472	0.0561
<b>Lobe number, <math>m</math></b>	+ 2	+ 2	- 3 & - 5	+ 2	+ 2
<b>Rotation Speed, <math>\omega_{rs}/\Omega</math></b>	12.4%	10.3%	2.0% & 9.6%	9.6%	9.1%

For the original experiments, two forms of stall were recorded. The dominant form was characterized as  $m = +2$ , and was present in four of the five speed lines tested. This rotating stall did not track with compressor speed, but rather rotated at a frequency of 33.13 Hz for all tested speeds, which on average corresponds to about 10% of the impeller speed. An intermittent form of stall was also recorded on the 20640 rpm line. For flow coefficients  $\varphi_1 \leq 0.0472$ , the dominant +2 cell stall pattern was found. Preceding that flow rate, in the range  $0.0551 \leq \varphi_1 \leq 0.0472$ , an intermittent form of stall presented with  $m = -3$  and  $m = -5$ . The low, constant rotational speed for the  $m = +2$  rotating stall fell within the typical ranges for diffuser rotating stall.

**Table 2.3. Experimental rotating stall onset points with the reduced return channel**

<b>Speed, <math>N</math> (rpm)</b>	13100	19240		21870	
<b>R.S. Onset flow rate, <math>\varphi_1</math></b>	0.0376	0.0392	0.0528	0.0504	0.0587
<b>Lobe number, <math>m</math></b>	+ 2	- 4	+ 5	+ 5	- 3
<b>Rotation Speed, <math>\omega_{rs}/\Omega</math></b>	86.5%	21.3%	24.3%	24.5%	25.0%

In the results for the reduced return vanes, the flow rate and isentropic head decrease, as can be seen in Figure 2.5. This also results in a decrease in efficiency. This effect was expected, as the reduced return channel was not designed for the C2-HP compressor. Instead, the interest was in how the new return channel would affect rotating stall. As with the original tests, the new results also showed a dominant form of rotating stall preceded by an intermittent form. In the

new configuration, rotating stall appeared on all the speed lines, including the 13100 rpm line that did not have any instability in the original tests. At the lowest speed line, the compressor experienced impeller rotating stall, as shown by its high rotational speed. At the other two tested speeds, a dominant and an intermittent form of stall were recorded. At both speeds the intermittent stall appeared at a higher flow rate than in the original RTV tests, and then dissipated as flow rate decreased. As the flow rate decreased further, the dominant stall appeared at flow rates similar to those in the original RTV tests. The rotating stall onsets for both sets of tests are also plotted on the performance curves in Figure 2.5, but only for the dominant form of rotating stall, not the intermittent kinds that preceded it. The results for the reduced RTV tests showed additional instabilities that were not present in the original tests. Additionally, the stall presented as impeller rotating stall, but showed many similarities with the diffuser rotating stall results from the original tests. It is possible, as shown by Abdelhamid [22], that the intermittent stall may be caused by the impeller, which leads to the eventual development of diffuser rotating stall.

The experimental results for this compressor showed a highly unstable operating regime. Due to the large areas of the performance map affected by rotating stall, especially since they are near the design and peak efficiency points, the stable operating range of this compressor is significantly reduced. This is true for both the original and the modified return channels. Therefore, the compressor was deemed not viable for industrial implementation. However, these same characteristics made it a good choice for further investigation using unsteady CFD.

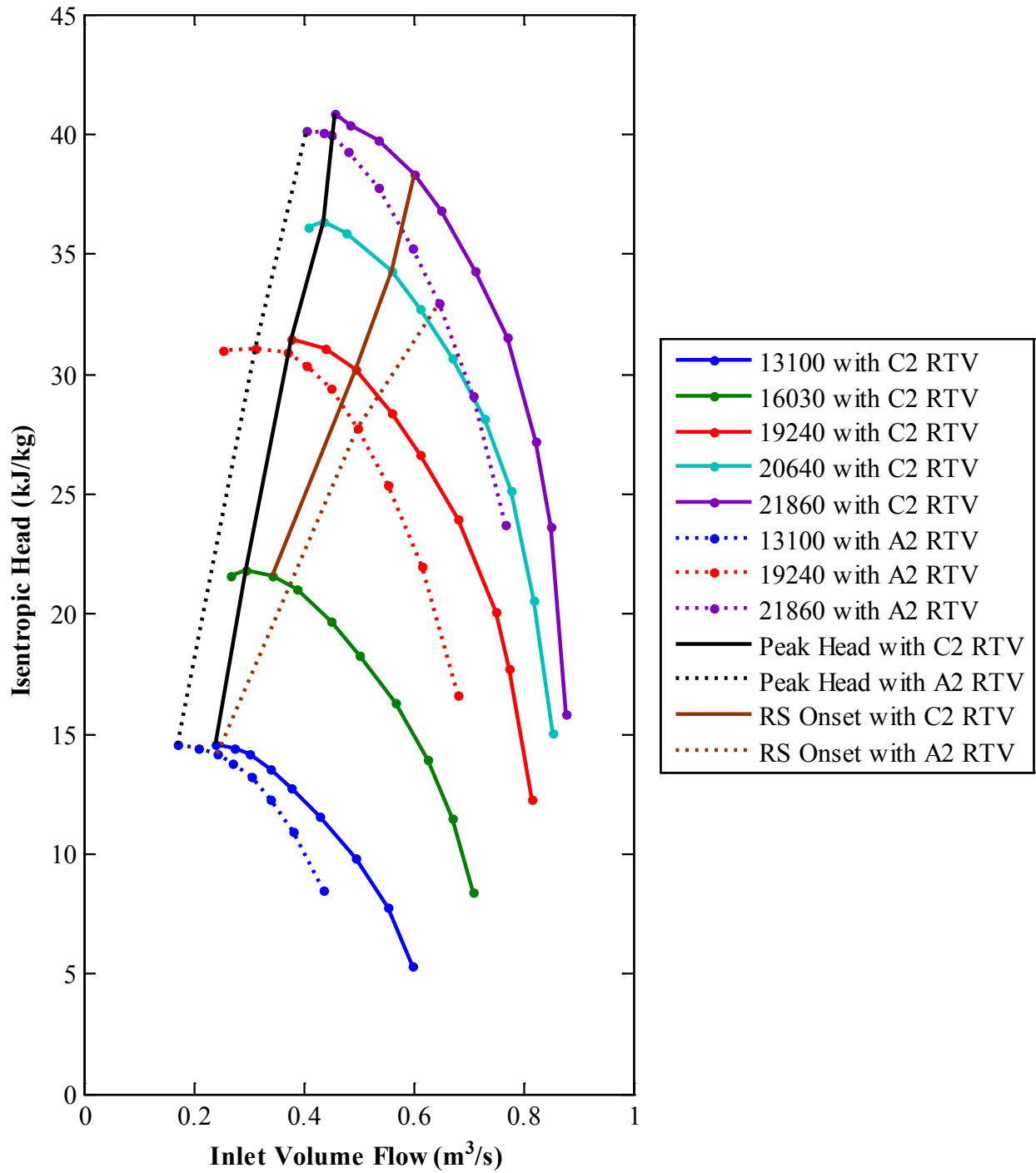


Figure 2.5. Test results for C2-HP compressor with C2 (original) and A2 (reduced) return channels

## **CHAPTER 3: METHODOLOGY**

### **3.1 THE INVESTIGATION PLATFORM**

Prediction of rotating stall requires the investigation of the three-dimensional flow profiles in the compressor, and how these profiles vary with time. Therefore, the solver must be capable of accurately modeling the complex flow through the compressor in both steady-state and transient simulations. Additionally, the solver must allow for the choice of various turbulence models that have proven accuracy in compressor applications. Due to the unsteady nature of rotating stall and the size of the grid required, the chosen solver must have parallel-processing capability, in order to keep solution times within reasonable limits. Finally, the CFD code must be readily available to compressor engineers and must already have the tools required to model centrifugal compressor geometry. For these reasons, the commercial code ANSYS CFX was chosen to complete the investigation.

Compressor modeling and grid generation for the simulations were completed using ANSYS BladeGen and TurboGrid. In order to capture rotating stall, a full 360° mesh of the compressor must be generated. The grid was first generated for a single passage, as is the common practice, and then copied around the circumference to produce the full mesh. The simulation setup and accuracy of the solver and partitioning were validated by comparing a set of steady-state computational results to experimental results. Grid sensitivity studies were completed to try to reduce simulation time without sacrificing solution accuracy.

Aerodynamic analysis of the compressor operation was performed using ANSYS CFX. It is commercially available software that is commonly used in the process industry. The software solves the discretized Reynolds Averaged Navier-Stokes (RANS) equations, including the total

energy equation, allowing for multiple choices of turbulence models. For turbomachinery applications, these include the  $k-\varepsilon$  and  $k-\omega$  two-equation models and the Reynolds-stress transport models. Selection of the turbulence model will be discussed further in Section 3.4. For the simulations, the fluid was modeled as air as an ideal gas. In order to use the transient solver, a realistic initial condition is necessary. The steady-state solver was used to produce an initial set of results to be used as the starting point for the transient CFD runs.

In order to complete the large-scale simulations required for this application, parallel processing on a set of high-performance computing servers was necessary. This uses the “divide and conquer” approach: splitting the simulation domain between various high-performance servers, rather than solving the entire simulation on a single machine. This allows for a significant reduction of computation time. The choice of the number of processors will have an effect on both the solution time but also on simulation accuracy. The effect of partitioning the domain between multiple processors was studied to determine the best number of processors to use for the simulations.

Two separate approaches were taken to simulate rotating stall in the compressor. The first method was used as a baseline to determine if the mesh, transient time step, and turbulence models were chosen correctly for the purpose of capturing rotating stall. Since the transient simulations for this method are set up so that the compressor mass flow rate is maintained constant, for the purposes of this paper they will be referred to as “fixed-flow simulations.” By testing flow rates at which rotating stall is known to happen for experiments, it could be confirmed if the simulations were modeling it correctly.

For compressor design, it is of interest to be able to predict at which flow rates on the compressor map rotating stall happens. The purpose of the second approach taken for the



transient simulations was to predict the flow rate where rotating stall first develops: the onset point. For a constant compressor speed, the transient simulations were set off at a flow rate that is known to be stable. After one full revolution of the compressor impeller at this flow rate the mass-flow boundary condition was suddenly dropped to a lower value. This was repeated once per revolution. The concept is similar to that of typical compressor testing, where a valve is used to decrease the flow rate through the compressor from choke to surge. By decreasing the mass flow rate in small increments, a stability range for the specific speed line could be determined. In this paper, these simulations will be referred to as “speed-line simulations.”

### **3.2 STEADY-STATE VALIDATION**

Validation of the CFD results was first completed by comparing a set of steady-state results to the experimental results obtained for the same compressor. For this purpose, a single-passage model including the return vanes was used, shown in Figure 3.1. The steady-state simulation was performed with a uniform, axial inlet with specified total pressure and temperature and with a fixed mass-flow outlet after the return vanes. The working fluid was air, modeled as an ideal gas. The high resolution advection scheme was used. The turbulence model chosen was  $k-\varepsilon$  with first order upwind scheme, with all the wall boundaries modeled with a surface roughness height of 1.6 microns. The inlet was specified with medium turbulence intensity of 5%. The rotating speed of the impeller was fixed, and frozen rotor interfaces were used at the inlet-rotor interface and the rotor-diffuser interface. The convergence criteria were set for the max residuals to be less than  $1 \times 10^{-4}$  residuals and the domains to have at least a 1% mass-flow conservation target.

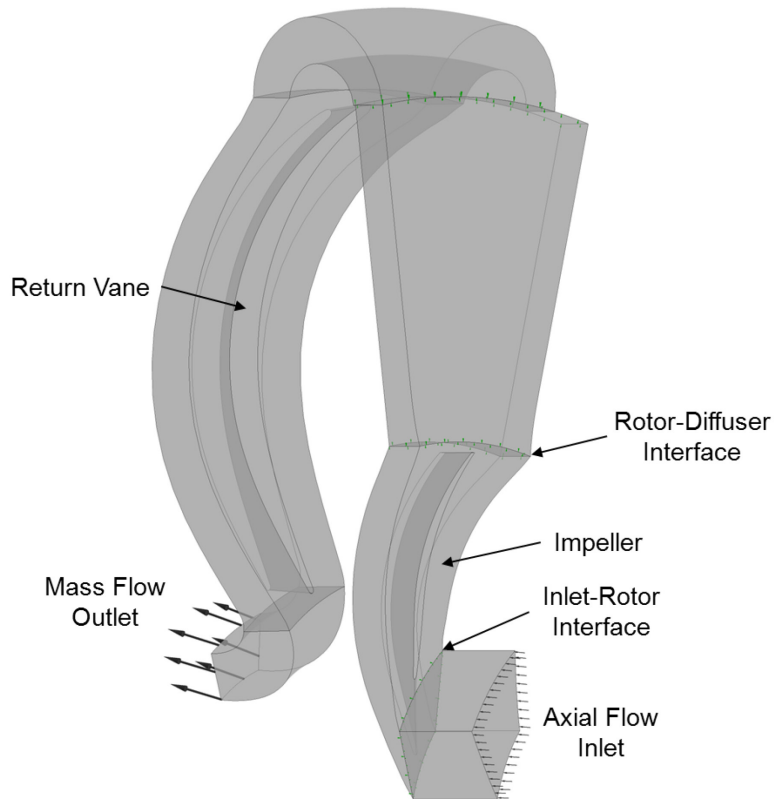


**Figure 3.1. Schematic of impeller model used for CFD validation, with boundaries and interfaces**

Seven simulations were completed at different flow coefficients at design speed,  $N = 19240$  rpm, and compared to the experimental results for the same speed line. These are shown in Figure 3.2, comparing the isentropic head coefficient, and the isentropic efficiency of the experimental and computational results. The head and flow coefficient definitions used are given in Equations (3.1) and (3.2). The results are comparable, with the computational head and efficiency being slightly higher than the experimental results, which is to be expected. On average, the computational head coefficient is higher by 2.8%, while the efficiency is higher by 6.1%. However, since rotating stall presents at low flow rates near surge, the range of interest for this investigation may be limited to  $\phi_1 \leq 0.06$ . In this range, the difference between experimental and computational head coefficient is only 0.3% and efficiency is only 4.4%. These results correlate well and are sufficient to give confidence in the accuracy of the CFD modeling used.

$$\psi = \begin{cases} \left(\frac{1838}{d_2}\right)^2 \frac{H_{isen}}{N^2} & \text{in English units} \\ \left(\frac{854.4}{d_2}\right)^2 \frac{H_{isen}}{N^2} & \text{in SI units} \end{cases} \quad (3.1)$$

$$\phi = \begin{cases} \frac{700.3}{d_2^3} \frac{Q}{N} & \text{in English units} \\ \frac{24.318}{d_2^3} \frac{Q}{N} & \text{in SI units} \end{cases} \quad (3.2)$$

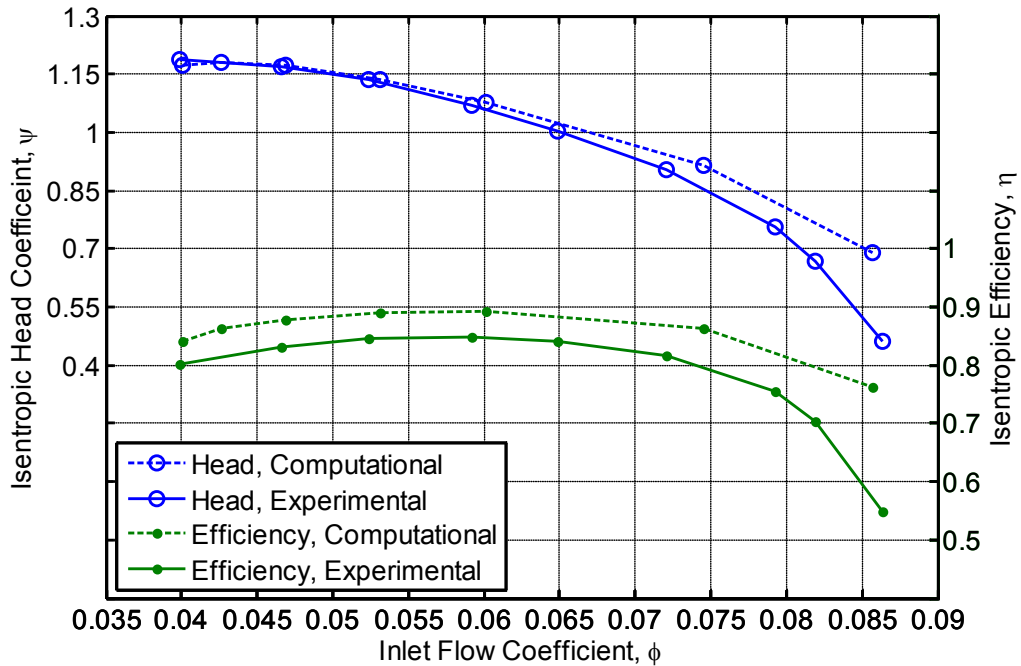


**Figure 3.2. Isentropic head coefficient and efficiency comparison between experimental and steady-state numerical results at  $N = 19240$  rpm**

### 3.3 360° GRID GENERATION

The development of an appropriate computational grid is the most important factor to completing the CFD simulations in a timely and accurate manner. The common practice for modeling rotating turbomachinery is to analyze a single impeller passage, setting up periodic

boundary conditions so the flow in the rest of the machine will match the flow within the analyzed passage. Rotating stall appears as one or more cells of retarded flow; it is not present in all passages at once. Additionally, rotating stall affects more than one passage at a time, as it propagates from one blade passage to the next. As a result, it was not possible to model just a single passage of the impeller. A full 360° mesh was required to model rotating stall. As with any other CFD mesh, the full 360° mesh must produce accurate results while keeping solution times within an acceptable limit. With such a large mesh, simulation times were increased by various orders of magnitude compared to single-passage meshes.

In order to reduce computational time, the return channel was not modeled. The experimental results for this impeller (Table 2.2 and Table 2.3) showed no significant improvement of rotating stall with either of two return channels, so it was concluded that the return channel does not affect the development of rotating stall in this impeller. The diffuser was modeled up to the beginning of the return bend, at  $d_5$ . This allows for a large reduction in the size of the model and, therefore, a significant reduction in solution time.

Grid generation was first completed for a single-passage. After a grid sensitivity study, the selected mesh was used to construct the full 360° mesh. Since boundary layer separation is a typical cause for rotating stall, special care was taken to ensure the mesh near the blade surfaces was adequate. Following compressor designer experience, the  $y^+$  values at the blade surface were kept below 300. Additionally, the mesh near the interface between the impeller and diffuser was kept at a finer quality than the rest of the diffuser, in case the interaction between the diffuser and rotor was the cause of the rotating stall, as may be the case for stall that presents with low rotational speeds.

To study the accuracy of the grid, a set of three single-passage meshes were developed using coarse, medium and fine densities. The single-passage meshes were then solved using the steady-state CFX solver at the compressor design point. The simulation results were compared to determine which single-passage mesh would produce accurate results while significantly reducing calculation time. The accuracy of the simulations was measured using the finest mesh as a benchmark. The dimensionless performance parameters (inlet and outlet flow coefficient, isentropic head coefficient and efficiency) of the other meshes were normalized by those of the finer mesh and averaged to produce a single metric for simulation accuracy,  $\Psi_M$ , defined in Equation (3.3). Table 3 shows the accuracy for three different single-passage meshes.

$$\Psi_M = \frac{1}{4} \left( \frac{\varphi_1 - \varphi_{1,bsl}}{\varphi_{1,bsl}} \right) + \frac{1}{4} \left( \frac{\varphi_2 - \varphi_{2,bsl}}{\varphi_{2,bsl}} \right) + \frac{1}{4} \left( \frac{\psi - \psi_{bsl}}{\psi_{bsl}} \right) + \frac{1}{4} \left( \frac{\eta - \eta_{bsl}}{\eta_{bsl}} \right) \quad (3.3)$$

**Table 3.1. Grid accuracy for single-passage meshes**

	<b>Mesh nodes</b>	<b>Accuracy, <math>\Psi_M</math></b>
Single-Passage	533774	Baseline
Single-Passage	275494	0.38%
Single-Passage	96768	0.77%
Full 360°	4065825	0.45%

To continue to a full impeller mesh, the accuracy limit was chosen as  $\Psi_M \leq 0.5\%$ . The medium-density mesh was the coarsest mesh within this range. The full 360° mesh was then created by copying the selected single-passage mesh into a full impeller. This increased the number of mesh points by a factor equal to the number of blades, in this case 15. The 360° mesh was again checked for accuracy by completing a steady-state run at the same operating point.

The same accuracy metric was used as for the single-passage meshes. For the 360° mesh, the accuracy metric remained within the required range. A small change is expected, as the periodic boundaries are not present in the simulation anymore, but the accuracy should not deviate significantly from the accuracy of the single-passage mesh used to create it. Figure 3.3 and Figure 3.4 show close-up views near the leading and trailing edges of the impeller of the full 360° mesh, with 4 million nodes, that was created for the simulations.

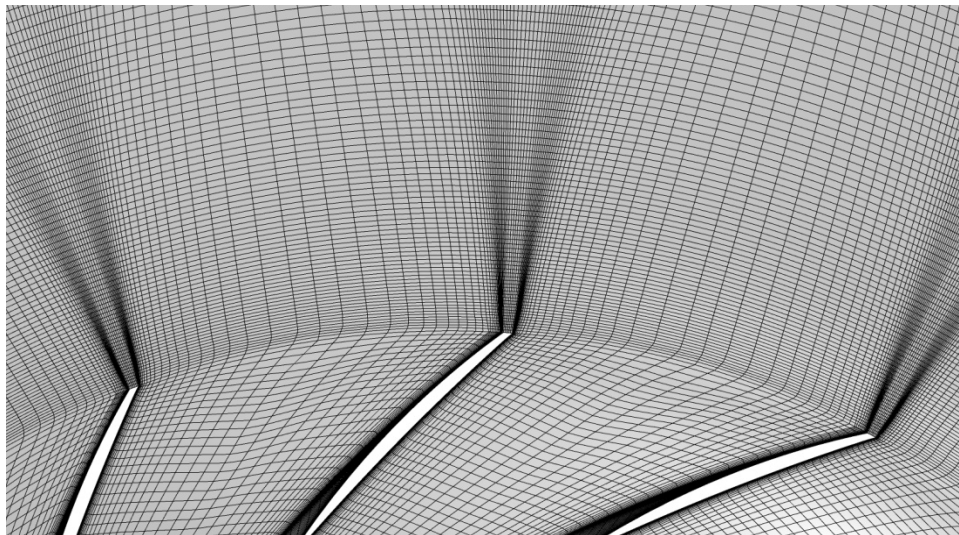


**Figure 3.3. Detail of full 360° mesh used for simulations, near blade trailing edge**

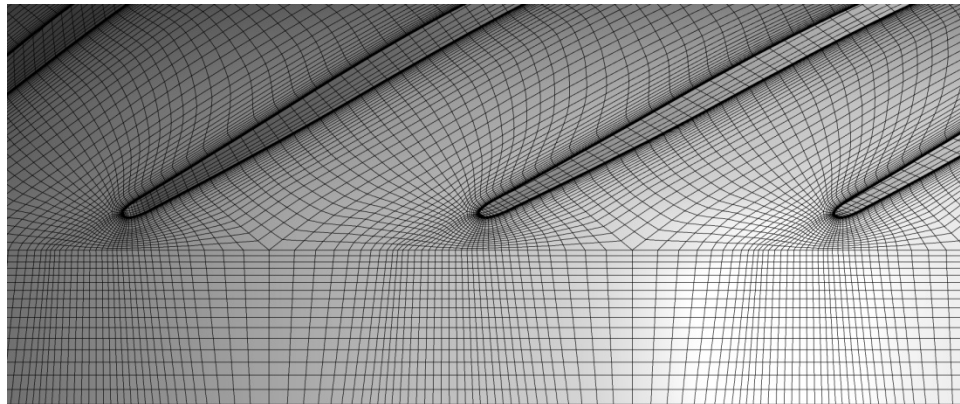


**Figure 3.4. Detail of full 360° mesh used for simulations, near blade leading edge**

### 3.4 TURBULENCE MODELS

ANSYS CFX allows for the choice between various turbulence models. Multiple options are available, but only three are recommended for compressor applications [63]. Two models are based on the eddy viscosity hypothesis, the  $k-\varepsilon$  and Shear-Stress-Transport  $k-\omega$  based models. The other model is based on solving the Reynolds-stress transport equations, named the Baseline Reynolds Stress model.

The  $k-\varepsilon$  model is the most widely used turbulence model in CFD. It is an eddy viscosity model, where the turbulent fluctuations are related to the mean velocities through a known turbulent viscosity. It is also known as a “two-equation” model, in which it adds two more transport equations to be solved for the two turbulence quantities: the turbulence kinetic energy,  $k$ , and the turbulence eddy dissipation,  $\varepsilon$ . Of the available turbulence models, this is the easiest to implement. However, the model uses five constants whose values are based on empirical observations and are chosen to give an accurate estimate for a varied range of flows. It tends to be less effective for high-swirl, wall-bounded flows. Therefore, the model is less effective in flows in rotating fluids, curved surfaces, and boundary layer separation. However, it is the fastest and most flexible model to implement, and its rapid solution typically outweighs the inaccuracy associated with it [64,65].

CFX also implements a  $k-\omega$  Shear-Stress-Transport (SST) model. Standard  $k-\omega$  models replace the second equation for the turbulence eddy dissipation,  $\varepsilon$ , with one for the turbulence frequency,  $\omega$ . Again, this equation is based on empirical constants. These models tend to over-predict the eddy-viscosity term in the equations. The SST formulation of the model used by CFX also incorporated blending functions to include stress transport effects and limit the production of turbulence energy. This allows for a better prediction of the onset and amount of flow

separation due to pressure gradients. However, this model usually requires a finer mesh in the near-wall regions in order to produce better results than the  $k-\varepsilon$  model. The computation time required to solve is increased: even though it is still a two-equation model, it requires a number of extra calculations for the blending functions and the finer near-wall grid [63,64].

Two separate applications are available using the Reynolds Stress models. In this case, the turbulent transport equations are solved for the individual Reynolds stresses without the assumption of a turbulent viscosity relationship. Additionally, a length or time scale for the turbulence needs to be computed, either  $\varepsilon$  or  $\omega$ . Therefore, the Reynolds Stress models replace the two-equation models with seven additional equations. Additionally, the pressure-strain correlation must be calculated in an additional step, also adding to the computation time required for a solution. In general, a Reynolds Stress model will take at least twice as long to solve than the  $k-\varepsilon$  model. However, the benefit of the models is that they naturally include the effects of streamline curvature, secondary flows, and Coriolis forces in rotating flows. CFX allows for the use of the Speziale, Sarkar and Gatski (SSG) Reynolds Stress Model, which uses  $\varepsilon$  for the scale equation, and the Baseline (BSL) Reynolds Stress Model, which uses  $\omega$  for the scale equation. The recommendation between the two is for the BSL model, as it produces better results for wall-bounded flows and boundary separation simulations [63,64,65].

In the single-passage steady-state solutions, the standard  $k-\varepsilon$  turbulence model showed a good correlation to the experimental results, so the transient simulation was initially performed using the same model. However, once dealing with transient effects and the boundary layer separation involved in rotating stall, the choice of turbulence model may have an effect on the solution. However, it should be noted that it has less importance to the accuracy of the results than the choice of mesh size and transient time step. A coarse mesh of large time step will easily



produce more simulation error than the turbulence model. If the  $k-\varepsilon$  turbulence model does not produce accurate results once a satisfactory mesh and time step have been developed, further investigation into the turbulence model will be necessary.

### **3.5 PARALLEL PROCESSING**

The increase in solution time between the  $360^\circ$  mesh and the single-passage meshes was significant, as expected. In order to complete the large-scale simulations, parallel processing on a set of HPC servers was necessary. The general intent is to increase the number of processors used to solve the problem, therefore achieving the same solution with a faster turnaround. In order to use multiple processors, the mesh must be divided into partitions. An example for simple 2D mesh run on four processors is shown in Figure 3.5. Each partition is assigned to one of the processors. However, the information at the boundaries and interfaces of the partitions must be communicated between all the processors. This is achieved in ANSYS CFX-Solver [66] by declaring a “master” processor, which is in charge of the communication between the various partitions.

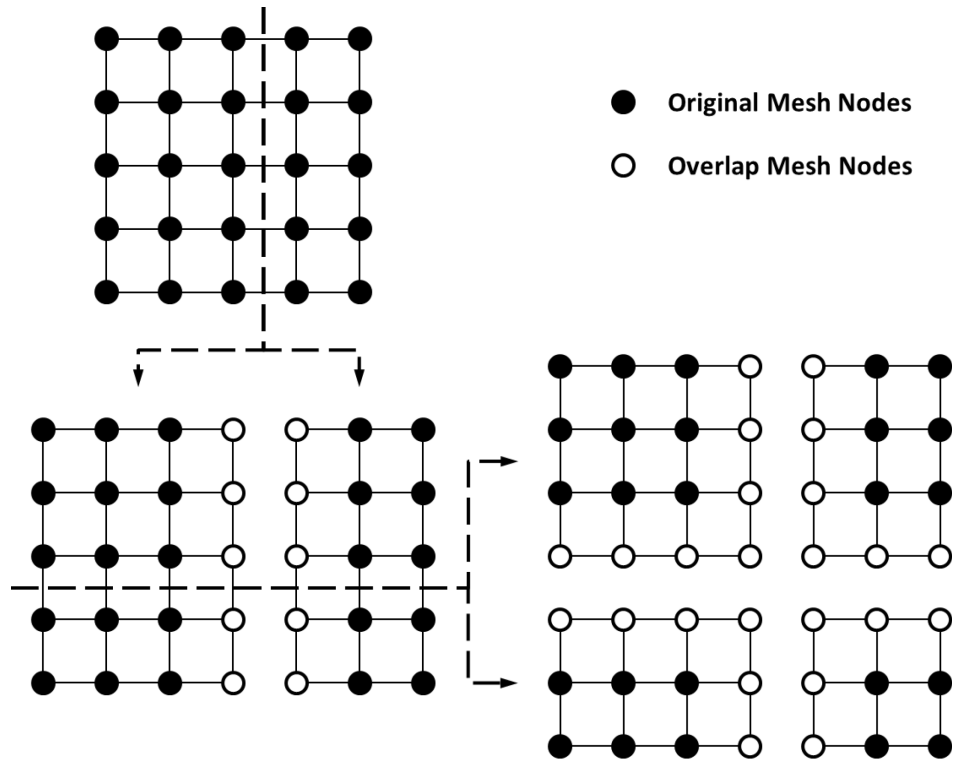


**Figure 3.5. Mesh overlap nodes for partitioning, adapted from ANSYS CFX [66]**

The choice of the number of processors will have an effect on both the solution time but also on simulation accuracy. While it is generally better to increase the number of processors, there reaches a limit at which increasing the number of processors does not produce a significant decrease in simulation time. The suggested limit by ANSYS CFX is 75000 nodes per partition, but may vary according to the machine used [66]. Additionally, at the interfaces between the various partitions of the mesh, there will be overlapping regions of mesh whose properties are solved by both processors on either side of the interface, also shown in Figure 3.5. After every iteration, the values at these overlap nodes are averaged and replaced for the next iteration. This typically causes a small amount of numerical error. However, if the mesh is divided into so many partitions that the overlap zones become a significant amount of the overall volume of the domain, the numerical error caused by the averaging of the interfaces accumulates into a significant error in the solution. The metric used by ANSYS CFX is the overlap percentage,

which calculates the amount of mesh nodes in the overlap regions over the total number of nodes in the entire domain. The recommendation is to keep the overlap under 10% where possible, but it may be pushed as high as 20% [66]. Therefore, there is an upper limit of processors that may be used before the simulation starts to break down.

For the 360° mesh produced for the impeller being investigated, a study was performed to find the number of processors that would allow for an improved computation time without sacrificing numerical accuracy. The simulations were completed for the 360° mesh using the steady-state solver at the design point. However, they were forced to complete exactly 400 steady-state iterations, to better compare the solution times. The only parameter that was varied was the number of parallel processors for each run. The partitioning method used was the Optimized Recursive Bisection Method with a uniform partition size. The transient simulations will use Transient Rotor-Stator interfaces between the stationary and rotating domains of the model, so the partitioner must also use the Coupled, Transient Rotor-Stator options for domain partitioning. The solution times are shown in Table 3.2.

**Table 3.2. Solution time reduction for parallel processing, run for 400 iterations with 4,065,828 nodes**

<b># Processors</b>	<b>Solution Time</b>	<b>Average Iteration Time</b>
1	2d:13h:20m:36s	552.1 s/iter
8	1d:09h:38m:43s	302.8 s/iter
16	18h:53m:08s	170.0 s/iter
32	12h:15m:59s	110.4 s/iter
60	1h:16m:22s	11.5 s/iter

The simulation times are also plotted, along with the overlap percentage calculated, in Figure 3.6. The overlap percentage values were calculated after running the partitioning step for the same mesh between different numbers of processors. The solution times continuously

improved up to 60 processors, and from the graph it seems using more processors might still benefit the computation time; but increasing the number of partitions beyond that would approach the 20% overlap limit. The limit of 75,000 nodes per partition is also reached at 60 parallel processors (74,272), while the average overlap percentage between partitions is 16.7%. Again, the simulations were checked for numerical accuracy, using the same metric as the grid studies, and they all produced results within  $\Psi_M = 0.5\%$  of the baseline results. From these results, it was decided to perform the transient simulations with a maximum of 60 processors.

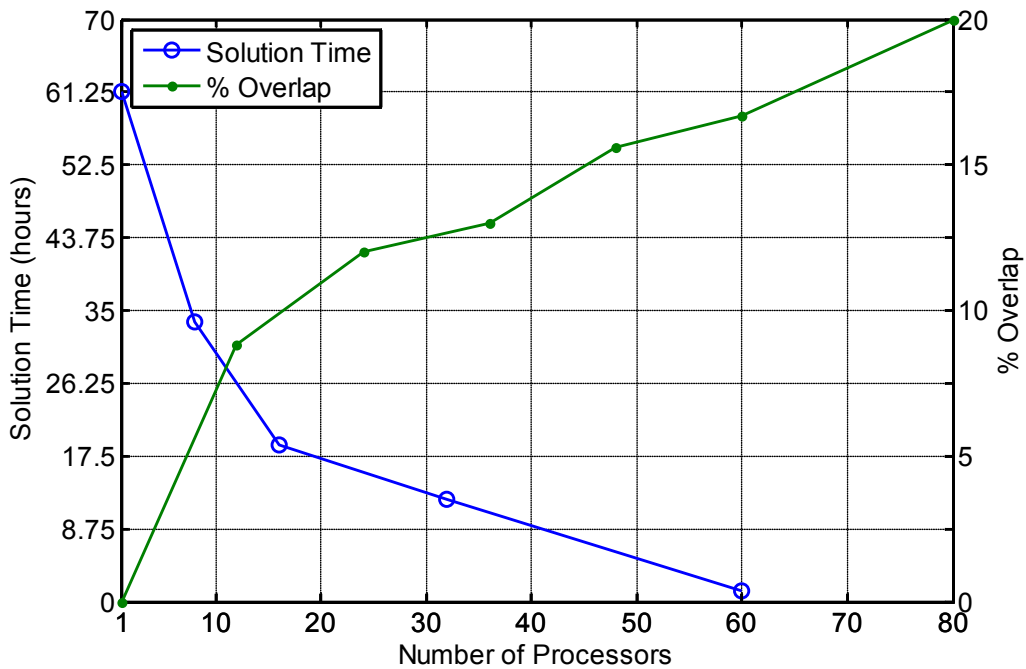


**Figure 3.6. Solution times and overlap percentage variation with number of parallel processors**

### 3.6 FIXED-FLOW TRANSIENT SIMULATIONS

The purpose of the transient simulations is to capture rotating stall at an operating point that has exhibited rotating stall in experimental studies. Comparing the experiments and

computational results will allow for a better understanding of the phenomenon and how it shows up in CFD simulations. In addition to the points where rotating stall was expected, one transient simulation was completed at the design point for the compressor, corresponding to  $N = 19240$  rpm and  $\phi_1 = 0.054$ . This is a stable point and served as a benchmark case for comparison to the other points.

Before starting the transient simulations, steady-state solutions with frozen rotor interfaces were completed on the  $360^\circ$  mesh to be used as initial conditions. The steady-state, single-passage simulations showed that the schemes and boundary conditions chosen for this model were sufficiently accurate. Therefore, the transient simulations were performed with a uniform, axial inlet and with a fixed mass-flow outlet at the diffuser exit,  $d_5$ . The high resolution advection scheme was used, with the standard  $k-\varepsilon$  turbulence model, since the steady-state validation showed a good correlation to experimental values. A moving mesh was used to simulate the impeller rotation at a fixed speed. Transient Rotor-Stator interfaces were used at the two interfaces between the rotor and stationary components.

The transient scheme used was second-order backward Euler. The discretization of the transient time step is a very important factor in the accuracy of the transient simulations. As with the grid size, the time step size will affect both the accuracy and the computation time. Smaller time steps will improve solution accuracy, but a larger number of iterations will be required to complete a single revolution of the impeller. A time step that is too large will not resolve any flow effects that occur on a smaller time scale. Again, a balance needs to be found: the smallest time step that allows for a reasonable solution time. The commonly used metric is the Courant number (CFL), a dimensionless number relating the size of the mesh,  $\Delta x$ , to the size of the time step,  $\Delta t$ , using the fluid velocity,  $v$  [67]. For a 1-D mesh, it is defined as

$$\text{CFL} = \frac{v\Delta t}{\Delta x} \quad (3.4)$$

For transient simulations, the average Courant number over the domain should be on the order of 1~10. As an additional guideline, Anish and Sitaram [68] recommend using a step size sufficiently small to require 30 to 50 time steps for a blade to cover a single blade passage. It should be noted that the recommendation given was developed for investigations of impeller-diffusor interaction, and no such recommendation is available for rotating stall investigations. Therefore, the more conservative option was to use the smallest time step in the recommended range, requiring 50 time steps per passage rotation and 750 time steps per revolution. For the tests run on the  $N = 19240$  rpm line, this leads to a time step size of  $\Delta t = 4.158 \times 10^{-6}$  seconds and corresponds to an average  $\text{CFL} = 2.74$ . For the tests run on the  $N = 20640$  rpm line, this leads to a time step size of  $\Delta t = 3.876 \times 10^{-6}$  seconds and corresponds to an average  $\text{CFL} = 3.04$ .

Each simulation was required to carry out 1500 time steps, or two full revolutions of the impeller. The residual convergence criteria for each time step were reduced to  $1 \times 10^{-5}$ , while the maximum number of iterations allowed per time step was limited to 5. This effectively forced the simulation to completing 5 iterations per time step. Data storage becomes an important limitation in solving the transient simulations. The large size of the  $360^\circ$  mesh causes transient result files to have individual sizes exceeding 3.5 GB. It is beyond typical hard drive limitations to store data for each time step, so transient results were recorded for every 50 time steps. Post-processing of the  $360^\circ$  simulations also poses some computational issues. The amount of data in each individual transient results file is large enough that a personal computer cannot store it in its RAM. The post-processing macros in CFD-Post must be customized to run on a high-performance server as well.

For these simulations, 60 processors were used in parallel. As mentioned in the previous section, this choice approaches the accuracy limits recommended by ANSYS. In order to confirm that the transient results were accurate, the transient simulation was re-run with 30 processors for the equivalent time of one rotor revolution. The results of the two were then compared for discrepancies, and none were found. The mass-averaged thermodynamic and aerodynamic values at all locations varied by less than 0.1% between the 60 processor and 30 processor simulations.

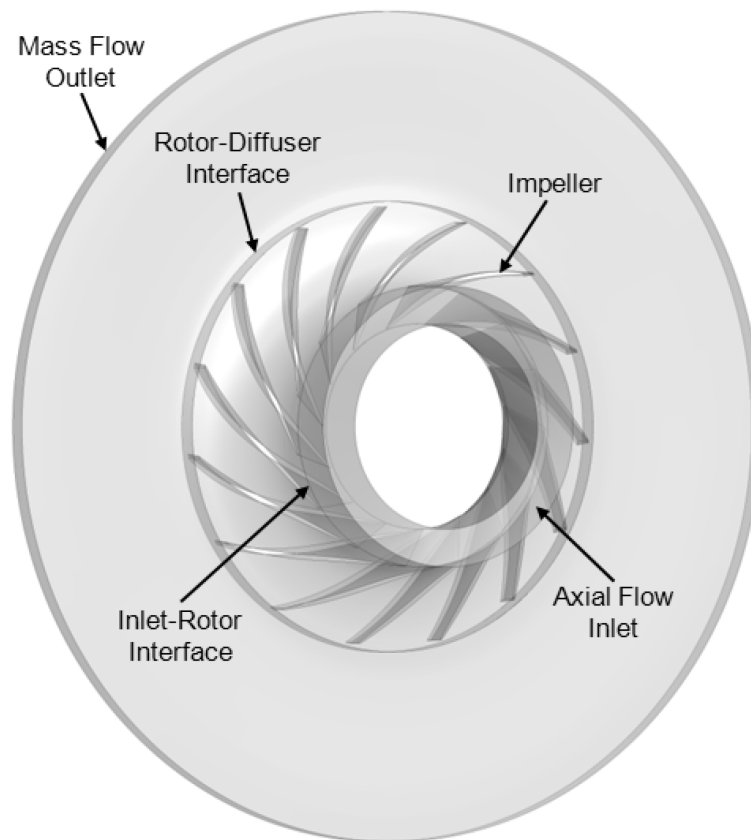


**Figure 3.7. Full 360° computational model used for transient CFD simulations, with axial inlet, impeller, diffuser and interfaces**

During transient simulation runs, the mass flow through each boundary and interface was monitored. With the boundary conditions chosen, the mass flow at the outlet of the diffuser was

fixed. The mass flow at the interfaces between the rotating and stationary regions of the model was also monitored. There are two such regions: the Inlet-Rotor Interface located just before the leading edge of the impeller blades and the Rotor-Diffuser Interface located after a short mixing zone after the trailing edge of the blades. Both of these interfaces are shown in Figure 3.7. During steady-state simulations, the mass flow at these boundaries must converge to the same value as the outlet boundary. However, this is not required during the transient simulations. In general, since the maximum number of iterations allowed per time step was limited to 5, the mass flow rate through these interfaces will fluctuate but only by small values. This is normal for transient CFD simulations due to numerical noise and some of the unsteady aerodynamics phenomena such as recirculation, jet/wake flow and rotor-diffuser interaction through these regions [68,69]. However, the time-averaged mass flow rate through these sections must remain at the same value as the prescribed boundary condition. During the course of these investigations, it was found that the fluctuations of mass flow at these two interfaces are much more pronounced during rotating stall.

### **3.7 SPEED-LINE TRANSIENT SIMULATIONS**

The fixed-flow simulations were mainly used to study rotating stall at a point where it was already known to occur experimentally. Knowing rotating stall occurs is useful, but for compressor design it is more important to be able to predict at which flow rates on the compressor map it presents. The purpose of the speed line simulations was to predict the flow rate where rotating stall first develops: the onset point. This will allow designers to determine if the compressor design needs to be improved to allow for a larger stable operating range.



In the speed-line simulations, the simulation was started at a flow rate that was known to be stable. If experimental data are not available, then the design point could be used. As with the fixed-flow transient simulations, a steady-state simulation must be completed first at that stable flow point to be used as the initial condition. Most of the simulation setup for the speed-line simulations was the same as that for the fixed-flow simulations. The only difference was the mass-flow outlet. With the type of boundary condition chosen, the mass flow at the diffuser exit was fixed. After starting the transient simulation at the stable flow point, the mass flow at this boundary was reduced periodically but always to a fixed value. This is very similar to typical compressor testing, where a valve is used to decrease the flow rate through the compressor from choke to surge.

For these simulations, it was necessary to determine the size of the flow-rate step and how many revolutions to complete at each step. The mass flow rate drop must not be large enough to drastically change the flow conditions in the rotor, while allowing for a reasonable time to complete the simulations. Since experimental results were already available for this impeller, the mass-flow steps chosen equaled one third of the mass-flow steps taken experimentally. On average, this resulted in a 0.002 drop of the inlet flow coefficient. After each flow drop, the compressor must be allowed to settle at the new flow and have enough time for the rotating stall to develop. It was determined, from the fixed-flow simulations, that one full revolution of the impeller (750 time steps) would be a sufficient time for the compressor to develop stall and stabilize before dropping the flow rate again.

Two rotational speeds were tested using the speed-line simulations, at 19240 and 20640 rpm. These lines were chosen from the experimental results for this compressor since they exhibited the most varied range of rotating stall occurrences. The size of the time steps was the same as

that in the fixed-flow simulations. The rotational velocity of the impeller remains constant during the speed-line simulations, so the transient time step does not need to be adjusted when the mass flow rate changes. However, the drops in mass flow cause the flow velocity to change and the Courant number changes during these simulations. In the case of the  $N = 19240$  rpm line, it varies from  $CFL = 3.21$  to  $2.62$ . In the case of the  $N = 20640$  rpm line, it varies from  $CFL = 3.17$  to  $2.63$ .

For the speed-line simulations, FFT analysis was also used to determine frequency content of the mass-flow signals at the domain boundaries. The resulting signals were compared to those from the fixed-flow simulations. Since the speed-line simulations began at a stable flow rate and moved into the rotating stall regime, the signal was split into two portions: the stable region before stall develops and the unstable region during operation with rotating stall, with the split representing the onset point. The FFT analysis was applied to each signal portion individually, and the results compared. As an additional baseline, the same simulation setup was used on a single-passage mesh. In the single-passage simulation, the periodic boundary conditions do not allow asymmetric phenomena such as rotating stall to appear. Therefore, the FFT of this signal was used as a baseline comparison to how the mass fluctuations would appear if rotating stall never developed in the compressor.

Additionally, the FFT analysis was used to determine the onset flow rate of rotating stall. Since the signal must be split at the onset point, but this point is usually not known a priori, it must be determined from the FFT content of the numerical results. From the results, it was determined that the FFT of the stable region should show little to no supersynchronous content, while the rotating stall region should have some high-frequency content. Using this, the onset point could be determined iteratively, starting with an initial guess and performing the FFT

analysis to determine if the two signals match the above criteria. The guess for the onset point is then varied until the lowest mass flow value that shows a stable region without high frequency oscillations is found. This is determined to be the computational rotating stall onset flow point. These results are then compared to the visual interpretation of the actual mass-flow signals and the experimental results for this compressor.

## CHAPTER 4: FIXED-FLOW TRANSIENT SIMULATIONS

### 4.1 ROTATING STALL AT $N = 20640$ RPM

The first set of results presented show the rotating stall captured in the transient simulation run for the point at  $N = 20640$  rpm and  $\phi_1 = 0.04308$ . The transient results at this operating point show the development and propagation of a single rotating stall cell in the compressor impeller. The following sets of plots show the velocity and pressure profiles taken at instantaneous snapshots during the transient simulation. All the profiles shown are taken in a blade-to-blade view at 50% span between hub and shroud.

The development of rotating stall is shown in Figure 4.1, page 60, in which the vectors show the relative velocity between the blades,  $W$ , and the underlying contours are colored by the velocity magnitude. The discontinuity between the inlet and the blades is caused by the sudden change from a stationary frame to a rotating frame in the impeller. The impeller blades are rotating upwards in this view. Figure 4.1(a) is taken shortly after the start of the transient simulation. Figure 4.1(b) and (c) are each taken 50 time steps later and the frame is rotated so the same blades are shown in all three pictures; the blades are numbered for clarity.

Figure 4.1(a) shows the initial disturbance that causes the rotating stall in this impeller. The flow is slightly irregular at the leading edge of blade 1, causing the flow reaching that blade to slow down and turn to avoid the disturbance. In Figure 4.1(b), the deviated flow off the leading edge has reached the tip of blade 2. This causes two issues: the throughflow in the blade passage is decreased and the incidence on the lower blade is increased.

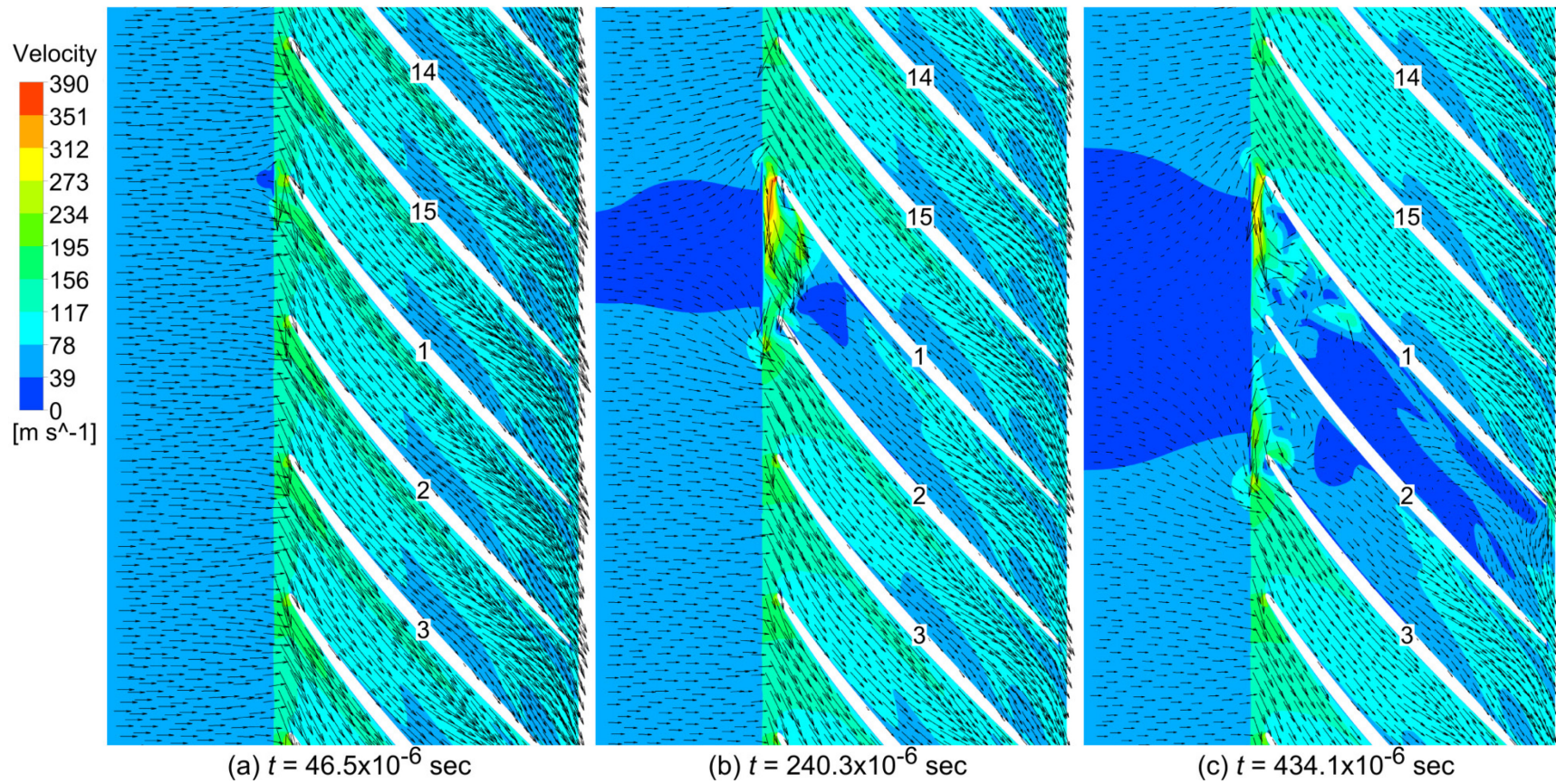


**Figure 4.1. Velocity vectors showing development of rotating stall cell,  $N = 20640$  rpm and  $\phi_1 = 0.04308$**

In Figure 4.1(c), the full rotating stall pattern is seen. The passage between blades 1 and 2 is fully stalled, with most of the flow velocity at zero. However, it has begun to recover, as would be expected. As the stall moves to the passage below it, the flow along the suction side of blade 1 begins to move back in its intended direction. This flow entrails the rest of the stagnant air between the blades, eventually causing the entire passage to return to its original flow pattern. The flow between blades 2 and 3 is in the initial stages of stall. The flow has separated off the suction side of blade 2, near the leading edge. This is due to the increased incidence from the stalled passage above it. While most of this passage is still flowing forward, a reversed flow eddy has formed at the leading edge of the passage, forcing the incoming flow to slow down and some of the flow to recirculate around the leading edge of blade 3. This eventually causes the passage velocity to decrease and resemble the passage above it.

While the flow between blades 4 and 5 is still unaffected by rotating stall, the reversed flow around the tip of blade 4 will force the incidence on it to increase. This will cause the same separation seen in the channel above and eventual stalling of the passage. Therefore, rotating stall will propagate downward in the direction opposite to the impeller rotation. The rotating stall propagation matches the direction in which the reversed flow eddy moves over the blade tip, as was also shown in the flow patterns measured by Krause et al. [28] and Lennemann and Howard [27], previously shown in Figure 1.5. This reversed flow eddy is the driving factor in the propagation of rotating stall, causing the increase in incidence that forces the stall cell to move from one passage to the next. Without this flow reversal around the blade leading edge, the stall would not be able to affect the flow in the next passage and, therefore, would not propagate. Also of significance is the region of retarded flow in the inlet domain, which was expected from the stall phenomenon, as shown previously in Figure 1.4. Additionally, Figure 4.2 plots the

meridional velocity contours in the impeller eye, taken just before the leading edge of the blade. The stall cell is seen clearly in this plot, but it also shows the areas of reversed flow (dark blue) that are caused by the passage stalling.

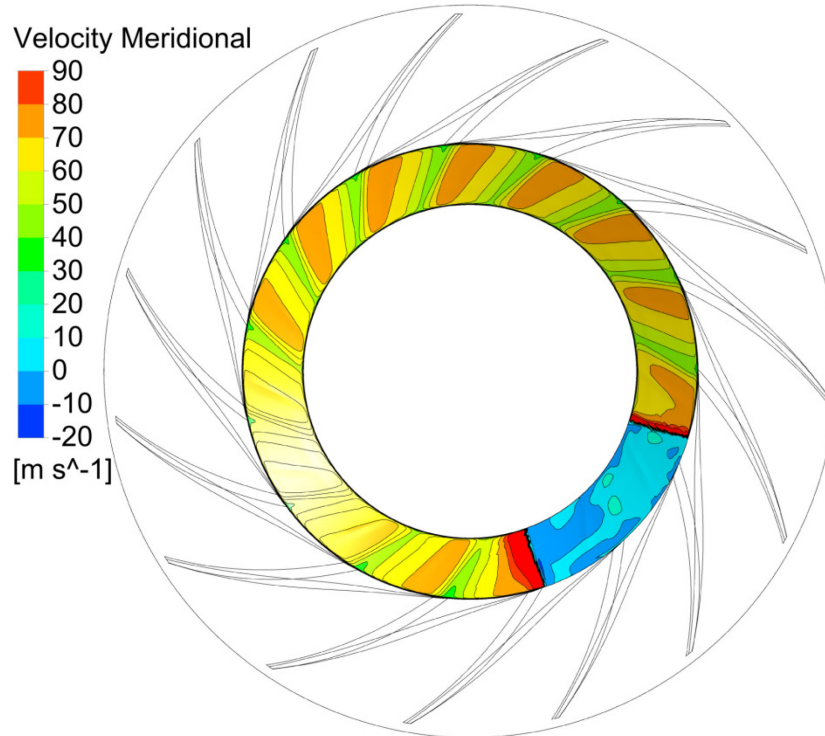


**Figure 4.2. Meridional velocity near blade leading edge during rotating stall,  $N = 20640$  rpm and  $\phi_1 = 0.04308$ , at simulation time  $t = 434.1 \times 10^{-6}$  sec**

The propagation of the rotating stall around the impeller is best seen in the pressure contours shown in Figure 4.3(a)-(e), shown on page 63. The contours show the development and propagation of the rotating stall cell. The figures are zoomed into the stall area of the rotor, but the blades in the figures are numbered from 1-15, as a reference for the rotation of the impeller. The results show how quickly the stall cell develops in the rotor. In only a fraction of a revolution of the impeller, the stall cell grows from a small incidence loss to a fully-developed stall cell. Once the cell is developed, it covers two to three flow passages and propagates in the direction opposite to the impeller rotation.



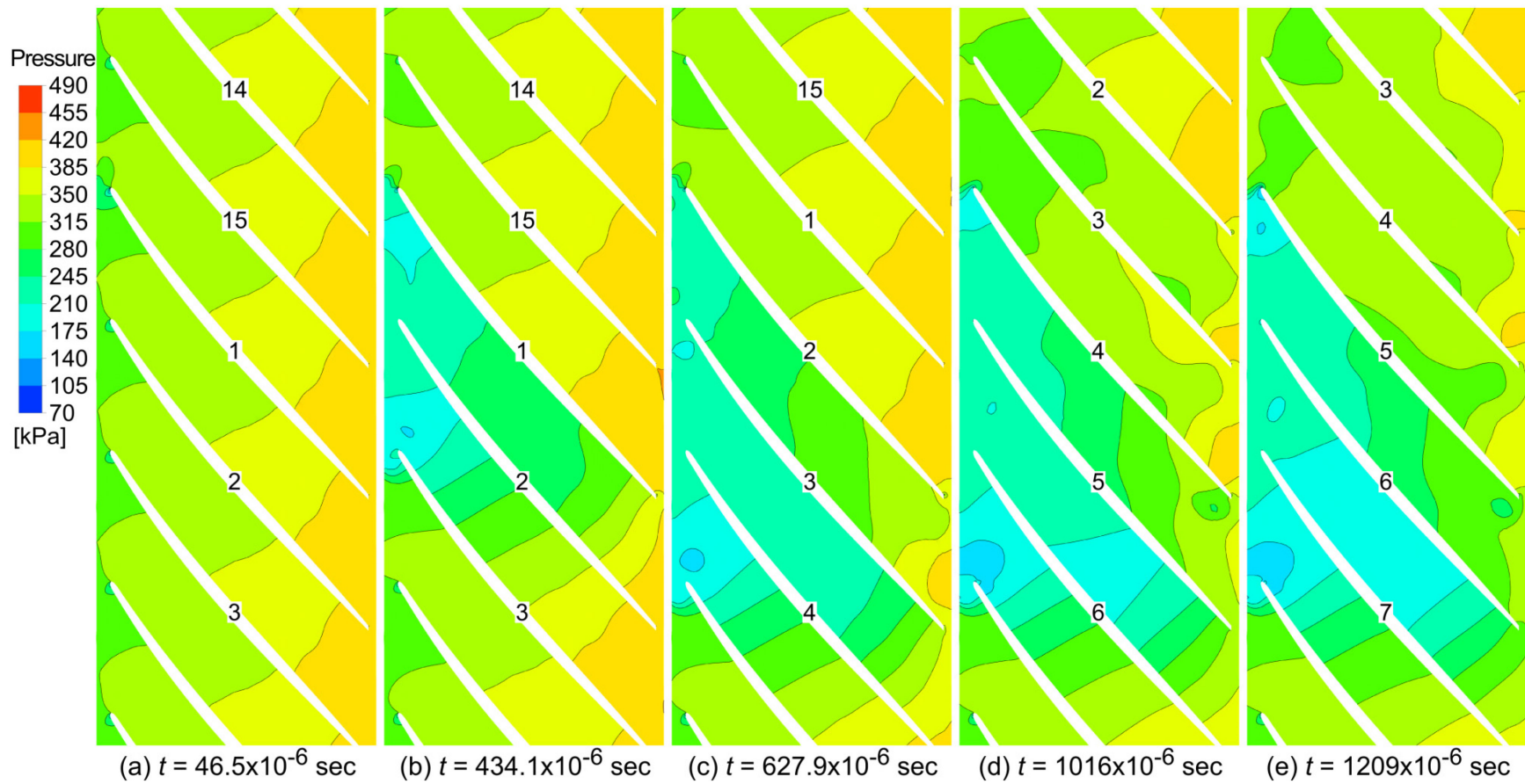


**Figure 4.3. Pressure contours showing development of rotating stall low-pressure zone,  $N = 20640$  rpm and  $\phi_1 = 0.04308$**



Since the size of the rotating stall cell varies with time, it is difficult to exactly determine the rotating speed of the phenomenon. As the stall is developing initially, in Figure 4.3(a) and (b), it does not move between blade passages. On average, the rotating speed can be estimated at 87% of the rotor speed since it moves across 13 blade passages after one full revolution of the impeller (15 blades). This estimated value is consistent with what Frigne and Van den Braembussche [8] found for progressive impeller rotating stall, which is caused by incidence and flow separation in the impeller.

The CFD results for the transient simulations at the  $N = 20640$  rpm and  $\phi_1 = 0.04308$  operating point clearly show the development of a single rotating stall cell, rotating against the impeller direction. This does not match with the experimental results at this point, which showed two cells rotating with the impeller. The development of multiple cells will be affected by two important factors that have been ignored in the computational simulations: inlet distortions and aerodynamic loading from the return channel. The CFD simulations were completed with a uniform axial inlet, while the testing was performed with a set of inlet guide vanes that do not produce a completely uniform velocity profile. The testing results also proved that the return channel geometry will have an effect on the location and number of cells of the stall. Due to time and computer limitations, the return channel was not modeled in the transient simulations. However, the simulations proved to be a useful tool for detecting the occurrence of rotating stall in the compressor.

## **4.2 ANALYSIS OF MASS FLOW FLUCTUATIONS**

The previous section presents the CFD results for a fixed-flow simulation performed at  $N = 20640$  rpm and  $\phi_1 = 0.04308$ . In the results, a single stall cell is seen to be rotating against the

impeller direction. During the transient runs, the mass flow at the interfaces of the rotating and stationary domains was monitored. Figure 4.4 shows the time-series mass flow rates during rotating stall operation. The mass flow rate is plotted for the Inlet-Rotor Interface and the Rotor-Diffuser Interface. The time-averaged mass flow rate of both signals and the mass flow applied at the outlet boundary condition,  $\dot{m} = 1.574$  kg/s, are also plotted. The time averaged value is within 0.5% of the boundary condition, which is within the mass-flow conservation target set for the simulation. The flow rates at the inlet and outlet interfaces of the rotor are allowed to fluctuate, but the trends for both lines are the same. The rotor is still operating at an overall steady state, as seen from the time averaged value; but rotating stall is causing flow reversal and therefore transient mass-flow fluctuations near the impeller. Some of the fluctuation is due to normal numerical error in the simulations, so the two signals contain frequencies caused by both numerical error and rotating stall.

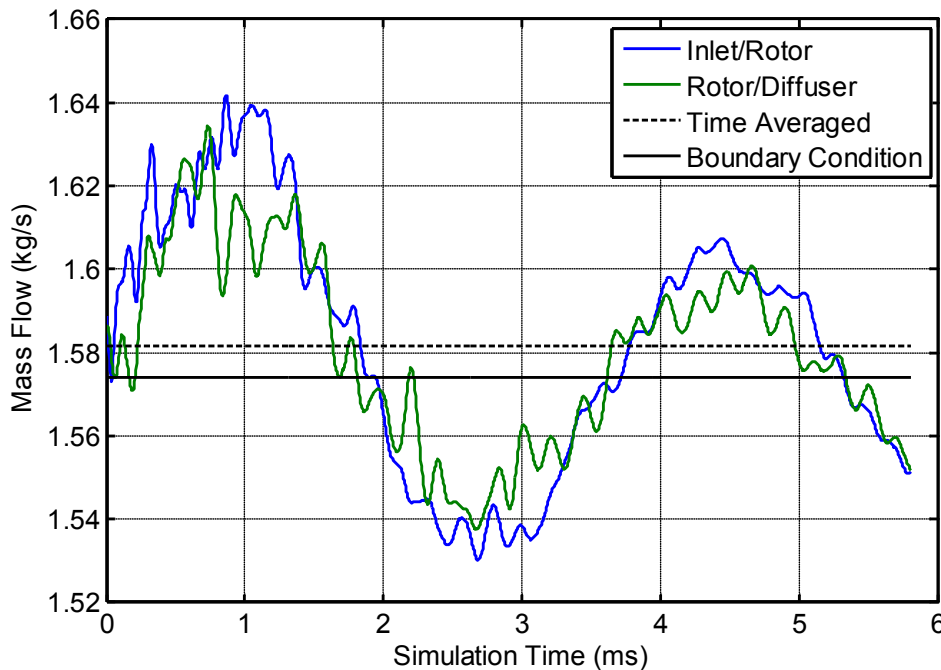


**Figure 4.4. Time-record of mass flow rates for transient simulation at  $N = 20640$  rpm and  $\phi_1 = 0.04308$**

FFT analysis was applied to the two mass-flow signals at the interfaces in order to determine the exact frequency content of the two signals. The results are shown in Figure 4.5. To remove the DC portion of the signal the values are normalized before the FFT is applied using the equation:

$$\dot{m}' = \frac{\dot{m}_{\text{int}} - \dot{m}_{\text{bc}}}{\dot{m}_{\text{bc}}} \quad (4.1)$$

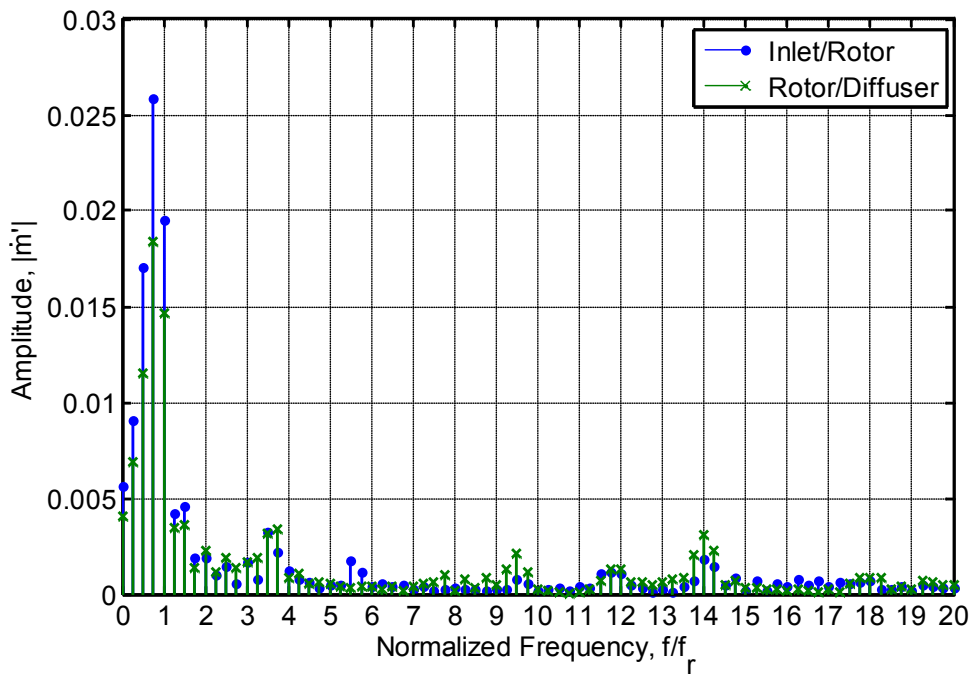


**Figure 4.5. Frequency spectrum of mass-flow signals at rotor interfaces,  $N = 20640$  rpm and  $\varphi_1 = 0.04308$**

The frequency was normalized by the rotational frequency of the rotor, so that is a multiple of the rotation frequency,  $f_r$ . Therefore, frequencies below 1 are subsynchronous and above 1 are supersynchronous. The major peak in Figure 4.5 occurs at  $f/f_r = 0.75$ , or at 75% of the running speed. This is a significant development, as it matches the predicted rotational speed of the rotating stall in this simulation. Furthermore, by zero-padding the signal, the frequency of the peak can be found with more precision to be at 78% of running speed. This leads to the

conclusion that the frequency peak exists due to the presence of rotating stall in the simulation, and that the frequency of this peak matches the rotational frequency of the stall. This value falls within the observations of Frigne and Van den Braembussche [8] and matches well with the prediction of  $\omega_{rs}/\Omega = 87\%$  from the previous section. Figure 4.5 shows a few more significant peaks at  $3.5f_r$  and at  $14f_r$ . Additionally, there is no significant peak at  $f/f_r = 1$ . This indicates that the rotational frequency of the rotor itself does not affect the mass flow fluctuations at the rotor interfaces.

However, in order to determine whether these frequencies can be associated with rotating stall, it is necessary to compare the frequency content of the rotating stall signal to a baseline signal acquired at a stable operating point. The point chosen to represent stable operation was the design point for the compressor,  $N = 19240$  rpm and  $\phi_1 = 0.054$ . In order to compare the transient mass-flow signals from both simulations, the values were normalized by using the mass-flow imbalance across the rotor, using Equation (4.2). The results are plotted in Figure 4.6.

$$\dot{m}'_{imb} = \left| \frac{\dot{m}_{inlet\backslash rotor} - \dot{m}_{rotor\backslash diffuser}}{\dot{m}_{bc}} \right| \quad (4.2)$$

The frequency plot in Figure 4.6 shows that the numerical simulations do have some inherent noise at all frequencies. Across the spectrum, the stable operating point shows small but consistent amplitude. The only standout peak is at approximately  $3.75f_r$ , which was also found to have a peak in the rotating stall simulations. In the rotating stall signal, the peak at  $0.75f_r$  is still present in the FFT of the mass imbalance, and it also contains some high frequency peaks that the stable operating point does not. This is further proof that the peak at 75% of the running speed can be associated with rotating stall operation. The peak at 375% speed seems to be present in both steady and stalled operation, but its magnitude is increased. This is likely caused

by numerical noise, but it is being amplified by the unsteady operation of the impeller. Finally, the rotating stall seems to cause some high frequency oscillations at  $9.5f_r$ ,  $11.75f_r$  and  $14f_r$  that are not present during normal operation. The comparison of the stable and rotating stall fixed-flow simulations verify that the majority of the frequency content in the mass-flow traces can be attributed to rotating stall.

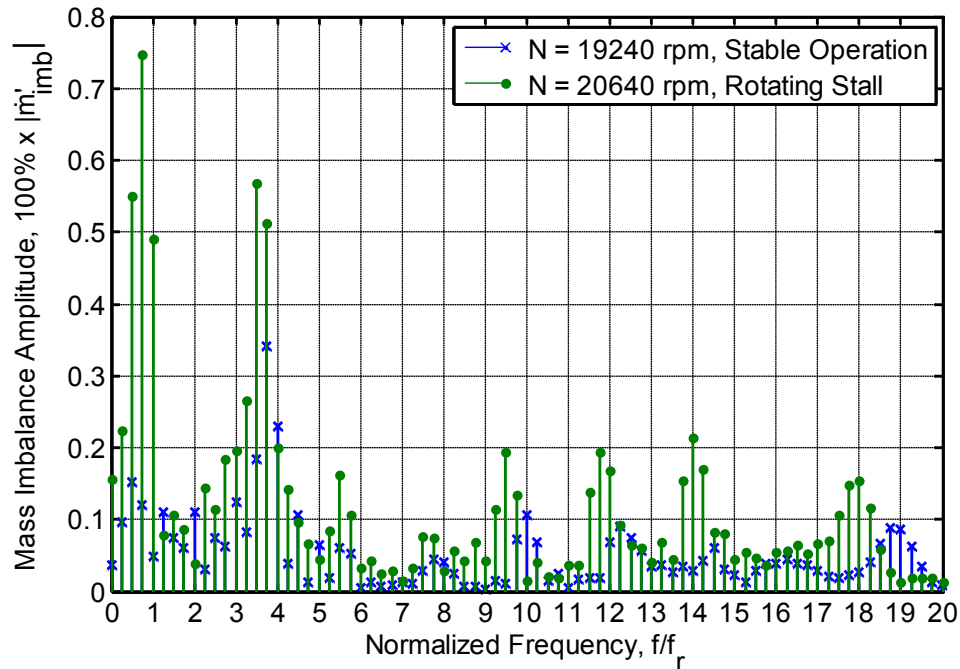


**Figure 4.6. Frequency spectrum of the normalized mass-flow imbalance, comparing rotating stall at  $N = 20640$  rpm and  $\phi_1 = 0.04308$  with normal operation at  $N = 19240$  rpm and  $\phi_1 = 0.054$**

### 4.3 COMPRESSOR SURGE AT $N = 21860$ RPM

The following set of results are taken at the point  $N = 21860$  rpm and  $\phi_1 = 0.04985$ . The transient results at this operating point initially show a flow pattern similar to rotating stall developing in the impeller channels. The flow again separates from the leading edge of the impeller, but the impeller passage never recovers as the impeller rotates past the stall zone.

Instead, the stall bubble propagates to the channels below it, in the direction opposite the impeller's direction. The flow in previously stalled channels does not recover, and eventually stalls throughout the entire impeller.

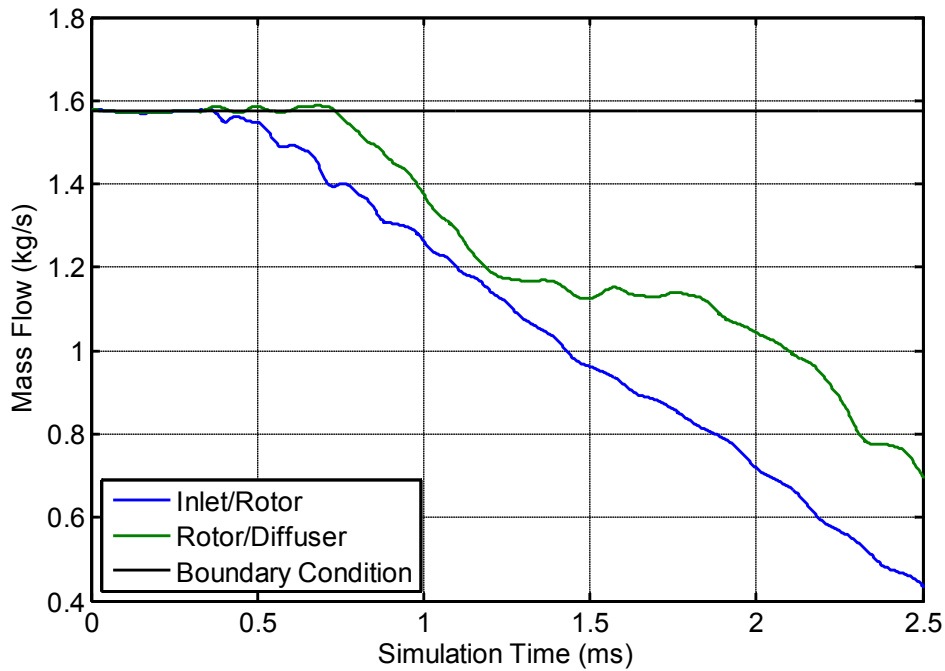


**Figure 4.7. Time-record of mass flow rates for transient simulation at  $N = 21840$  rpm and  $\varphi_1 = 0.04985$**

The mass flow results, shown above, also confirm this trend. While the mass flow oscillates about the boundary condition value at the beginning of the simulation, as if rotating stall is developing, it then starts dropping significantly as the rotor channels stall. The simulation stops running once the flow is reversed throughout all the impeller channels. This behavior is more indicative of surge, and does not match the experimental results, where the surge point recorded for this speed line is at  $\varphi_1 = 0.0423$ .

## 4.4 CONCLUSIONS

Unsteady numerical simulations have been completed on a full 360° model centrifugal compressor during rotating stall operation, with the objective of capturing the formation of the stall cell in the impeller. Flow instabilities appear in the simulations at operating points that have demonstrated stall experimentally. The results prove that the code can simulate the initial disturbance in the impeller and its growth into a fully-developed stall cell. The results show that the stall formation in this case is due to excessive incidence at low flow rates. Additionally, the numerical results match well with rotating stall theory. The flow patterns during rotating stall operation demonstrate how the backflow in the inducer causes the stall cell to affect more than one passage at a time, which allows the stall to propagate in the same direction in which the flow reverses around the leading edge of the blades. The propagation speed of the stall is estimated at 87% of the rotor speed, which also matches well with observed data on impeller rotating stall. Although the characterization of the stall does not exactly match experimental recordings, various factors are mentioned that could be affecting the development of stall cells in the CFD simulations. This is also the first reported case of numerical simulation on full-span stall inside a centrifugal compressor impeller.

The fixed-flow simulations provide confidence in the modeling and simulation methods developed to detect rotating stall. The simulations also showed a relatively simple method of detecting rotating stall during the transient simulations. The development of rotating stall in the impeller caused supersynchronous fluctuations in the mass-flow traces at the Inlet/Rotor and Rotor/Diffuser interfaces of the simulation domain. During stable operation, these high-frequency oscillations were not present. Since there currently is no precise method to predict the

formation of rotating stall before experiments, this development may be used to detect rotating stall in CFD during the design phase.

In the fixed-flow simulations, the transient simulations are initialized and run at a flow rate where rotating stall is expected from experimental results. However, in compressor design it is of interest to determine the range of flow rates at which the operation is affected by rotating stall. In the following section, the boundary conditions during the transient simulation are varied by starting at a stable flow rate and slowly decreasing the mass flow rate until the results show signs of stall. The mass flow fluctuations are used as an indicator for the presence of rotating stall in the numerical simulations, allowing for the prediction of the actual onset flow rate of phenomenon.



## CHAPTER 5: SPEED-LINE TRANSIENT SIMULATIONS

### 5.1 20640 RPM SPEED LINE

The main purpose of the speed-line simulations is to determine the onset flow rate of rotating stall in the compressor. Having seen in the fixed-flow simulations that the occurrence of rotating stall is accompanied by high-frequency fluctuations in the mass flow rate, it was possible to detect these same fluctuations during the speed-line simulations and pinpoint the exact flow rate at which rotating stall first presents during the simulation. The first set of results presented are for the  $N = 20640$  rpm speed line. The experimental results from this speed line showed that rotating stall first occurred when the flow rate dropped from  $\dot{m} = 2.141$  kg/s to  $\dot{m} = 1.955$  kg/s. The speed-line simulation was started with a steady-state run at  $\dot{m} = 2.345$  kg/s, which was well within the stable in the experimental results. The mass flow was reduced once per revolution using steps of approximately  $\Delta\dot{m} = 0.068$  kg/s.

During the speed-line transient run, the mass flow at the interfaces of the rotating and stationary domains was monitored. Figure 5.1 shows the results for the whole speed line. The mass flow at the boundary condition, the solid black line, is plotted to show the step-by-step reduction in mass flow rate applied to the simulation. The time on the x-axis represents the physical time elapsed in the transient simulation, where the steady-state results used as the initial condition for the transient simulations are at  $t = 0$  ms. Once every revolution, which corresponds to every 2.906 ms for this speed line, the mass-flow boundary condition is dropped by approximately 3%. The figure shows the transient results from the initial stable point through the rotating stall region that was determined experimentally. As was expected, the mass flow at the interfaces is seen to fluctuate around the value at the outlet boundary condition. As the boundary

flow is dropped, the interface flows track with it while the magnitude of the oscillations increases. Once the simulation reaches a mass flow rate at which rotating stall is present, the frequency of these oscillations is increased significantly.

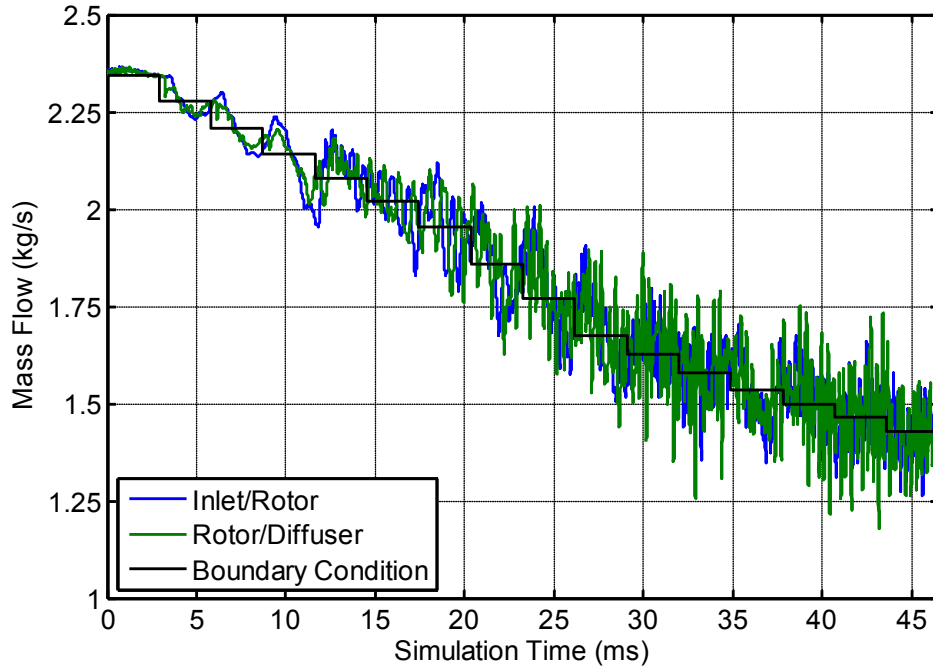


**Figure 5.1. Time-record of mass flow rates for full 360° speed-line simulation at  $N = 20640$  rpm**

Figure 5.2 shows a close-up of the same figure for the area where rotating stall first develops. In this view, the onset of the high-frequency fluctuations is seen to coincide with the drop in mass flow from 2.141 kg/s to 2.077 kg/s. The low frequency oscillations before this point can be attributed in part to the forced drop in mass flow and the transient settling associated with it and also to transient rotor-diffuser interaction [68], which can produce both periodic and aperiodic fluctuations in the impeller velocity profiles. However, it is clear that rotating stall does not occur before this point. The stall onset determined in the physical tests is also shown on the plot. It should be noted that in the experiments the flow rate was dropped directly from 2.141 kg/s to 1.955 kg/s, where the experimental stall onset is marked. However, there is no test data

for the intermediate flow points. During testing, rotating stall generally appears as the flow control valve is moving, and it is not possible to tell the exact flow rate at which the stall was first detected. In comparing the CFD results, the difference in flow step size between the numerical and experimental setups provides different onset values. In both cases, the flow at 2.141 kg/s is stable, but any flow below is unstable. If the flow rate after the step reduction is used as the onset flow, the numerical onset is taken to be 2.077 kg/s and the experimental onset is 1.955 kg/s. Using these same values to calculate the rotating stall margin, as defined in Equation (5.1), yields a difference of 5.69% between the experiments and CFD.

$$\text{RSM} = \frac{\dot{m}_{BEP} - \dot{m}_{RS}}{\dot{m}_{BEP}} \quad (5.1)$$

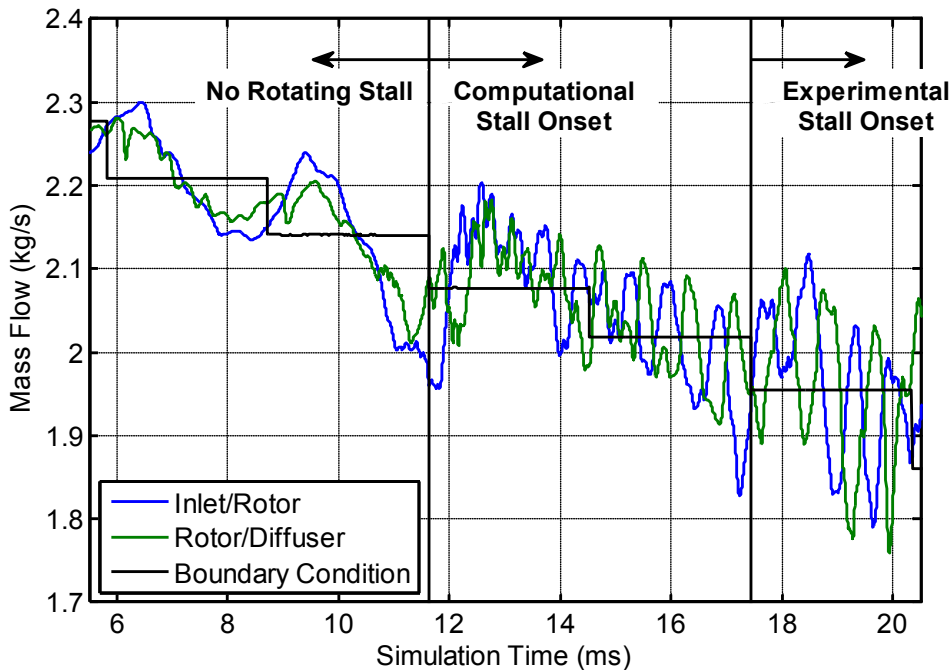


**Figure 5.2. Close-up view of the mass flow rates for  $N = 20640$  rpm line, showing the onset of rotating stall in CFD and experiments**

The fixed-flow simulations in the previous section determined that the high-frequency oscillations could be attributed to rotating stall. In order to confirm this in the speed-line

simulations, it is necessary to have a baseline with which to compare to that does not have rotating stall. For this purpose, the same simulation was completed for the  $N = 20640$  rpm line using a single-passage model. The periodic boundary conditions in a single-passage model assume the flow through all the impeller blade passages to be exactly the same. Due to the unsteady, non-axisymmetric nature of rotating stall, it is not possible for it to appear in a single-passage model. Therefore, the results for a single-passage speed-line simulation provide a good baseline without rotating stall. The mass-flow traces for this simulation are shown in Figure 5.3. For each reduction in flow, the transient results have to settle to the new mass flow value. While the results show that one revolution is just barely sufficient for the transient traces to settle about the desired flow rate, increasing the number of revolutions per step did not provide much benefit while greatly increasing the simulation time.

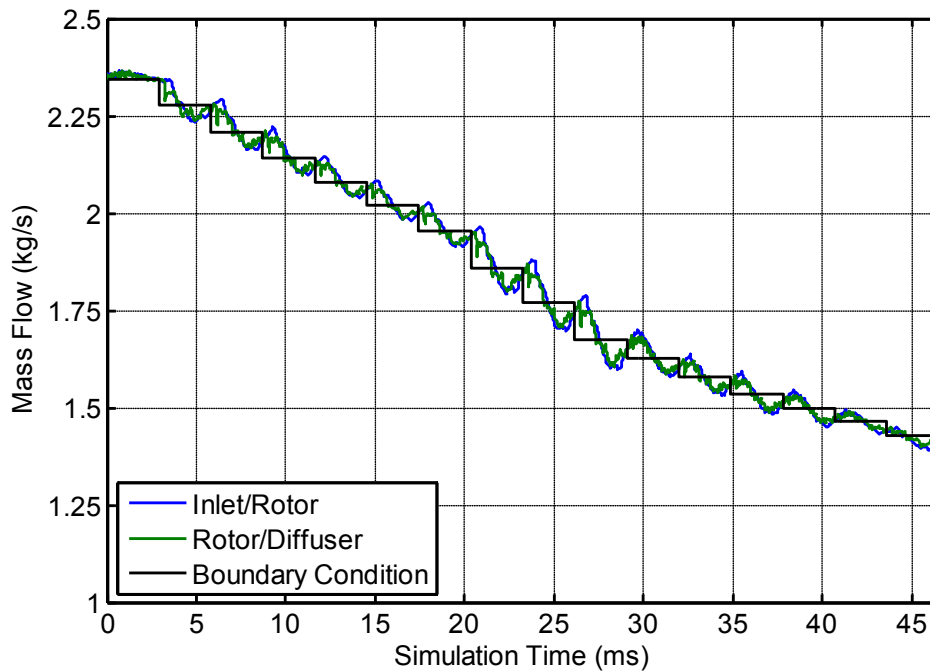


**Figure 5.3. Time-record of mass flow rates for single-passage speed-line simulation at  $N = 20640$  rpm**

For the speed-line simulations, FFT analysis was used to compare the frequency content of the 360° simulation results during rotating stall and during stable operation. The mass-flow signal was divided into two portions: a stable operation region and a rotating stall operation region. If the onset point was chosen correctly, the signal portion during rotating stall should include high-frequency fluctuations of significant amplitude, while the stable operation signal should not. The onset point was determined iteratively using the FFT analysis to meet these criteria. The onset point found using this method was 2.077 kg/s, which matches with the computational onset point which can be seen in Figure 5.2. The mass flow at the interfaces was normalized into a percent mass imbalance using Equation (4.2). The resulting FFT spectra for the stable and unstable portions of the signal are shown in Figure 5.4. Additionally, the single-passage FFT results are included as a baseline.

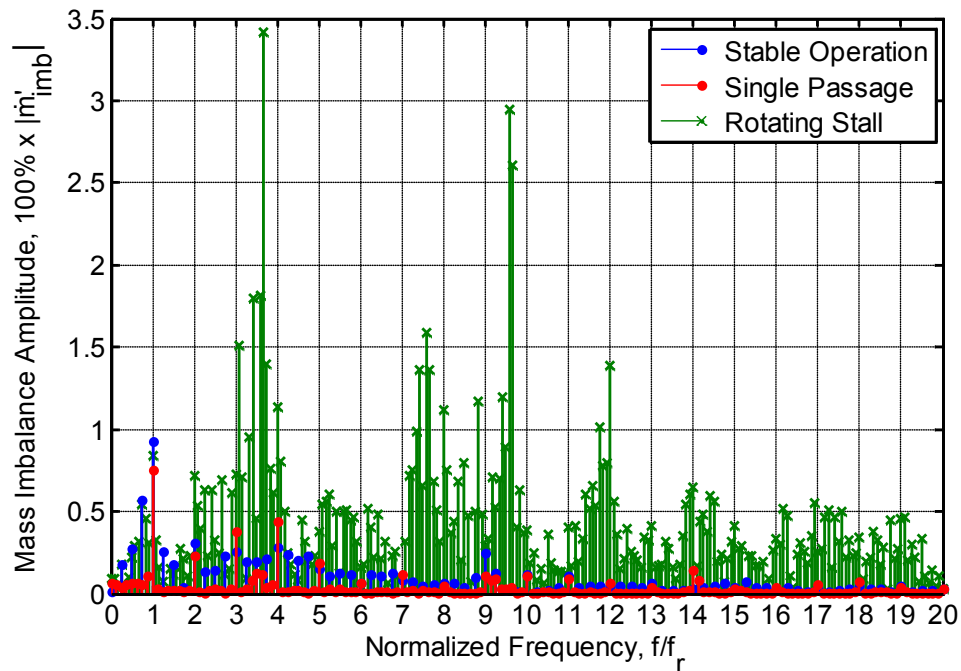


**Figure 5.4. Frequency spectrum of normalized mass imbalance, split between regions of stable and rotating stall operation for  $N = 20640$  rpm line, for an onset point determined at 2.077 kg/s**

The comparison of the three signals shows that they all have a significant peak at the running speed. This is due to the fact that the mass flow rate at the outlet boundary is reduced once per revolution. The peak at  $ff_T = 1$  is the response to the forcing frequency, caused by the periodic drop in mass flow. Since all the steps are similar in size, the magnitude of all three peaks is similar. The single-passage signal contains some high-frequency harmonics but no other significant peaks. Similarly, the stable operation segment of the split signal shows little to no high-frequency content, and matches well with the single-passage results. The rotating stall segment of the split signal shows high frequency content that is very clearly introduced after the rotating stall onset point. The two largest peaks are found at  $3.7f_T$  and  $9.6f_T$ , with two smaller peaks at  $7.6f_T$  and  $12f_T$ . This correlates well with the results also observed for the fixed-flow simulations.

Apart from the frequency analysis of the mass flow, the occurrence of rotating stall is also confirmed in the transient CFD results. Different characterizations of impeller stall were seen, varying in the number of cells throughout the speed line. Figure 5.5, on page 78, shows some of the rotating stall results seen for the 20640 rpm speed-line simulation. The figure shows contour plots of velocity with vectors at 50% span of the impeller. Each of the contours is taken at a different flow point during the simulation; the boundary mass flow for each time step is labeled beneath it. The contours were taken one full revolution after the mass flow rate was dropped to the labeled value; exactly one time step before the labeled mass flow was again dropped to a lower flow rate. The figure shows results from four different transient time steps.



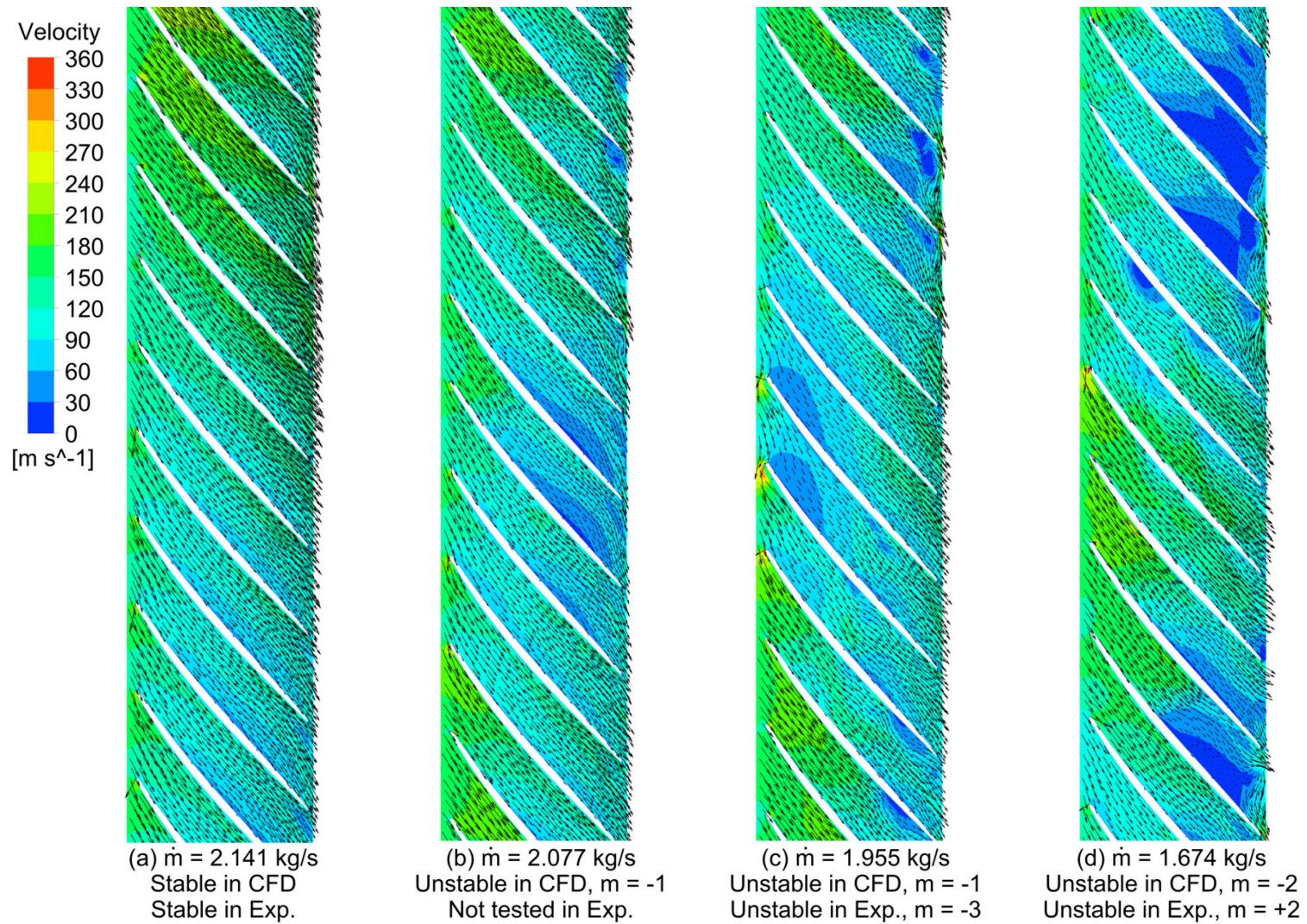


**Figure 5.5. Velocity contours showing rotating stall at various flow rates on the  $N = 20640$  rpm speed-line simulation. For each contour, the type of rotating stall found in CFD and experimentally is labeled for comparison.**

The first velocity results shown, Figure 5.5(a), are taken at a mass flow rate of 2.141 kg/s. This is before rotating stall was noticed in either the FFT analysis or the experimental testing. The velocity contours confirm that there is no rotating stall at this point. However, they also show that there are some asymmetrical disturbances in the flow. The lower part of the figure shows some separation occurring off the pressure side of the blade, approximately half way down the blade length, which is not present at the top of the same blade set. This small velocity fluctuation is similar to the prestall waves sometimes detected in axial compressors [70]. This disturbance is not large enough to create any reversed flow but also indicates the probable cause of the rotating stall. The separation along the blades, produced by the high blade loading for this design, seems to be the main contributing factor to the development of rotating stall in this simulation.

Figure 5.5(b) shows the transient result for a mass flow rate of 2.077 kg/s. This is a flow point that was not tested experimentally and is one of the intermediate steps taken during the numerical simulation. It is taken at the mass flow at which the high frequency fluctuations were seen in the FFT analysis and marks the onset flow rate determined for the numerical simulations. In this contour plot, a single rotating stall cell is seen rotating against the direction of the impeller, taking up three impeller passages. While the flow in the stall cell has not yet reversed direction, the disturbance is large enough to decrease the amount of air passing through the stalled passages. The stall cell is located at the same distance down the blade as the separation seen in Figure 5.5(a), confirming that the stall at this flow point is due to excessive blade loading. Additionally, some low-speed zones are seen along the trailing edge of the blades in the top of the contour. These are not rotating stall cells but eventually lead to the development of a second cell in the rotor at lower flow rates.



The third velocity contour, Figure 5.5(c), shows the velocity results at 1.955 kg/s. This is the first mass flow rate at which rotating stall was noticed during experimental tests. In the simulation, this point is after the onset of rotating stall and therefore should still show a stall pattern. However, the stall pattern exhibited by the compressor will change as the mass flow rate is varied. In this case, a single stall cell is still present, but it has moved from the trailing edge of the blades to the leading edge. As the stall cell reduced the amount of flow through the affected blade passages, the incidence angle is increased. In turn, this causes the separation producing the stall pattern to move further up the blade passage. The disturbances seen at the trailing edge on the top of Figure 5.5(b) are still present but are larger at this flow point. The largest of these disturbances is now causing reversed flow at the exit of the blade passage and therefore could be characterized as the initial stages of a second stall cell.

Finally, Figure 5.5(d) shows the transient results for a flow rate well within the rotating stall regime in both experiments and numerical simulations, at 1.674 kg/s. In this case, two stall cells are seen still propagating against the direction of the impeller. The two stall cells are similar but not quite the same size. The lower stall cell is smaller, taking up only one or two passages rather than three. However, the flow pattern between the blades and the location at which separation occurs is the same. In both cases, reversed flow is present near the trailing edge of the pressure side of the blade. Additionally, the separation for both occurs halfway down the blade length, as in Figure 5.5(b). The effects of the stall cells on the rest of the flow are evident as well. The reduced flow between the stalled passages has increased the velocity through the passages that are not stalled. In experiments the rotating stall at this flow point was also found to be composed of two cells but rotating with the impeller, which is in the opposite direction as detected in the simulations.

In terms of determining the onset point of rotating stall, the numerical results are in agreement with the experimental results. However, it is clear from Figure 5.5 that the stall pattern detected can be very different between the two. There are three factors that will have an effect on the stall characterization that were ignored in order to keep simulation times feasible for this simulation. First, the return channel was not modeled in the simulations in an effort to reduce the mesh size. The experimental results for this compressor showed that the aerodynamic loading imposed by the return channel has a large effect on the type of stall that forms in the compressor, but not on the onset flow rate of the phenomenon. By not including the return channel, the stall being formed in simulations will not necessarily match the stall formed in the experiments. The second issue is the choice to make the inlet boundary condition have a uniform velocity. In experiments a set of inlet guide vanes are used in an attempt to make the flow as uniform as possible, but the exact flow profile is not known. The small non-uniformities in the flow coming out of the inlet guide vanes may cause more rotating stall cells to appear than the uniform flow through the inlet of the numerical domain. Finally, the choice of turbulence model will affect the type of stall detected. Due to the very large size of the mesh, the  $k-\varepsilon$  model was chosen to reduce simulation time. Different turbulence models will provide more accurate predictions for the location and size of the separation off the impeller blades but will also require finer meshes and increased simulation time. However, the important result is that both simulations and experiments show rotating stall at the same flow points, even if the characterization is different. Since the compressor will not be allowed to run in the unstable operation region, using CFD to determine the stable operating range of a compressor is of higher importance than determining the exact type of stall pattern exhibited during unstable operation.

## 5.2 19240 RPM SPEED LINE

The frequency analysis was also performed on the results for the  $N = 19240$  rpm speed line. The experimental results from this speed line showed that rotating stall first occurred when the flow rate dropped from  $\dot{m} = 1.978$  kg/s to  $\dot{m} = 1.751$  kg/s. The speed-line simulation was started at the stable point at  $\dot{m} = 2.168$  kg/s, and the mass flow was reduced using steps of approximately  $\Delta\dot{m} = 0.068$  kg/s. Figure 5.6 shows the mass flow at the outlet boundary and the two interfaces near the region where rotating stall first develops. The trends are similar to those of the 20640 rpm line, with the onset of rotating stall being closely associated with the emergence of high-frequency fluctuations at the two rotor-stator interfaces. However, the onset flow rate is somewhat harder to determine visually from this plot. While the 20640 rpm results showed a marked difference between stalled and stable operation, the onset of stall seems to be more gradual for this speed line, occurring either at 1.751 kg/s or at 1.687 kg/s.

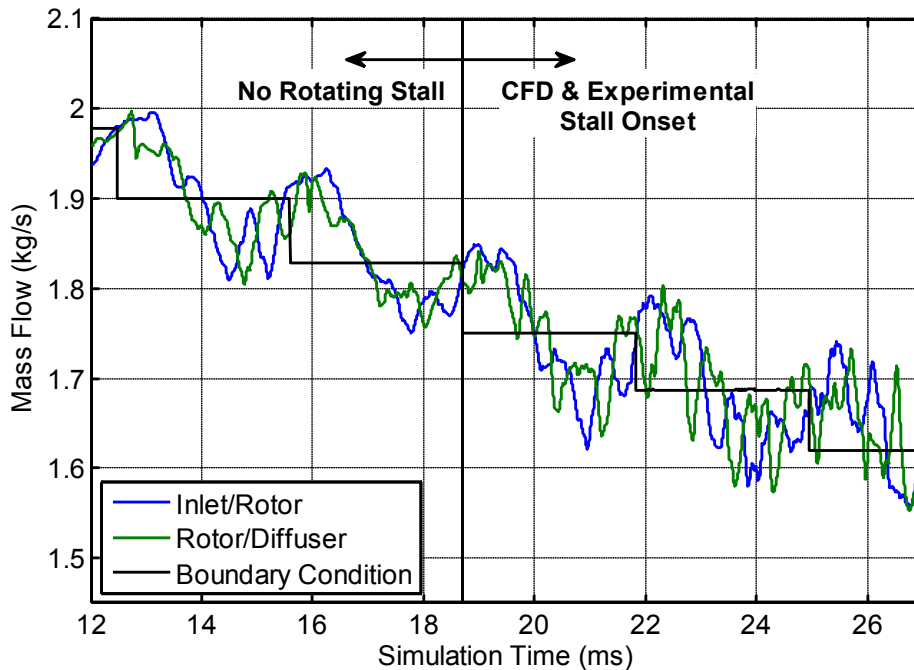


**Figure 5.6. Mass flow rates for the  $N = 19240$  rpm line, showing the onset of rotating stall determined in CFD and experiments**

Visual interpretation of the results in Figure 5.6 does not lead to a clear value for the onset of stall for the 19240 rpm line. The FFT analysis was therefore used to determine the onset flow rate more precisely. As in Figure 5.4, the mass flow rates at the Inlet/Rotor and Rotor/Diffuser boundaries were normalized using Equation (4.2). The signal was then split into stable and stalled operation portions, and the onset point was determined iteratively as the point where the supersynchronous fluctuations are predominantly in the stalled portion of the signal. Figure 5.7 shows the resulting split frequency spectrum for the stable region and the rotating stall region. The onset point found using this method was at 1.751 kg/s, which matches up exactly with the experimentally recorded data, as is seen in Figure 5.6.

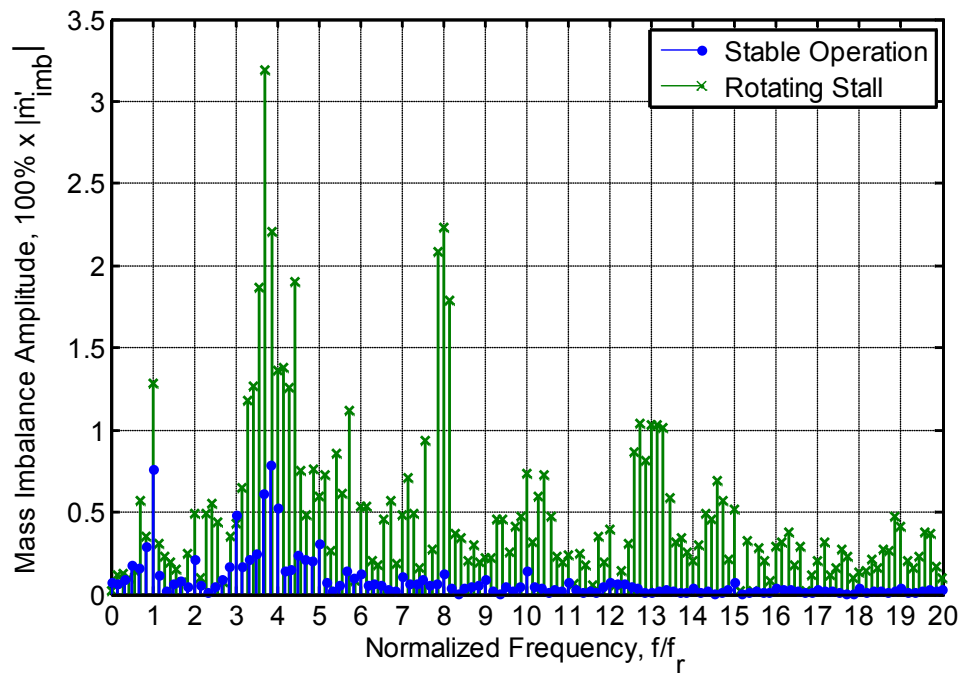


**Figure 5.7. Frequency spectrum of normalized mass imbalance, split between regions of stable and rotating stall operation for  $N = 19240$  rpm line, for an onset point determined at 1.751 kg/s**

As was seen in the split frequency spectrum for the 20640 rpm line in Figure 5.4 the spectrum in Figure 5.7 also shows a significant difference between the stalled and stable

operation regions. The stalled operation produces more significant peaks above the running speed, with three major peaks seen at  $3.75f_r$ ,  $8f_r$  and  $13f_r$ . In this case, the stable operation region also contains a peak at  $3.75f_r$ , but it is only 25% of the magnitude of the peak during stall. As before, both signals contain a peak at the running speed, which matches the forcing frequency of the mass drops applied at the boundary condition. However, it is again clear that the mass-flow fluctuations present in the numerical simulations can be used to detect the occurrence and onset of rotating stall within the compressor.

The velocity vectors at 50% span for four of the flow points on the  $N = 19240$  rpm speed-line simulation are shown in Figure 5.8, page 85. The first contour on the left, Figure 5.8(a), is taken at 1.978 kg/s, which is a stable point in both the experiments and according to the FFT analysis. As with the 20640 line, we see a small asymmetrical velocity fluctuation present in the impeller before a full rotating stall cell forms. Figure 5.8(b), taken at 1.828 kg/s, is the flow point directly before the numerical onset of stall. This point was not tested experimentally. The same asymmetric velocity disturbance is seen, but now two low speed locations exist at the top and bottom of the figure (the entire impeller circumference is not shown).

Figure 5.8(c) shows the transient results for a mass flow of 1.751 kg/s. This is the first point after the rotating stall onset in both the numerical and experimental results. Although the stall is mild, there is some reversed flow occurring near the leading edge of the bottom blades and a recirculation zone near the trailing edge of the central blades. The stall is characterized as a large single cell with the flow recovering near the top of the blade set. The same cell grows as the simulation moves further into the rotating stall regime, as seen Figure 5.8(d) at 1.556 kg/s. At the lower flow rate, the cell experiences a larger reduction in flow speed and covers a wider area of the impeller.

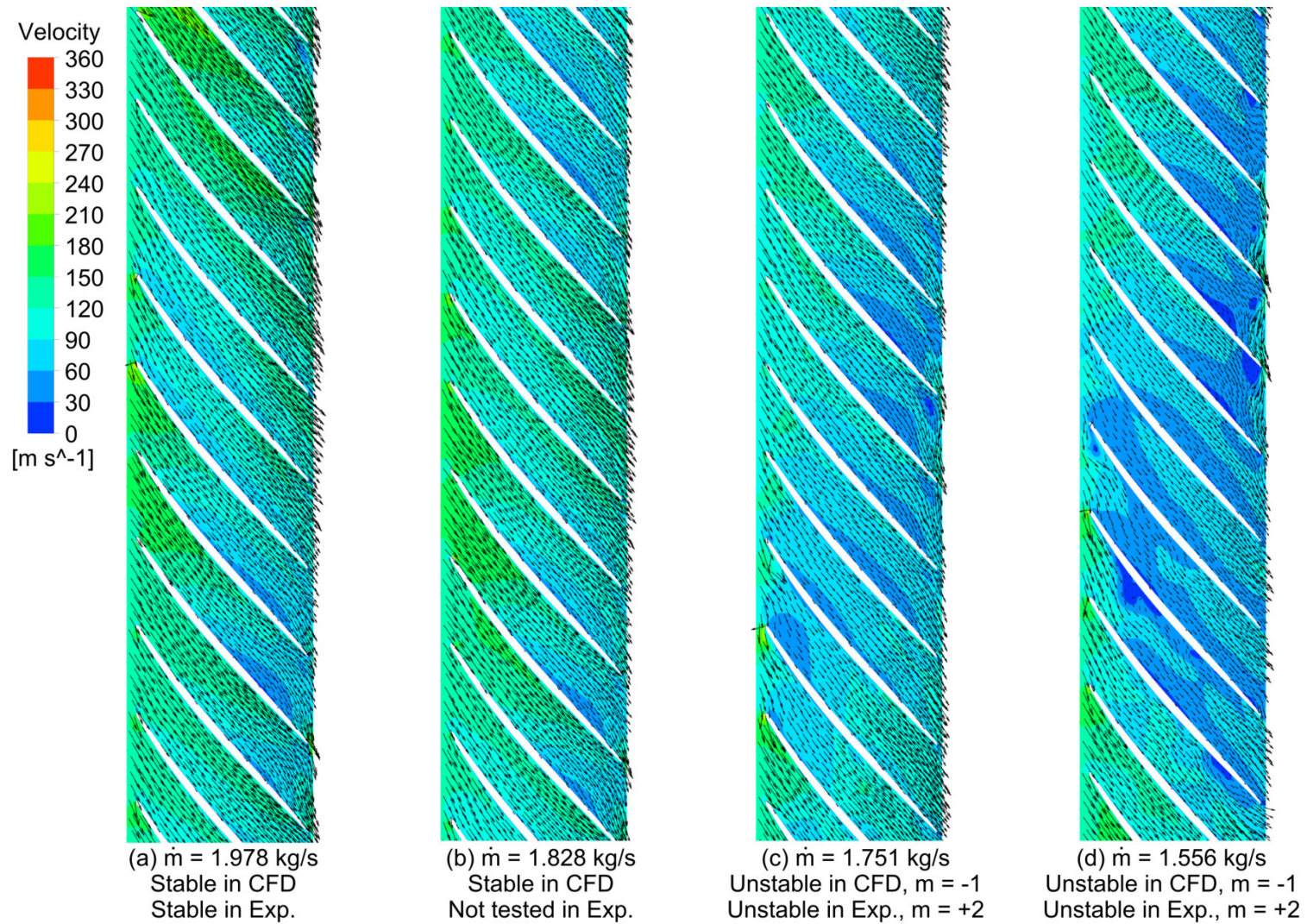


**Figure 5.8. Velocity contours showing rotating stall at various flow rates on the  $N = 19240$  rpm speed-line simulation. For each contour, the type of rotating stall found in CFD and experimentally is labeled for comparison.**

### 5.3 COMPARISON TO EXPERIMENTS

The compressor was tested for rotating stall using the methods detailed in Chapter 2. Two different return channels were used in the tests, and the compressor exhibited rotating stall behavior for both. However, it was noticed that while the return channels affected the type of stall developing in the compressor, they did not significantly change the onset flow rate at which the stall developed. It should also be noted that the experimental testing took much larger mass-flow steps than the numerical simulations, as determined by the sizing of the valves.

For the speed line at 19240 rpm, which was tested with both return channels, the onset of rotating stall was found to occur as the flow rate was dropped from 1.978 kg/s to 1.751 kg/s. This matches up exactly with the numerical results, which saw the onset of stall occur when the flow was dropped from 1.828 kg/s to 1.751 kg/s. While the step size is smaller in the simulations, the onset flow rate is the same. For the speed line at 20640 rpm, which was only tested with the original return channel, the onset of rotating stall was found to occur as the flow rate was dropped from 2.141 kg/s to 1.955 kg/s. In the numerical results, the onset was found to occur when the flow was dropped from 2.141 kg/s to 2.077 kg/s. Due to the larger step size in the testing results, the CFD estimates of the onset are within experimental uncertainty. The larger step size in the test valve may have incorrectly determined the onset flow, having jumped past the real onset during the flow adjustment. Either way, the simulation results show that the onset flow rate can be determined within a very accurate envelope of the actual results. However, from a compressor design perspective, it is also useful that the numerical simulations predict rotating stall to form at a higher flow rate than what was determined experimentally. Since operation during rotating stall is to be avoided, the limits imposed by the numerical simulations are actually more stringent than those discovered during testing.

## 5.4 CONCLUSIONS

The speed-line transient simulations were completed with the purpose of effectively determining the onset of the rotating stall phenomenon. The FFT analysis of the mass flow traces described in Section 4.2 was applied to iteratively determine the onset point for the rotating stall during the speed-line simulations. The detection of rotating stall onset in the numerical simulations was highly accurate when compared to the experimental results. Due to the larger flow step size in the testing results, the CFD estimates of the onset are within experimental uncertainty. The larger step size in the test valve may have incorrectly determined the onset flow, having jumped past the real onset during the flow adjustment. Either way, the simulation results show that the onset flow rate can be determined within a very accurate envelope of the actual results.

The simulation results also provided some insight as to the cause of rotating stall in this impeller. For both speed lines presented, the initial development of the instability occurs due to excessive blade loading halfway down the blade meridional length. For the majority of the flow conditions, the blade loading seems to be the main contributing factor to flow separation off the blades. Incidence at the leading edge only seems to be significant at few flow points, not for the entire range. The results also showed that the location and type of rotating stall can easily vary along the same speed line, which is also typically observed in experiments.

The results presented indicate that rotating stall and its onset can be accurately predicted using numerical simulations. The methods developed can be used to determine a more accurate compressor stability range before experimental testing. There currently is no precise method to predict the formation of rotating stall before experiments. Due to the large lead times and



material costs involved in testing compressors, being able to capture rotating stall formation in CFD offers a cost-effective alternative for compressor design. The following section will focus on applying the developed methods to aid in the design of a new compressor impeller with a larger stability range.

## CHAPTER 6: COMPRESSOR RE-DESIGN

### 6.1 OBJECTIVES

The previous chapters presented a methodology for accurately predicting rotating stall and its onset point. It is mentioned that these methods may be used to aid in compressor design before experimental testing. The following chapter applies that concept to re-design the tested compressor to avoid rotating stall. The re-design process is explained and the new design is validated using the transient CFD methodologies developed.

The main objective of the compressor re-design is to reduce the appearance of rotating stall, or to widen the compressor's stable operating range. This may be achieved by decreasing the rotating stall onset point further towards surge, or by removing the phenomenon completely from the operating range for the compressor. In addition to this primary objective, three major requirements must be met during the redesign:

- 1) The head characteristic of the re-design must match that of the previous impeller. This is the most important restriction. This compressor is purposed for high-pressure pipeline use, and head rise is most important parameter, otherwise the compressor cannot pressurize the flow to the desired downstream pressure and is not useful towards the design purpose. In this case, the entire head characteristic from choke to surge, not just at the best efficiency point, must match as closely as possible with the original compressor's characteristic.

- 2) The re-design must require the least amount of modifications to existing parts. Re-design of the impeller is necessary, but to reduce costs the use of pre-existing parts for the inlet, diffuser and return channel is preferred. For this compressor, that requires keeping the same impeller length, hub diameter, meridional shroud curve, diffuser and return channel geometries.

By using the same shroud curve, the following parameters are also fixed: inlet blade height, exit diameter and exit blade height. There are two main design options left: modifying the hub curve (the more difficult choice, since there are no signs of separation or stagnation along that surface) or the blade angle distribution (the more logical choice, as it will directly affect the blade loading and flow separation off the blade). Therefore, the re-design presented in this chapter will focus on the blade angle distribution and its effect on the rotating stall onset.

3) The last requirement is to maintain the compressor's efficiency. The stage efficiency characteristics of the compressors must match as closely as possible. This is of high importance for pipeline compressors, as the compressor runs continuously for long periods of time, and higher efficiency equates to large savings when applied over lengthy time periods. However, due to the nature of the device, it is more important to achieve the desired pressure ratio while having a large operating range rather than having the desired efficiency for only a narrow operating range. It is acceptable to sacrifice a few efficiency points if the compressor can achieve a larger operating range.

## **6.2 BLADE DESIGN**

In order to aid the re-design process, the original compressor was analyzed at off-design flow points using both a 1-D performance code and steady-state CFD. The results are used in conjunction with the previously presented transient CFD to help identify problems in the original design that may cause the rotating stall to develop. This section will present the results of that analysis and the recommendations for the re-design of the impeller blades.

There exist two possible causes for rotating stall in this impeller: incidence and blade loading. The first step in the re-design is to determine which will dominate the development of

rotating stall in the impeller. From the fixed-flow transient simulations, the disturbance appears near the leading edge of the impeller, and propagates due to excessive incidence between the flow angle and blade angle. However, the speed-line transient simulations show that the dominant form of rotating stall throughout the entire speed line is due to excessive blade loading near the mid-length of the blade.

In order to determine the effect of incidence on the development of rotating stall, the incidence angle, defined in Equation (6.1), was calculated using both a 1-D performance code and steady-state CFD simulation. The 1-D prediction includes the geometric blockage from the blades, but not any aerodynamic blockage caused by the boundary layers off the blades. The results for the original design are plotted in Figure 6.1.

$$\delta_1 = \beta_{1b} - \beta_{1f} \tag{6.1}$$

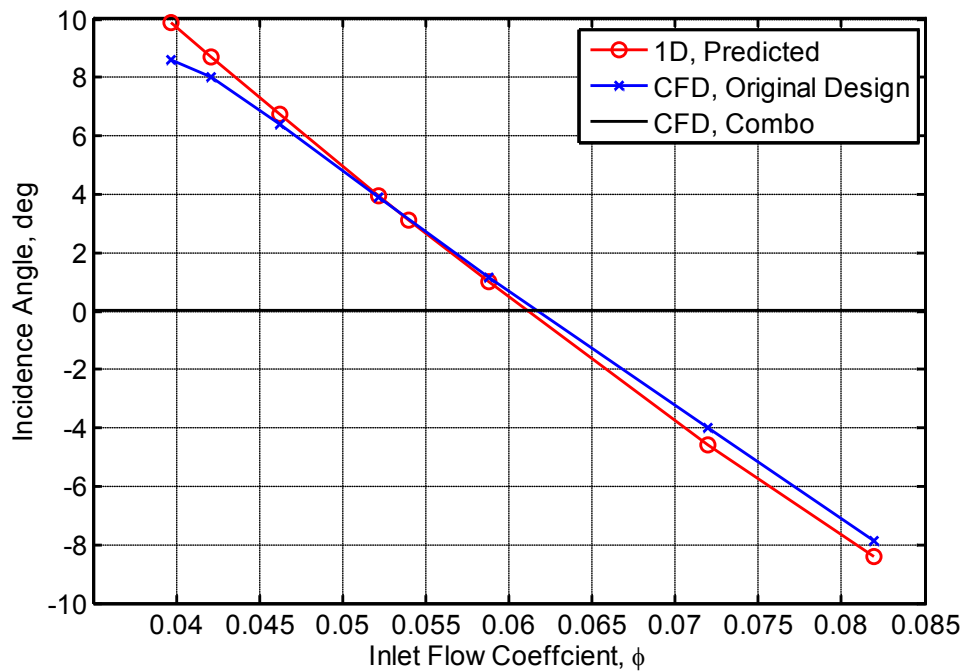


**Figure 6.1. Incidence angle comparison for the original design**

The results from CFD and the 1-D code match to within  $1.3^\circ$ , with the largest difference occurring at the smallest flow rate. The difference between the two lines is due to the added aerodynamic blockage that is taken into account by the CFD results. The two lines show that the prediction is accurate. At the design point,  $\varphi_1 = 0.054$ , the incidence angle is  $3.13^\circ$ , which is a typical design value in order to increase the compressor's range near choke. The general recommendation for compressor design is to keep the absolute value of the incidence below  $10^\circ$  or  $12^\circ$  to avoid separation off the leading edge of the impeller [2,7]. From the results in Figure 6.1, it is obvious that the original design fits within this requirement, yet rotating stall still occurs in the impeller. Because of this, the re-design efforts will concentrate on the blade loading across the impeller, keeping the inlet blade angles constant at  $\beta_{1h} = 34.4^\circ$  and  $\beta_{1s} = 25.9^\circ$ .

The blade loading across the impeller length is mainly determined by the blade shape, which is characterized by the blade angle distribution. Figure 6.2 shows the blade angle distribution for the original design, along with the distribution for two proposed re-designs. The blade angles are calculated from the tangential direction, and are plotted against the normalized meridional distance along the blade,  $M$ , where 0 represents the leading edge and 1 represents the trailing edge. The original design uses an unconventional distribution for the blade shapes. At the leading edge, the gradient of both the hub and shroud lines is similar. This is useful to increase the compressor's performance near choke. However, at the trailing edge the two curves do not converge to the same value and both curves still have some slope. Conventional designs usually have the trailing edge values for both hub and shroud equal and with zero slope.

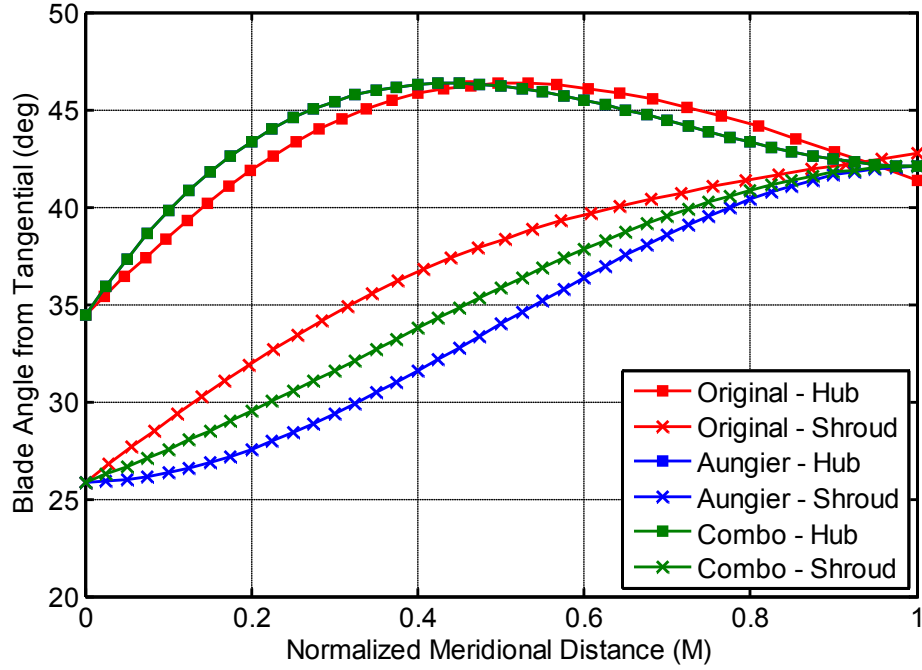


**Figure 6.2. Blade angle distribution for the original design and for two proposed re-designs**

Two re-designs are proposed for the blade angle distribution of the impeller. The first re-design follows the method proposed by Aungier [71]. This method uses a cubic equation for both hub and shroud curves, but forces both curves to a zero gradient at the trailing edge. Additionally, it forces the leading edge of the shroud curve to have zero gradient, while indirectly controlling the initial gradient of the hub curve using a single parameter,  $K_h$ . The equations are given below.

$$\beta_s = \beta_{1s} + (\beta_2 - \beta_{1s})(3M^2 - 2M^3) \quad (6.2)$$

$$\begin{aligned} \beta_h &= \beta_{1h} + AM + BM^2 + CM^3 \\ A &= -4(\beta_2 - 2\bar{\beta}_h + \beta_{1h}) \\ B &= 11\beta_2 - 16\bar{\beta}_h + 5\beta_{1h} \\ C &= -6\beta_2 + 8\bar{\beta}_h - 2\beta_{1h} \\ \bar{\beta}_h &= 90K_h + (1 - K_h)(\beta_2 + \beta_{1h})/2 \end{aligned} \quad (6.3)$$

The value of  $K_h$  was chosen to be 0.1537, resulting in a hub blade angle distribution with the same maximum value as the original design. The exit blade angle was chosen as the average value of the original design's two curves,  $\beta_2 = 42^\circ$ . The Aungier re-design, also shown in Figure 6.2, has a zero gradient at the exit. The resulting hub curve has a larger gradient at the inlet and the maximum value is shifted toward the leading edge by the decision to reduce the trailing edge gradient. The shroud curve produced by the Aungier method has zero gradient at both inlet and exit, resulting in a very different shroud curve from the Original design.

One more design was produced, a combination of the Original and Aungier designs, to take advantage of the benefits of both. It was named the "Combo" design. In this case, the exit conditions from the Aungier design are matched, but the shroud is given an initial gradient. The hub curves for the Combo and Aungier designs match exactly. The shroud curve is modified to have an initial slope, which is not possible following Aungier's design methodology. The equation for the shroud curve was derived to have a single control parameter,  $K_s$ , which equals the inlet gradient of the shroud curve.

$$K_s = \left. \frac{d\beta_{1s}}{dM} \right|_{M=0} \quad (6.4)$$

$$\beta_s = \beta_{1s} + K_s(M - 2M^2 + M^3) + (\beta_2 - \beta_{1s})(3M^2 - 2M^3) \quad (6.5)$$

The value of  $K_s$  was chosen to be 15.057, which results in an inlet slope that is exactly half of that for the Original design. The Combo re-design is also shown in Figure 6.2. The resulting shroud curve lies between the Original and Aungier designs. This should give a better performance near choke while decreasing the blade loading near surge.

As an additional check, the incidence angle analysis was repeated for the Combo design using steady-state CFD. The 1-D predicted values for the incidence angle remain the same, since the inlet blade angles are the same, but the CFD results for the Combo re-design are much closer than those for the Original design, as seen in Figure 6.3. From these results, it can be concluded that the improved slope near the leading edge of the blades is helping to guide the flow into the blade passage, producing less separation. The lower separation decreases the aerodynamic blockage of the flow, matching the 1-D prediction more closely than the Original design could.

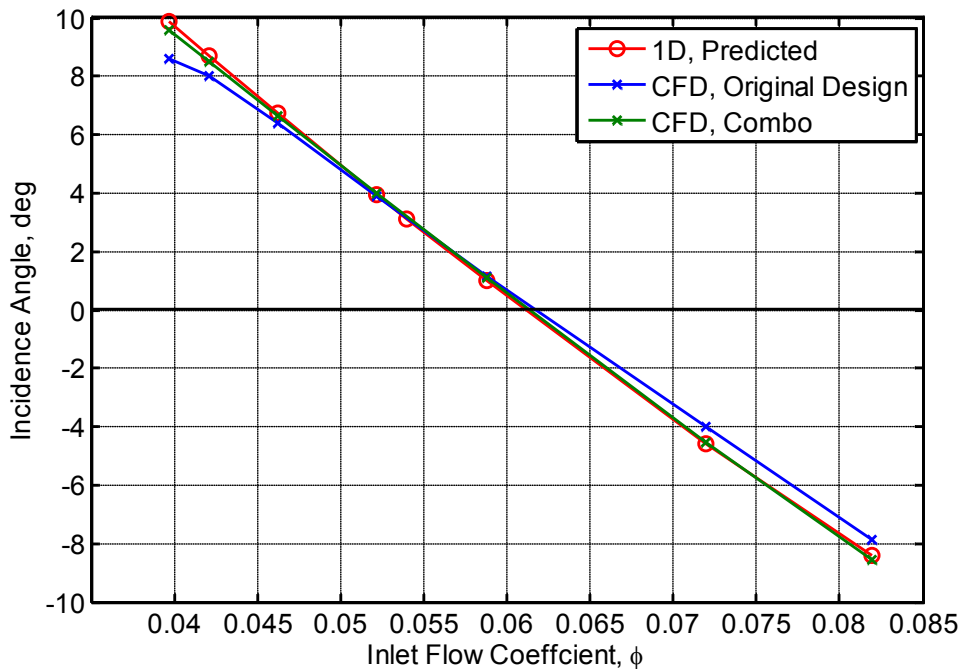


**Figure 6.3. Incidence angle comparison for the original design and Combo re-design**

### 6.3 STEADY-STATE PERFORMANCE

In the previous section, two different choices for the re-designed impeller are presented. From these options, a final design needs to be chosen for the compressor. In order to do this, the various options are simulated using steady-state, single-passage CFD in order to have an accurate



prediction of off-design performance and blade loading effects. The CFD analysis for the original compressor was presented and validated in Section 3.2. The steady-state CFD results for the re-designs are completed using the same methods that were used for the original design. The performance results are plotted in Figure 6.4. The Original design is shown, along with the Aungier and Combo re-design results. Additionally, the Aungier design was also run with 13 blades instead of 15 blades, to improve its performance near choke.

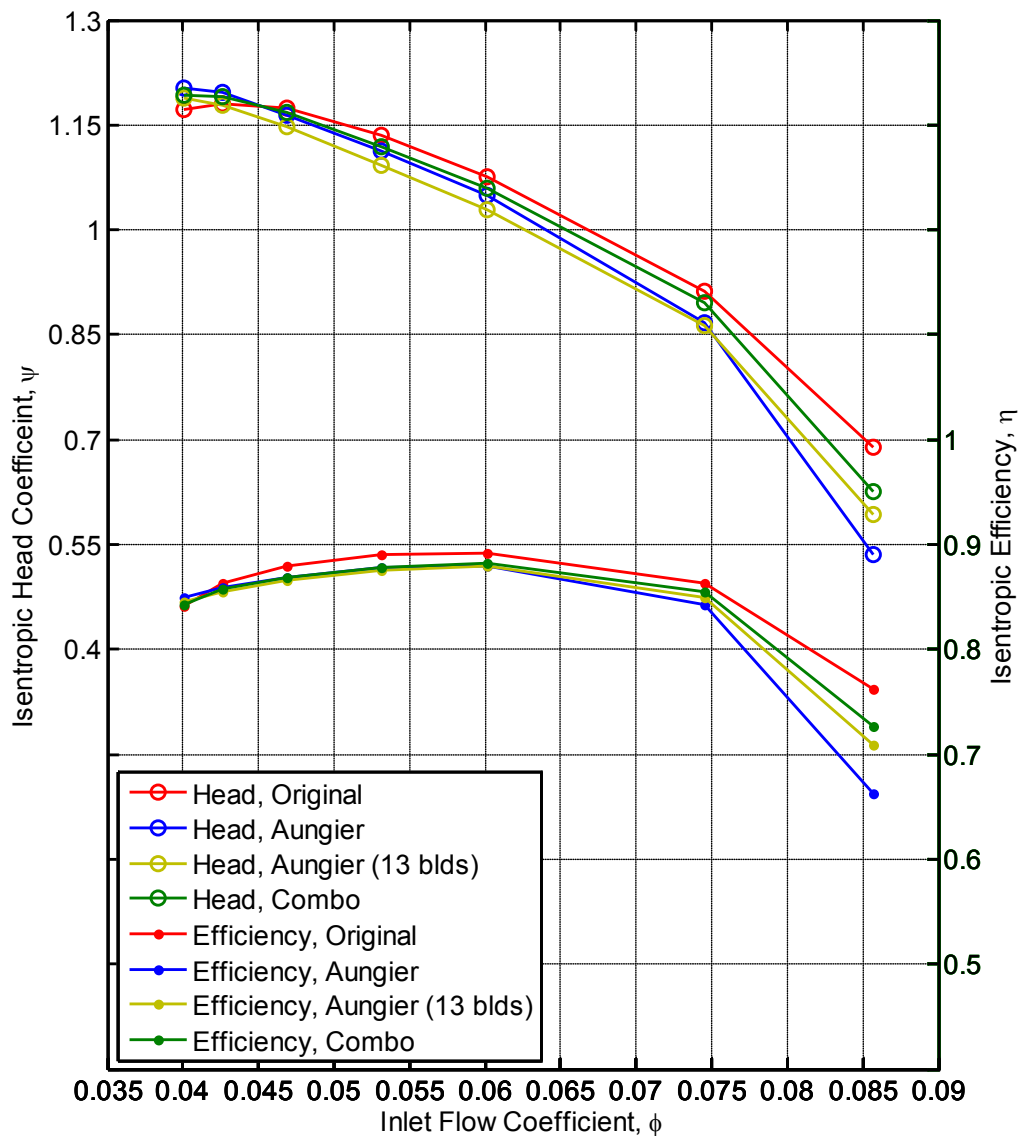


**Figure 6.4. Isentropic head coefficient and efficiency comparison between original design and various re-design options for  $N = 19240$  rpm**

The Aungier design has a satisfactory performance near the design point,  $\phi_1 = 0.054$ , with the head coefficient drop of 2% from the Original value and a drop of 1.2% in efficiency. It even exceeds the performance near surge by 2.5% in head and 0.8% in efficiency. However, the performance near choke does not meet the necessary requirements. The head coefficient is 22.4% lower, while the efficiency is 9.9% lower. The difference in performance can be attributed to a lower choke point for the Aungier re-design than the Original impeller.

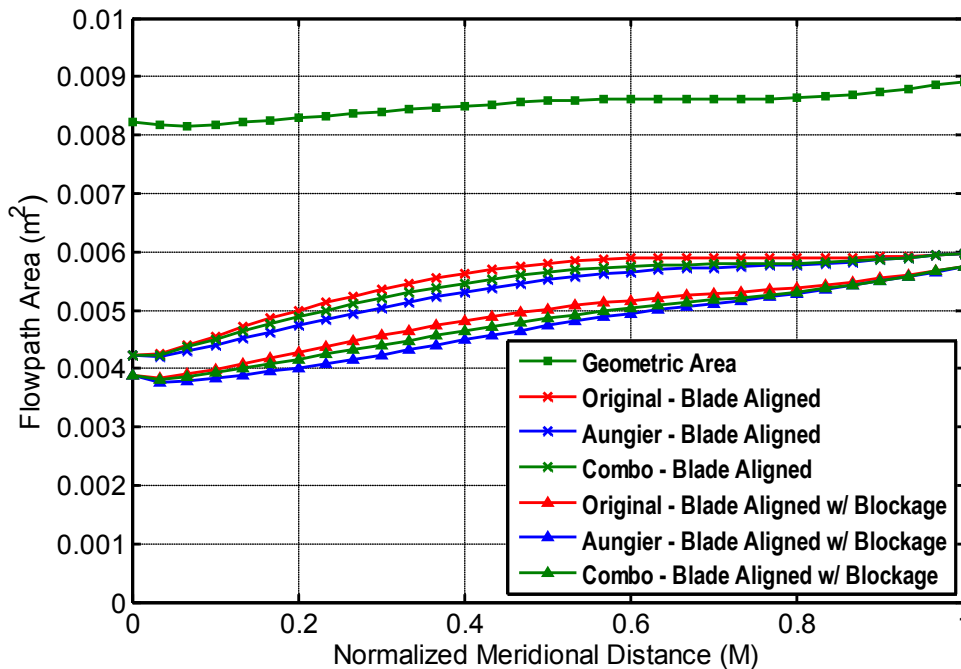


**Figure 6.5. Comparison of flowpath area for the various designs**

The effects of the new blade distribution on the flowpath area can be seen in Figure 6.5. The hub and shroud meridional curves are the same, so the geometric area for all three designs does not change. However, the real throat of the impeller is normal to the blades, resulting in a smaller area than the geometric one. For this blade-aligned area, the gradients between the blade angles have an important effect. Additionally, including the blockage caused by the thickness of the blades decreases the area even further. The minimum area for all three designs occurs right

after the leading edge, but the Original design is the widest due to the similar slopes between the shroud and hub curves. The Aungier design has the most deviation between the slopes at hub and shroud, and therefore has the smallest blade-aligned area.

From these observations, it was decided to attempt to decrease the number of blades for the Aungier design from 15 to 13. The results are also shown in Figure 6.4. The benefit of removing two blades is clearly visible, as the choke point has moved to a higher flow rate. However, compared to the 15 blade Aungier, the performance near design point and near surge is hindered. The reduction of two blades increases the slip between blades and fluid, reducing the pressure ratio at lower flow points.

Finally, the Combo design performance is also plotted in Figure 6.4. As expected, the performance of the Combo design falls right between the Aungier and Original lines. The head coefficient is lower than the Original by only 1.5% at design point and is within 1% for the lower flow rates. Near choke, the Combo design is better than both the 15 blade and 13 blade Aungier designs, with a drop in head of 9%. Similarly, the efficiency near choke is lower by 3.5%, but it is within 1% of the Original design at all the other flow points. The most important requirement for the new design was to match the original design's head characteristic as closely as possible, which is best met by the Combo design. For this reason, it was chosen to continue the re-design effort using this blade geometry.

## **6.4 BLADE LOADING**

Further steady-state CFD analysis of the Combo design was completed to determine if the re-design achieved the desired results with regards to blade loading, before attempting the full 360° transient simulations. The blade loading on a centrifugal impeller is commonly defined

using the relative fluid velocity along the suction side,  $W_{ss}$ , and pressure side,  $W_{ps}$ , of the blade. The mean velocity,  $\bar{W}$ , is also used to indicate the overall diffusion through the impeller. The three parameters can be further combined into a single blade loading coefficient,  $\lambda$ .

$$\lambda = \frac{\Delta W}{\bar{W}} = \frac{W_{ss} - W_{ps}}{\bar{W}} \quad (6.6)$$

From the definition, high values of blade loading occur when the suction side velocity is much greater than the pressure side velocity. When flow separation occurs off the suction side of the blade, that side's velocity decreases suddenly, so the blade loading coefficient becomes negative.

The design of compressor blades for appropriate blade loading is an iterative process usually completed using a 2-D or CFD solver at the design point of a compressor. There are three general recommendations for the design of high-efficiency impellers [72]. The overall flow velocity should be decelerated as soon as possible in the impeller, in order to prevent the formation of thick boundary layers and decrease the frictional effects on the flow. The maximum loading value should occur near the center of the blade, after the deceleration region, to avoid boundary layer separation and to maintain the velocity on the suction side relatively constant. Finally, a light loading should be used close to the impeller exit, to delay the formation of the jet-wake flow pattern as much as possible. An additional requirement has been reported when calculating the blade loading coefficient: the maximum value should not exceed 0.65 [2].

The blade loading plots and the blade loading coefficient for both the Original design and the Combo re-design are shown in Figure 6.6, at the near-design point for this compressor:  $\phi_1 = 0.0531$  and  $N = 19240$  rpm. The blade loading is calculated and plotted at three heights through the impeller span: 20% (near-hub), 50% (meanline), and 80% (near-shroud). Neither of the plots for the Original design show any problems conforming to the recommendations listed above, so

running a design point CFD analysis would not indicate this compressor would have any problems with rotating stall or boundary layer separation. The Combo design results have a slightly smoother diffusion, but have no significant difference from the Original design.

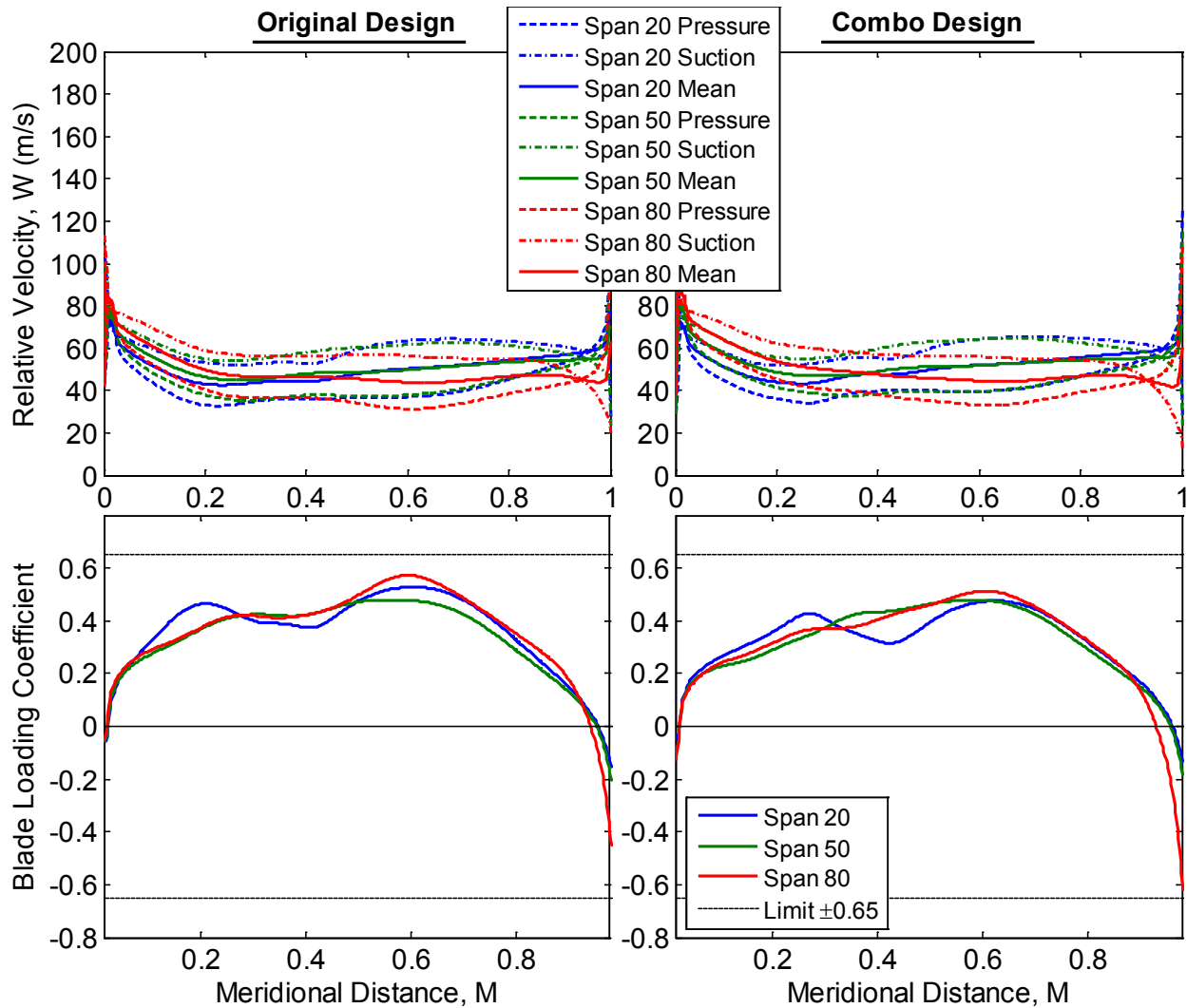


**Figure 6.6. Blade loading comparison between the Original and Combo designs, at near-design point  $\phi_1 = 0.0531$  and  $N = 19240$  rpm**

Rotating stall, however, does not occur at the design point. The blade loading for the two designs was also compared at a near-surge flow point:  $\phi_1 = 0.0426$  and  $N = 19240$  rpm. In this case the blade loading plots for the two designs look drastically different, as seen in Figure 6.7.

The Original design clearly had a significant amount of separation along the blade, while the Combo design has relatively little. Separation occurs when the suction side velocity decreases suddenly and the blade loading coefficient becomes negative. It is normal for the separation to occur first near the shroud, where the flow needs to negotiate the tightest turn. For the Original design, separation occurs first near the shroud, at 80% span. For this height, the flow has separated off the latter 48% of the blade. At the meanline there is also a significant amount, off the last 18.7% of the blade. At the near-hub there is still little to no separation.

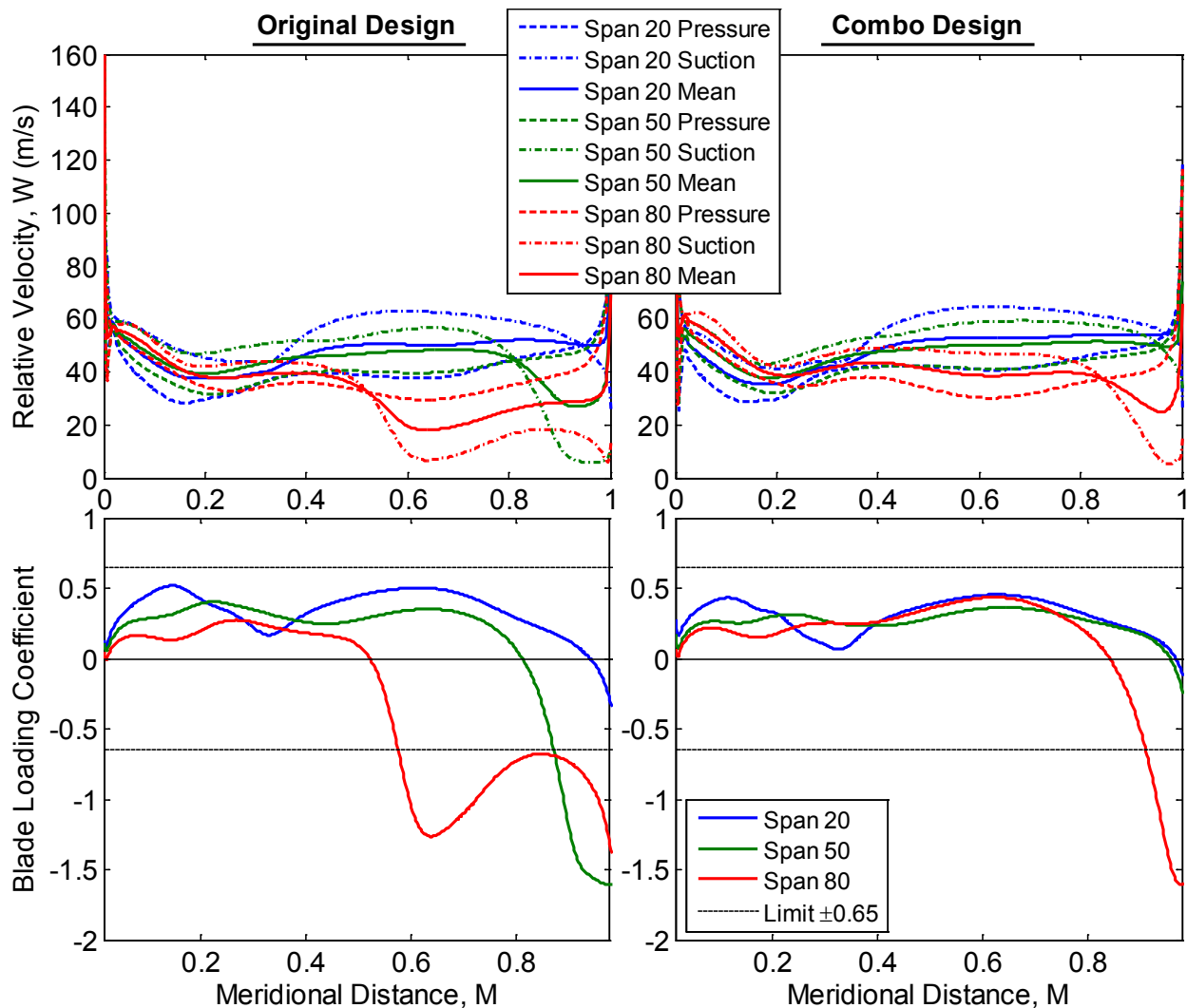


**Figure 6.7. Blade loading comparison between the Original and Combo designs, at near-surge point  $\phi_1 = 0.0426$  and  $N = 19240$  rpm**

The Combo design corrects some of this issue. For the near-shroud line, the separation is greatly reduced, covering only the last 15.7% of the blade. The meanline and hub curves also show little to no separation, a great improvement over the Original design. The comparison of the two designs clearly indicates that the Combo design will have a more stable operation near-surge than the Original design.

The blade loading coefficient plot for the Original design also brings up one more observation. When the separation occurs, the blade loading becomes negative and exceeds the 0.65 limit maximum imposed empirically. This does not have great significance from an aerodynamics perspective, but may have important implications of rotor stress and vibrations. During rotating stall, the boundary layers separate and re-attach at very high frequencies. The large inverse loading seen in the separated flow region indicates that the forces involved in the separation and reattachment of the boundary layer may be very large, causing the vibrations in the impeller that are seen experimentally.

As the compressor approaches surge, separation always occurs. The goal is to reduce the amount of separation. If the separation can be pushed to a lower flow rate, the stable range of the compressor is increased. Because of this, the Combo design shows the potential to have a greater stability range than the Original design. It was therefore selected as the best re-design possibility and will next be analyzed using the full 360° transient simulation methods developed in this research to confirm whether the re-design efforts were successful.

## **6.5 SPEED-LINE TRANSIENT RESULTS**

The final step to the re-design process consists of determining if the changes to blade angle distribution caused an improvement in the stable operating range of the compressor. Since

the Combo design fits the requirements best, the speed-line simulations presented in the previous chapters are repeated for this re-designed compressor to predict the new rotating stall onset. The overall geometry is fairly similar to the original design, so a new mesh was developed with the same meshing parameters and number of elements that were used for the original design. The speed line simulations were run for the 19240 rpm line, starting at a stable mass flow rate of 1.978 kg/s, and for the 20640 rpm line, starting at a stable mass flow rate of 2.345 kg/s. The time step was again chosen so that 750 time steps are required for one full impeller revolution.

The results for the 19240 rpm line are presented first. Figure 6.8 shows the mass flows at the rotor-stator interfaces near the rotating stall onset for the Combo redesign. For comparison, these are super-imposed over the mass flow traces from the Original design that were reported in Figure 5.6. In comparing the signals for the Original and Combo designs, three diverse regions can be distinguished. The first region, before the drop to 1.751 kg/s, is similar in both cases. The mass flows attempt to follow and converge to the boundary condition, and have little to no high frequency content. This area does not contain any indication of rotating stall occurring in the compressor, for either the Original design or the Combo design.

On the right of Figure 6.8 there is a second region where the signals from the Original and Combo designs match. After the boundary condition drops to 1.619 kg/s, the two signals contain high frequency fluctuations that deviate significantly from the boundary condition value. This is indicative of rotating stall operation, and after this point both the Combo and Original are clearly being affected by the phenomenon.



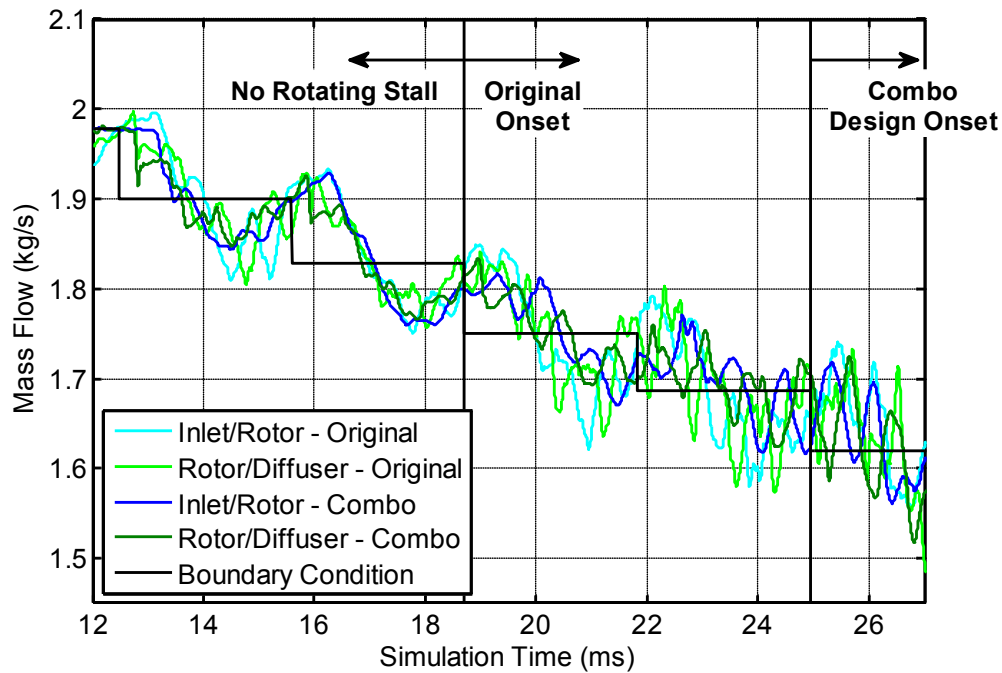


**Figure 6.8. Time-record of mass flow rates for the  $N = 19240$  rpm line, showing the onset of rotating stall for both the Original and Combo designs**

In the central region of the figure, where the boundary mass flow rate is 1.751 kg/s and 1.687 kg/s, the signals for the Original and Combo designs differ the most. In the Original design, it was clear that rotating stall was occurring, as was confirmed by both the FFT analysis and CFD velocity vectors. However, for the Combo design, the fluctuations do not appear suddenly, but rather grow slowly over time. This transition region, in which the fluctuations grow from stable operation into rotating stall operation, shows some unsteady and non-axisymmetric flow behavior but does not contain any of the reversed or stalled flow that is characteristic of rotating stall. Therefore, the rotating stall onset for the Combo design is located after the transition region, at 1.619 kg/s.

The FFT analysis confirms the placement of the rotating stall onset after the transition region. As with the signals from Sections 5.1 and 5.2, the mass flow traces for the Combo design are normalized using Equation (4.2) and the resulting signal is split into two regions: stable

operation and rotating stall operation. In this case, the transition zone between the two is included in the stable operation segment, so the split is located at 1.619 kg/s. The results of the FFT analysis are shown in Figure 6.9, superimposed over the results from the Original design, previously shown in Figure 5.7.

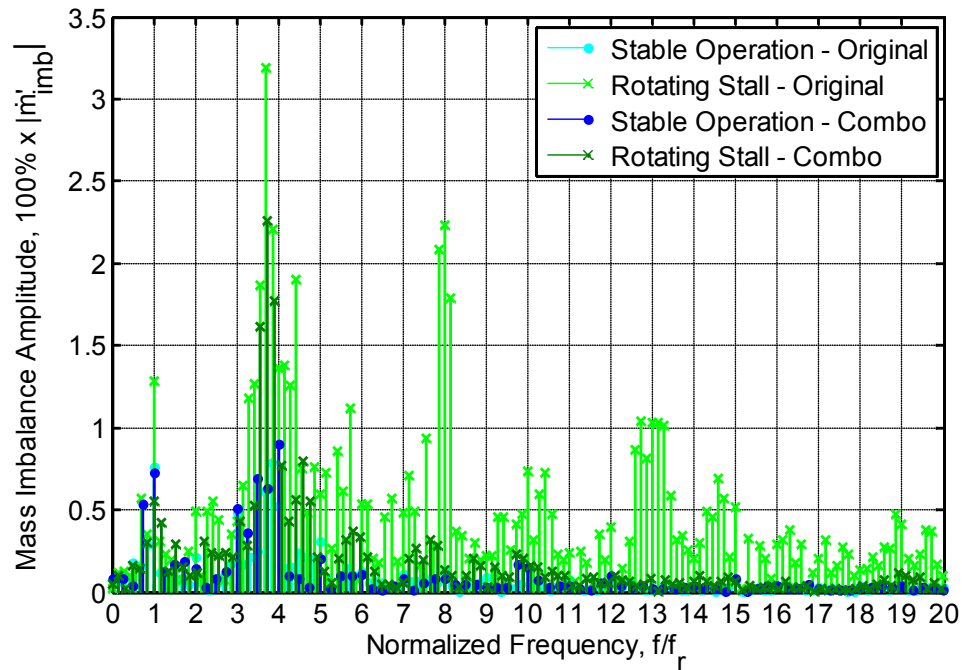


**Figure 6.9. Frequency spectrum of mass imbalance for both Original and Combo designs for  $N = 19240$  rpm line, split between regions of stable and rotating stall operation**

The FFT analysis for the Combo design is significantly decreased in magnitude from the Original design. However, the frequency peaks are located at the same values. All the signals still contain the forcing response at  $f/f_r = 1$ . The stable operation portions for both the Original and Combo designs are nearly identical. The rotating stall operation for the Combo design still shows a peak at  $3.5f_r$  and only two small peaks at  $5.8f_r$  and  $7.6f_r$ . Combined with the decreased magnitude of the main peak, this may indicate that the stall pattern observed in the Combo design is milder than that observed in the Original design.

The occurrence of rotating stall and the existence of the transition zone are also confirmed by the CFD velocity profiles. Figure 6.10 shows the CFD results seen in the three zones defined for this design: stable operation, transition and rotating stall operation.

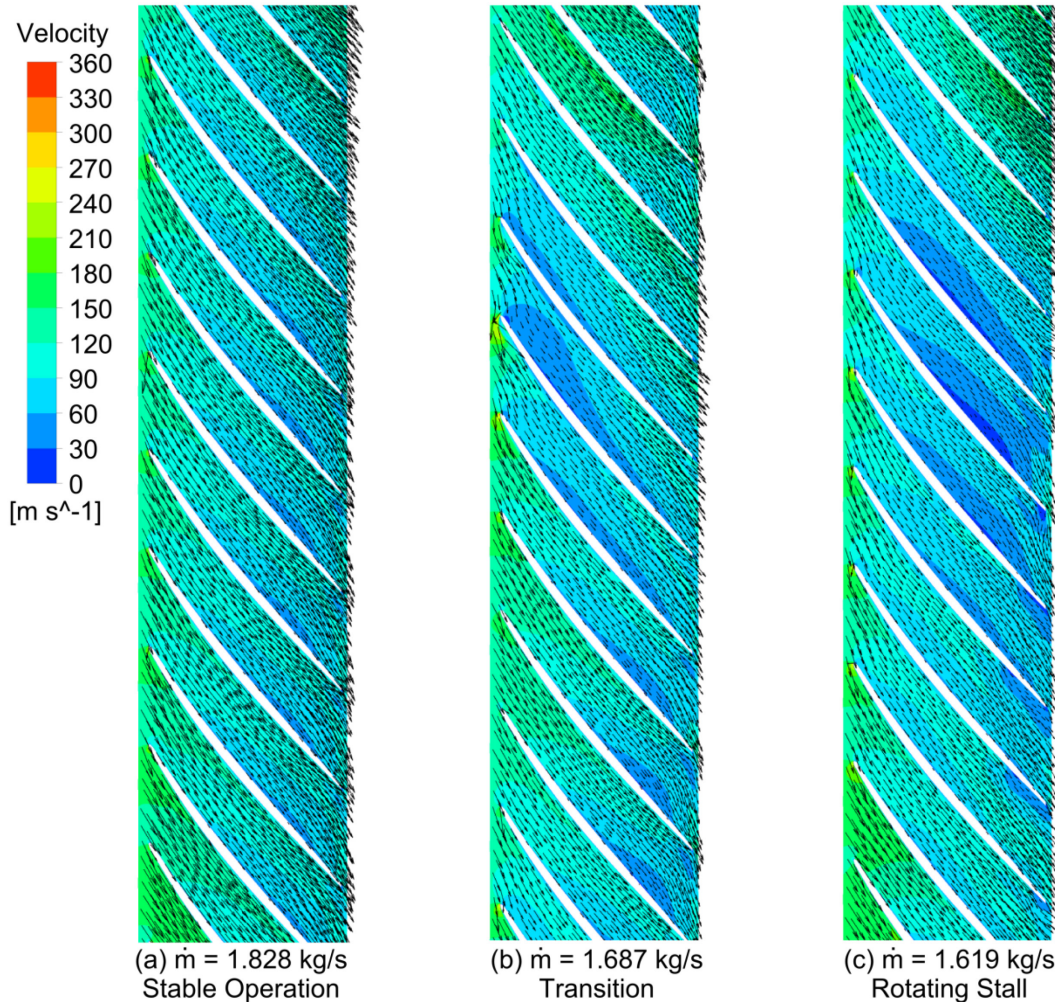


**Figure 6.10. Velocity contours showing stable, transition and rotating stall operation on the  $N = 19240$  rpm speed-line simulation for the Combo design**

The first flow point, seen in Figure 6.10(a) at a flow of 1.828 kg/s, is stable and shows no signs of rotating stall or of any high-frequency oscillations in the mass flow. The velocity vectors confirm that the flow is mostly uniform, but a slight non-uniform prestall wave can be seen. The flow near the center of the blade rows is slightly decelerated as compared to the flow on the top

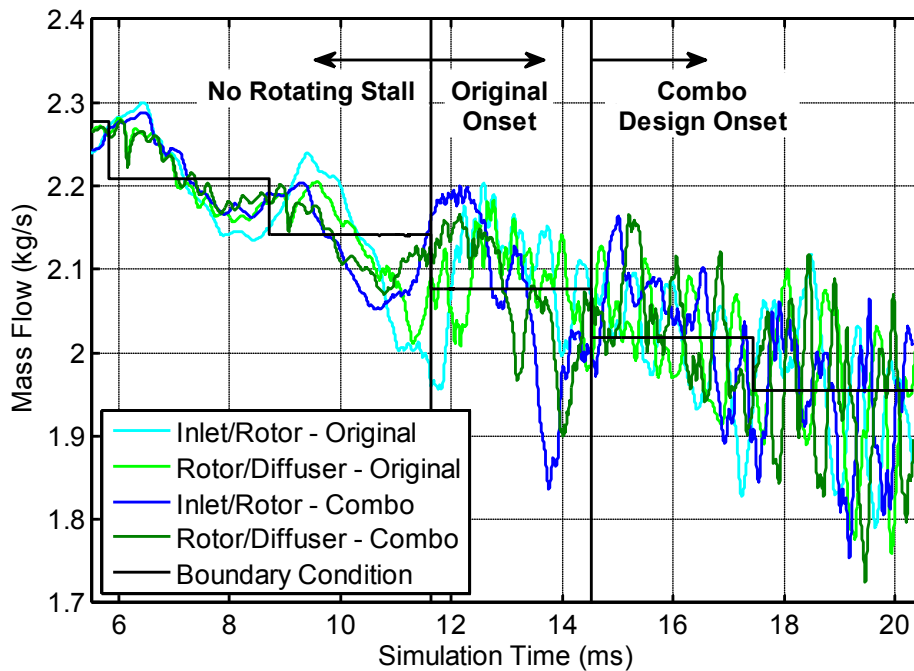
and bottom of the blade set. The flow separation still seems to be occurring at the same location as in the Original design, but the size of the separation zone is smaller.

Figure 6.10(b), taken at 1.687 kg/s, displays the flow profile in the transition zone. The flow does show a single cell of unsteady, non-axisymmetric flow. The cell is large enough to cause the velocities in proximity to decrease, but it does not cause any flow stagnation or reversal, which does not match with the characteristics of a rotating stall cell. However, this disturbance easily grows into a full stall cell once the boundary condition flow rate is decreased again. In Figure 6.10(c), at a flow of 1.619 kg/s, the rotating stall cell has fully developed and is causing both flow blockage and some reversed flow near the trailing edge of the blades. In this figure, the rotating stall cell can be easily discerned.

For the 19240 rpm line, the Combo design's rotating stall onset is moved to 1.619 kg/s. The transition zone is not included in this value, as the disturbances that appear in it do not develop into stall cells. The Original design had an onset flow of 1.751 kg/s. In terms of stall margin, Equation (5.1), the improvement of the Combo design is of 6.651% over the Original design. This is a significant amount when considering that the only changes made to the design were in the blade profiles, and no other parts were modified.

The results for the 20640 rpm line show a similar improvement. Figure 6.11 shows the mass flows at the interfaces for the Combo re-design and the Original design, which were previously reported in Figure 5.3. Again, three diverse regions can be distinguished. The first region, before the boundary condition drops to 2.077 kg/s, does not contain rotating stall. The signals from the two designs match closely, and show no high-frequency oscillations. The transition zone at this speed is smaller than for the 19240 rpm speed line, taking up only the mass flow step at 2.077 kg/s. Again, the transition zone begins where the onset for the Original design

was previously located. Finally, the Combo design's rotating stall onset is found at 2.018 kg/s. After this point, both designs show similar trends and the high-frequency content associated with rotating stall.



**Figure 6.11. Time-record of mass flow rates for the  $N = 20640$  rpm line, showing the onset of rotating stall for both the Original and Combo designs**

The FFT analysis results for the Combo design's 20640 rpm line are shown in Figure 6.12, superimposed on the results from the Original design presented in Figure 5.2. The transition zone is included in the stable operation section of the signal, so the split is located at 2.018 kg/s. As with the lower speed line, the two stable operation signals are very similar. The only difference comes near  $3.5f_r$ , where the Combo re-design does have a peak of similar magnitude to that of the forcing frequency. This is due to the inclusion of the transition zone in the stable portion of the signal. However, the peaks are not large enough for rotating stall to be expected.

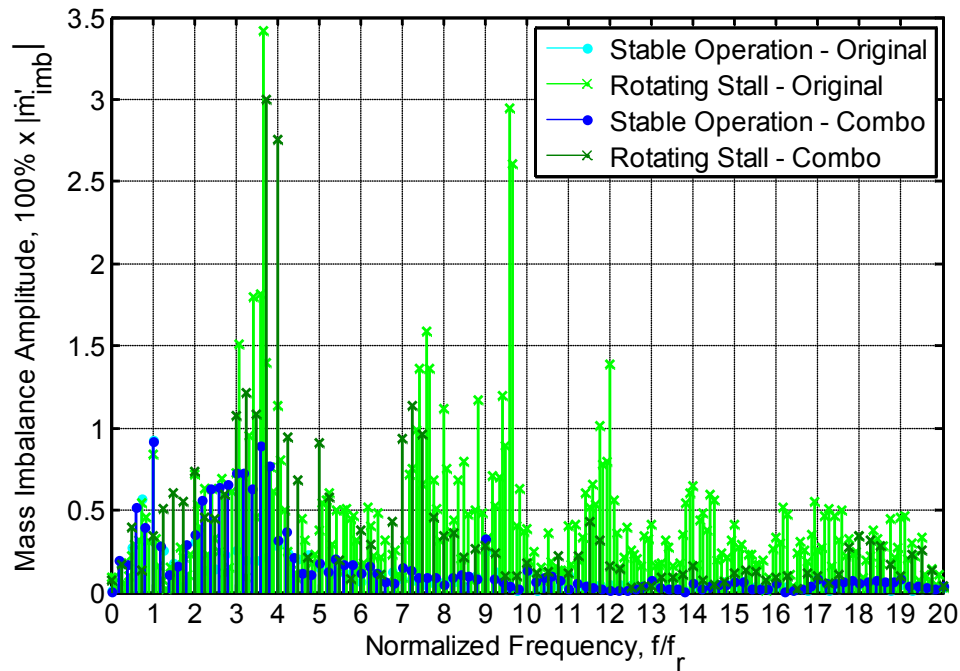


**Figure 6.12. Frequency spectrum of mass imbalance for both Original and Combo designs for  $N = 20640$  rpm line, split between regions of stable and rotating stall operation**

The rotating stall portion of the signal for the Combo design is also very similar to that of the Original design. The main peak at  $3.5f_r$  still is present, and is of similar magnitude. Additionally, a peak at  $7.25f_r$  is observed and smaller peaks at  $11.5f_r$  and  $18f_r$  are present. While the signals for the Original and Combo designs do not match exactly, the trends are the same. The rotating stall portion of the signal contains multiple high-frequency peaks that are not present in the stable operation segment. The modification of the blade angles has forced the form and number of stall cells to change, leading to different frequency contents in the signals.

Finally, the CFD velocity profiles, shown in Figure 6.13, confirm the onset point determined by the mass flow and FFT results. The flow point in Figure 6.13(a) is taken at 2.141 kg/s, in the stable region of the signals. The flow at this point is uniform, only a very small deceleration can be seen near the bottom of the blade rows. Figure 6.13(b), taken at 2.077 kg/s, displays the flow profile in the transition zone. In this case, some non-axisymmetric flow



separation occurs near the trailing edge of the blades. It is a small area that does not affect the overall velocities through the blades. The flow in the transition zone again does not match with rotating stall, but does contain an unsteady disturbance that causes some of the additional high-frequency content in the FFT analysis. Finally, in Figure 6.13(c), at a flow of 2.018 kg/s, the rotating stall cell is seen clearly. Once again, the stall seems to originate due to excessive curvature of the blades near the midpassage. However, the size and number of cells has decreased from the Original design.

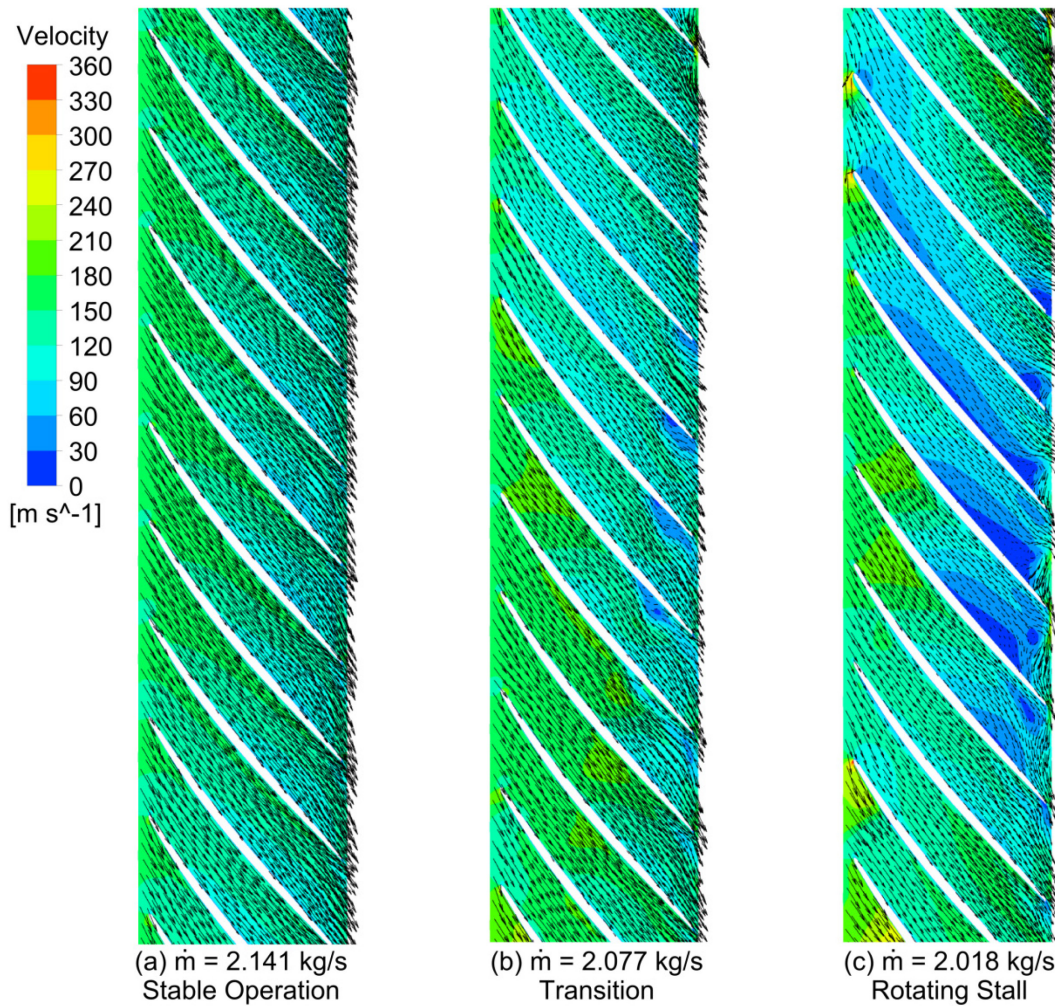


**Figure 6.13. Velocity contours showing stable, transition and rotating stall operation on the  $N = 20640$  rpm speed-line simulation for the Combo design**

For the 20640 rpm line, the Combo design's rotating stall onset is moved to 2.018 kg/s. The Original design had an onset flow of 2.077 kg/s. In terms of stall margin, the improvement of the Combo design is of 2.515% over the Original design. The smaller increase for the 20640 rpm line as compared to the 6.651% increase in the 19240 rpm line is expected. In general, higher speed lines tend to be less stable and rotating stall occurs on them more frequently. The smaller increase in stall margin for the 20640 rpm line fits with this observation.

## **6.6 CONCLUSIONS**

The compressor re-design was completed with the objective of designing an improved compressor with a wider operating range and similar performance characteristics to the preexisting one. An important restriction to the process was that only the blade geometry could be modified while keeping the flowpath geometry the same, in order to require fewer new parts for testing. The speed-line simulation results for the original impeller showed the cause of the stall pattern to be related to mid-passage separation, likely caused by the excessive blade loading on the design.

Three re-design options were proposed, with the main focus on re-designing the shroud blade distribution in order to reduce separation. Each design was analyzed using steady-state CFD to determine performance and blade loading. The design labeled the "Combo" design was recommended as it matched the performance with less than a 10% drop in head in the near-choke flow point. The Combo design also demonstrated significant improvement in flow separation at the near-surge point, which indicates less likelihood for rotating stall to occur. The full 360°, transient speed line simulations were completed for this design to determine the improvement in rotating stall onset.



The speed line simulations for the Combo design showed an improvement over the original design. For the  $N = 19240$  rpm speed line, the stable operating range improved by 6.65%, while for the higher speed,  $N = 20640$  rpm, the improvement was of 2.51%. The improvement in both cases proved that modifications to the blade angle distribution successfully decreased separation at near-surge flow rates and allow for a measureable increase in stable operating range. Additionally, the results showed that the existing empirical recommendations are insufficient in the design for stability of centrifugal compressors. Further improvements to the operating range could be achieved by modifying the flowpath geometry, in particular the shroud curve, but would require the modifications of more parts in the compressor.

Finally, the results proved the effectiveness of the developed speed-line simulation methods as an added tool in the design process of a centrifugal compressor. The results showed that an accurate prediction of rotating stall onset can be achieved before experimental testing, and poor geometries may be discarded or re-designed before testing. The computing time required for the analyses is still small compared to that required to build and test a new compressor, while also requiring only a fraction of the cost.

## CHAPTER 7: CONCLUSIONS

### 7.1 SUMMARY

Unsteady numerical simulations have been completed on a full 360° model centrifugal compressor during rotating stall operation, in order to capture the formation of the stall cell in the impeller. Two different types of simulations were completed and validated, with the objectives of accurately modeling the rotating stall cells and of predicting the onset flow rate of the phenomenon. Finally, the analysis methods are used to re-design the compressor for a wider stable operating range.

The fixed-flow simulation results prove that the code can simulate the initial disturbance in the impeller and its growth into a fully-developed stall cell. In the case presented, the stall cells forms due to excessive incidence at low flow rates. Additionally, the numerical results match well with rotating stall theory. The flow patterns during rotating stall operation demonstrate how the backflow in the inducer causes the stall cell to affect more than one passage at a time, which allows the stall to propagate in the same direction in which the flow reverses around the leading edge of the blades. The propagation speed of the stall is estimated at 87% of the rotor speed, which also matches well with observed data on impeller rotating stall. The fixed-flow simulations also showed a relatively simple method of detecting rotating stall during the transient simulations. The development of rotating stall in the impeller caused supersynchronous fluctuations in the mass-flow traces at the Inlet/Rotor and Rotor/Diffuser interfaces of the simulation domain. During stable operation, these high-frequency oscillations were not present.

The speed-line transient simulations were completed with the purpose of effectively determining the onset of the rotating stall phenomenon. The described FFT analysis of the

simulation results was used to accurately determine the onset point for the rotating stall. The detection of rotating stall onset in the numerical simulations was highly accurate when compared to the experimental results. Due to the larger flow step size in the testing results, the CFD estimates of the onset are within experimental uncertainty. The larger step size in the test valve may have incorrectly determined the onset flow, having jumped past the real onset during the flow adjustment. Either way, the simulation results show that the onset flow rate can be determined within a very accurate envelope of the actual results. The speed-line simulation results showed that rotating stall occurs due to excessive blade loading. The results also confirmed that the location and type of rotating stall can easily vary along the same speed line, which is also typically observed in experiments.

The compressor re-design was successful in determining the causes of rotating stall in the original impeller and proposing design modifications to improve the stability of the compressor. Within the given requirements, the changes in blade angle distribution successfully decreased separation at near-surge flow rates and allowed for a measureable increase in stable operating range. Furthermore, the process determined that the second requirement on the re-design was too stringent. Modifying the impeller blade angle distribution does provide some stability benefits, but it is limited to a relatively small improvement in range.

## **7.2 CONTRIBUTIONS**

The research completed in this work provides several important advancements to the knowledge base for computational studies of rotating stall. The fixed-flow simulations, used to model and characterize rotating stall, validated the use of CFD methods to detect rotating stall. The first case of numerical simulation of full-span impeller rotating stall was documented in the

results. Additionally, it was discovered that mass-flow fluctuations at the Rotor-Stator interfaces appear only during rotating stall operation.

The speed-line simulations were developed as a unique CFD method to detect rotating stall onset. Previously, numerical simulations have not been able to determine the stable and unstable operation ranges for a compressor. The simulations also confirmed the association between the mass flow fluctuations and the presence of rotating stall. Using FFT analysis of the mass flow fluctuations, a methodology was developed to determine the onset of rotating stall. This provides a simple method to determine the stable and unstable regions of operation.

It was proven that rotating stall can be accurately predicted using numerical simulations. The computing time required for the analyses is still small compared to that required to build and test a new compressor. The re-design of the compressor was completed as a proof that the developed methods can improve the design of a new compressor impeller before experimental testing. During the re-design exercise, it was shown that existing design guidelines are insufficient in designing for compressor stability. Additionally, the exercise proved that the methods developed can be used to determine poor geometries before testing and can quantify the improvement in stall margin between alternative designs.

### **7.3 RECOMMENDATIONS**

The application of unsteady CFD simulation to design of compressors and analysis of rotating stall has some further applications that were not explored in this work. However, in order to effectively study the phenomenon it will first be necessary to reduce simulation times for the speed-line simulations. The parallel processing study showed that increasing the number of processors beyond the current amount will result in significant numerical error. Therefore,

there are only a few possibilities for this: reducing the mesh size, increasing the time step size, increasing the mass flow step size, and decreasing the number of time steps completed per mass flow rate. Of these, the mesh size is already close to the coarsest size possible without sacrificing significant accuracy, and therefore would be a difficult choice. The size of the mass flow steps would also affect the accuracy of the onset flow prediction. Larger steps will have shorter simulation times, but also result in a less accurate prediction of the onset flow rate.

Based on the results seen in these studies, it is recommended to increase the size of the time steps and to decrease the number of time steps completed during each mass flow rate. The time steps chosen in these studies are on the conservative side, using 50 time steps per passage rotation, in order to detect an accurate stall pattern. The size of the time steps may be increased provided the steps are still within the time scales required for the development of rotating stall. A recommended starting point would be 30 time steps per passage revolution. Decreasing the number of time steps completed per mass flow rate will require further investigation. One revolution has shown to be a long enough period for the rotating stall pattern to form before the mass flow is dropped again. The studies completed during this research showed that extending the time to multiple revolutions provided little to no benefit towards the prediction of rotating stall. Decreasing to fractions a revolution was not investigated, but this may prove to be a valid option for decreasing the simulation time.

There are two possible applications of interest for continuing this work. The first would be complete a parametric analysis to determine the effect of different design options on the rotating stall onset point. Individually varying features such as blade angle distribution, inlet blade angle gradient, number of blades, hub and shroud curvatures should have significant effect on the onset point of rotating stall. A well-developed parametric study would allow for a better

understanding of these effects which will support compressor engineers in increasing the stability range of their designs. The fact that it may be completed numerically, rather than building and testing each design would be an important interest factor.

A second possible application relates to the blade vibrations that are associated with impeller rotating stall. Due to the small blade surface area, the rotation of the impeller, and the very small time scale at which the aerodynamic phenomenon occurs, experimental studies only provide limited understanding of how rotating stall affects the compressor blades. There is no such limitation in numerical simulations. A coupled analysis of the aerodynamic forces experienced during rotating stall with the stress and vibrations induced onto the rotor blades would be possible. The main difficulty would arise from the limited storage capacity of the computing system in use. Such a study would require full flow and stress data to be saved for each time step, maxing out most systems in less than one revolution of the impeller. If a simpler method may be devised, this type of analysis could lead to important innovations in blade design.

## REFERENCES

## REFERENCES

- [1] H. Krain, "Review of Centrifugal Compressor's Application and Development," *ASME Journal of Turbomachinery*, vol. 127, pp. 25-34, January 2005.
- [2] D. Japikse, *Centrifugal Compressor Design and Performance*. Vermont, USA: Concepts ETI, Inc., 1996.
- [3] S.L. Dixon, *Fluid Mechanics and Thermodynamics of Turbomachines*. Oxford, UK: Elsevier Butterworth-Heinemann, 1998.
- [4] R.C. Dean, "On the Necessity of Unsteady Flow in Fluid Machines," *ASME Journal of Basic Engineering*, vol. 81, pp. 24-28, March 1959.
- [5] S. Niazi, Numerical Simulation of Rotating Stall and Surge Alleviation in Axial Compressors, Ph.D. Dissertation, Georgia Institute of Technology, May 2000.
- [6] D.F. Marshall and J.M. Sorokes, "A Review of Aerodynamically Induced Forces Acting on Centrifugal Compressors, and Resulting Vibration Characteristics of Rotors," in *29th Turbomachinery Symposium*, Texas A&M University, 2000, pp. 263-280.
- [7] J.M. Sorokes, "Rotating Stall - An Overview of Dresser-Rand Experience," Dresser-Rand, [www.dresser-rand.com](http://www.dresser-rand.com).
- [8] P. Frigne and R. Van den Braembussche, "Distinction Between Different Types of Impeller and Diffuser Rotating Stall in a Centrifugal Compressor With Vaneless Diffuser," *ASME Journal of Engineering for Gas Turbines and Power*, vol. 106, pp. 468-474, April 1984.
- [9] N.G. Whitbeck, "An Experimental Study of Blade-to-Blade Pressure Differences and Operating Characteristics of a Centrifugal Compressor", Master's Thesis, Michigan State University, 1994.
- [10] A. Stein, Computational Analysis of Stall and Separation Control in Centrifugal Compressors, Ph.D. Dissertation, Georgia Institute of Technology, May 2000.
- [11] U. Haupt, K. Bammert, and M. Rautenberg, "Blade Vibration on Centrifugal Compressors - Fundamental Considerations and Initial Measurements," in *ASME Gas Turbine Conference and Exhibit*, Houston, USA, March 1985, ASME Paper 85-GT-92.
- [12] U. Haupt, K. Bammert, and M. Rautenberg, "Blade Vibration on Centrifugal Compressors - Blade Response to Different Excitation Conditions," in *ASME Gas Turbine Conference and Exhibit*, Houston, USA, March 1985, ASME Paper 85-GT-93.



- [13] U. Haupt, A.N. Abdelhamid, N. Kämmer, and M. Rautenberg, "Excitation of Blade Vibration by Flow Instability in Centrifugal Compressors," in *ASME International Gas Turbine Conference and Exhibit*, Dusseldorf, West Germany, June 1986, ASME Paper 86-GT-283.
- [14] U. Haupt, D.F. Jin, and M. Rautenberg, "On the Mechanism of Dangerous Blade Vibration Due to Blade Flow Interactions on Centrifugal Compressors," in *ASME Gas Turbine and Aeroengine Congress and Exposition*, Toronto, Canada, June 1989, ASME Paper 89-GT-291.
- [15] D.E. Bentley, P. Goldman, and J. Yuan, "Rotor Dynamics of Centrifugal Compressors in Rotating Stall," *ORBIT*, vol. 22, pp. 40-50, 2001, Bentley Nevada Corporation.
- [16] W. Jansen, "Rotating Stall in a Radial Vaneless Diffuser," *ASME Journal of Basic Engineering*, vol. 86, pp. 750-758, 1964, ASME Paper 64-FE-6.
- [17] U. Haupt, D. Jin, J. Chen, and M. Rautenberg, "Investigation of Rotating Stall Phenomenon of Multitudinous Stall Cells and Its Impact on Blade Excitation of Centrifugal Compressor Impeller," in *INTERFLUID 1st International Congress on Fluid Handling Systems*, Essen, Germany, September 1990, pp. 383-393.
- [18] U. Siedel et al., "Rotating Stall Flow and Dangerous Blade Excitation of Centrifugal Compressor Impeller," in *ASME International Gas Turbine and Aeroengine Congress and Exposition*, Orlando, USA, June 1991, ASME Paper 91-GT-102.
- [19] A. Engeda, "The Unsteady Performance of a Centrifugal Compressor with Different Diffusers," *IMEchE Journal of Power and Energy*, vol. 215, no. 5, pp. 585-599, 2001.
- [20] A.N. Abdelhamid, "Analysis of Rotating Stall in Vaneless Diffusers of Centrifugal Compressors," in *ASME Gas Turbine Conference and Products Show*, New Orleans, USA, March 1980, ASME Paper 80-GT-184.
- [21] N. Kämmer and M. Rautenberg, "A Distinction Between Different Types of Stall in Centrifugal Compressor Stage," *ASME Journal of Engineering for Gas Turbines and Power*, vol. 108, no. 1, pp. 83-93, January 1986, ASME Paper 85-GT-194.
- [22] A.N. Abdelhamid, "Effects of Vaneless Diffuser Geometry on Flow Instability in Centrifugal Compression Systems," *Canadian Aeronautics and Space Journal*, vol. 29, no. 3, pp. 259-266, 1983.
- [23] S. Mizuki, Y. Kawashima, and I. Ariga, "Investigation Concerning Rotating Stall and Surge Phenomena Within Centrifugal Compressor Channels," in *ASME International Gas Turbine Conference*, London, UK, 1978, ASME Paper 78-GT-9.

- [24] N. Kämmer and M. Rautenberg, "An Experimental Investigation of Rotating Stall Flow in a Centrifugal Compressor," in *ASME International Gas Turbine Conference and Exhibit*, London, UK, April 1982, ASME Paper 82-GT-82.
- [25] A.H. Stenning, "Rotating Stall and Surge," *ASME Journal of Fluids Engineering*, vol. 102, no. 1, pp. 14-20, March 1980.
- [26] H.W. Emmons, C.E. Pearson, and H.P. Grant, "Compressor Surge and Stall Propagation," *Transactions of the ASME*, vol. 77, pp. 455-469, May 1955.
- [27] E. Lennemann and J.H.G. Howard, "Unsteady Flow Phenomena in Rotating Centrifugal Impeller Passages," *ASME Journal of Engineering for Power*, vol. 92, pp. 65-72, January 1970.
- [28] N. Krause, K. Zähringer, and E. Pap, "Time-resolved Particle Image Velocimetry for the Investigation of Rotating Stall in a Radial Pump," *Experiments in Fluids*, vol. 39, pp. 192-201, 2005.
- [29] J. Chen et al., "The Interpretation of Internal Pressure Patterns of Rotating Stall in Centrifugal Compressor Impellers," in *ASME International Gas Turbine and Aeroengine Congress and Exposition*, Cincinnati, USA, May 1993, ASME Paper 93-GT-192.
- [30] Y.N. Chen, U. Haupt, and M. Rautenberg, "The Vortex-Filament Nature of Reverse Flow on the Verge of Rotating Stall," *ASME Journal of Turbomachinery*, vol. 111, no. 4, pp. 450-461, October 1989.
- [31] Y.N. Chen, U. Haupt, and M. Rautenberg, "Rossby Waves and Associated Transient Rotating Stall Vortices in Radial and Axial Turbocompressors," *Zeitschrift für Flugwissenschaften und Weltraumforschung*, vol. 14, pp. 233-246, 1990.
- [32] Y.N. Chen, U. Haupt, U. Seidel, D. Jin, and M. Rautenberg, "The Behavior of the Rossby Waves of Rotating Stall in Turbocompressors," in *INTERFLUID 1st International Congress of Fluid Handling Systems*, Essen, Germany, September 1990, pp. 403-416.
- [33] Y.N. Chen, U. Seidel, U. Haupt, and M. Rautenberg, "The Vortex Behavior of the Rotating-Stall Cell of a Centrifugal Compressor with Vaned Diffuser," in *ASME International Gas Turbine and Aeroengine Congress and Exposition*, Cologne, Germany, June 1992, ASME Paper 92-GT-66.
- [34] Y. Senoo and Y. Kinoshita, "Limits of Rotating Stall and Stall in Vaneless Diffusers of Centrifugal Compressors," in *ASME Turbo Expo*, London, UK, 1978, ASME Paper 79-GT-19.
- [35] A.N. Abdelhamid, "Control of Self-Excited Flow Oscillations in Vaneless Diffuser of Centrifugal Compression Systems," *Canadian Aeronautics and Space Journal*, vol. 29, no.

4, pp. 336-345, 1983.

- [36] H. Kobayashi, H. Nishida, Takagi, T., and Y. Fukushima, "A Study on the Rotating Stall of Centrifugal Compressors (1st Report, Effect of Vaneless Diffuser Width on Rotating Stall)," *Transactions of JSME (B Edition)*, vol. 54, no. 499, pp. 589-594, 1988.
- [37] H. Nishida, H. Kobayashi, T. Takagi, and Y. Fukushima, "A Study on the Rotating Stall of Centrifugal Compressors (2nd Report, Effect of Vaneless Diffuser Inlet Shape on Rotating Stall)," *Transactions of JSME (B Edition)*, vol. 56, no. 529, pp. 98-103, 1990.
- [38] J.M. Sorokes, "A CFD Assessment of Entrance Area Distributions in a Centrifugal Compressor Vaneless Diffuser," in *ASME International Gas Turbine and Aeroengine Congress and Exposition*, Huntsville, USA, June 1994, ASME Paper 94-GT-90.
- [39] Y. Yoshida, Y. Murakami, H. Tsurusaki, and Y. Tsujimoto, "Rotating Stalls in Centrifugal Impeller/Vaned Diffuser Systems," in *1st ASME/JSME Joint Fluids Engineering Conference*, New York, USA, 1991, pp. 125-130.
- [40] L. Bonciani, L. Terrinoni, and A. Tesei, "Unsteady Flow Phenomena in Industrial Centrifugal Compressor Stage," in *Rotordynamic Instability Problems in High Performance Turbomachinery*, Texas A&M University, 1982, pp. 344-364, NASA CP 2250.
- [41] J.T. Gravdahl, Modeling and Control of Surge and Rotating Stall in Compressors, Dr.Ing. Thesis, Norwegian University of Science and Technology, 1998.
- [42] J.D. Paduano, E.M. Greitzer, and A.H. Epstein, "Compression System Stability and Active Control," *Annual Review of Fluid Mechanics*, vol. 33, pp. 491-517, January 2001.
- [43] A. Goto, "Suppression of mixed-flow pump instability and surge by the active alteration of impeller secondary flows," *ASME Journal of Turbomachinery*, vol. 116, pp. 621-628, 1994.
- [44] I.J. Day, "Active Suppression of Rotating Stall and Surge in Axial Compressors," *ASME Journal of Turbomachinery*, vol. 115, pp. 40-47, January 1993.
- [45] F.K. Moore, "Weak Rotating Flow Disturbances in a Centrifugal Compressor with a Vaneless Diffuser," in *ASME Gas Turbine and Aeroengine Congress and Exposition*, Amsterdam, The Netherlands, September 1988, ASME Paper 88-GT-76.
- [46] D.A. Hoying, C.S. Tan, H.D. Vo, and E.M. Greitzer, "Role of Blade Passage Flow Structures in Axial Compressor Rotating Stall Inception," *ASME Journal of Turbomachinery*, vol. 121, pp. 735-742, October 1999.

- [47] J. März, C. Hah, and W. Neise, "An Experimental and Numerical Investigation Into the Mechanisms of Rotating Instability," *ASME Journal of Turbomachinery*, vol. 124, no. 3, pp. 367-375, July 2002.
- [48] J.P. Chen, R.S. Webster, M.D. Hathaway, G.P. Herrick, and G.J. Skoch, "High Performance Computing of Compressor Rotating Stall and Control," *Integrated Computer-Aided Engineering*, vol. 16, pp. 73-89, 2009.
- [49] G. Legras, N. Gourdain, and I. Trebinjac, "Numerical Analysis of the Tip Leakage Flow Field in a Transonic Axial Compressor with Circumferential Casing Treatment," *Journal of Thermal Science*, vol. 19, no. 3, pp. 198-205, 2010.
- [50] Y. Wu, W. Chu, H. Zhang, and Q. Li, "Parametric Investigation of Circumferential Grooves on Compressor Rotor Performance," *ASME Journal of Fluids Engineering*, vol. 132, no. 12, pp. 121103-1-10, December 2010.
- [51] M. Choi, N.H.S. Smith, and M. Vahdati, "Validation of Numerical Simulation for Rotating Stall in a Transonic Fan," in *ASME Turbo Expo 2011*, Vancouver, Canada, 2011, ASME Paper GT2011-46109.
- [52] T. Sano, Y. Yoshida, Y. Tsujimoto, Nakamura, Y., and T. Matsushima, "Numerical Study of Rotating Stall in a Pump Vaned Diffuser," *ASME Journal of Fluids Engineering*, vol. 124, no. 2, pp. 363-370, June 2002.
- [53] A. Lucius and G. Brenner, "Numerical Simulation and Evaluation of Velocity Fluctuations During Rotating Stall of a Centrifugal Pump," *ASME Journal of Fluids Engineering*, vol. 133, no. 8, pp. 081102-1-8, August 2011.
- [54] C. Widmer, T. Staubli, and N. Ledergerber, "Unstable Characteristics and Rotating Stall in Turbine Brake Operation of Pump-Turbines," *ASME Journal of Fluids Engineering*, vol. 133, no. 4, pp. 041101-1-9, April 2011.
- [55] N. Tani, N. Yamanishi, and Y. Tsujimoto, "Influence of Flow Coefficient and Flow Structure on Rotating Cavity in Inducer," *ASME Journal of Fluids Engineering*, vol. 134, no. 2, pp. 021302-1-13, February 2012.
- [56] S. Ljevar, H.C. de Lange, and A.A. van Steenhoven, "Two-Dimensional Rotating Stall Analysis in a Wide Vaneless Diffuser," *International Journal of Rotating Machinery*, vol. 2006, pp. 1-11, 2006, Article ID 56420.
- [57] J.N. Everitt and Z.S. Spakovszky, "An Investigation of Stall Inception in Centrifugal Compressor Vaned Diffusers," in *ASME Turbo Expo 2011*, Vancouver, Canada, 2011, ASME Paper GT2011-46332.

- [58] K. Iwakiri, M. Furukawa, S. Ibaraki, and I. Tomita, "Unsteady and Three-dimensional Flow Phenomena in a Transonic Centrifugal Compressor Impeller at Rotating Stall," in *ASME Turbo Expo 2009*, Orlando, USA, June 2009, ASME Paper GT2009-59516.
- [59] CD-adapco Press Release. (2011, July) STAR-CCM+ V4.04: Now with Harmonic Balance. [Online]. <http://www.cd-adapco.com/news/2009/06-30-starccm.html>
- [60] T. David, D. Zhang, and M. Cave, "Frictional Effects on a Base and a Flow-Trimmed Impeller of a Low Specific Speed Industrial Compressor," in *ASME Turbo Expo 2006*, vol. 6B, Barcelona, Spain, 2006, pp. 1121-1130, ASME paper GT2006-90998.
- [61] M. Ji, M. Cave, and D. Zhang, "Effects of Impeller Blade Loading on Industrial Centrifugal Compressor Performance and Stability," in *ASME International Mechanical Engineering Congress & Exposition*, Vancouver, Canada, November 2010, ASME Paper IMECE2010-40929.
- [62] A.N. Abdelhamid, U. Haupt, and M. Rautenberg, "Unsteady Flow Characteristics in a Centrifugal Compressor with Vaned Diffuser," in *ASME Gas Turbine Conference and Exhibition*, Anaheim, USA, May 1987, ASME Paper 87-GT-142.
- [63] "Turbulence and Wall Function Theory," in *ANSYS CFX-Solver Theory Guide*. Canonsburg, PA, USA: ANSYS, Inc., November 2009, ch. 2, pp. 53-97.
- [64] "Turbulence and Near-Wall Modeling," in *ANSYS CFX-Solver Modeling Guide*. Canonsburg, PA, USA: ANSYS, Inc., November 2009, ch. 4, pp. 97-122.
- [65] S.B. Pope, "Turbulent-viscosity models," in *Turbulent Flows.*: Cambridge University Press, 2009, ch. 10, pp. 358-386.
- [66] "Using the Solver in Parallel," in *ANSYS CFX-Solver Modeling Guide*. Canonsburg, PA, USA: ANSYS, Inc., November 2009, ch. 14, pp. 347-364.
- [67] J.D. Anderson, *Computational Fluid Dynamics: The Basics with Applications*, International ed. Singapore: McGraw-Hill, Inc., 1995.
- [68] S. Anish and N. Sitaram, "Steady and Transient Computations of Interaction Effects in a Centrifugal Compressor with Different Types of Diffuser," in *ASME Turbo Expo 2010*, Glasgow, UK, June 2010, ASME paper GT2010-22913.
- [69] J.S. Kang and S.H. Kang, "Steady and Unsteady Flow Phenomena in a Channel Diffuser of a Centrifugal Compressor," *JSME International Journal Series B*, vol. 47, no. 1, pp. 91-100, 2004.
- [70] I.J. Day, "Stall Inception in Axial Flow Compressors," *AMSE Journal of Turbomachinery*,

vol. 115, pp. 1-9, January 1993.

- [71] R.H. Aungier, *Centrifugal Compressors: A Strategy for Aerodynamic Design and Analysis*. New York, USA: ASME Press, 2000.
- [72] F. Dallenbach, "The Aerodynamic Design and Performance of Centrifugal and Mixed-Flow Compressors," *SAE Technical Paper Series*, 1961, SAE Paper 610160.